COMPANY MEMBERS OF THE NORDIC RHEOLOGY SOCIETY

ANNUAL TRANSACTIONS

THE NORDIC RHEOLOGY SOCIETY

VOLUME 34
2026

PAPERS PRESENTED AT

Joint Conference of

THE 35th NORDIC RHEOLOGY SOCIETY

and

THE 14th INTERNATIONAL CONFERENCE ON
MECHANICS OF TIME-DEPENDENT MATERIALS

at Lund in Sweden,

August 26 - 28, 2026

Editor: Herimonja A. Rabenjafimanantsoa

THE NORDIC RHEOLOGY SOCIETY

The Nordic Rheology Society engages people interested in rheology in the Nordic countries. The society has approximately 140 members. The objective of the society is to promote and propagate rheology at all levels by building a broad forum where academia and industry, in their applicational and theoretical guises can meet, share and discuss ideas to their mutual benefit. The Nordic Rheology Society represents the Nordic countries in the International Committee of Rheology (ICR).

The elected officers of the society are:

President:
Dr. Olli-Ville Laukkanen, Principal Scientist, VTT Technical Research Center, Finland.

Secretary:
Dr. Norbert Raak, University of Copenhagen, Denmark.

Treasurer:
Kasra Amini, KTH Royal Institute of Technology, Sweden.

ICR-representative:
Prof. Roland Kadar, Chalmers University of Technology, Sweden.

For further information about the Nordic Rheology Society and membership application please contact:

Dr. Olli-Ville Laukkanen, Principal Scientist, VTT Technical Research Center, Finland.
Email: nrs@nordicrheologysociety.org

Website: nordicrheologysociety.org

ISBN 978-82-692721-7-8
ISSN 1601-4057

Preface

The 34th Volume of the *Annual Transactions of the Nordic Rheology Society* (ATNRS) comprises the papers and posters presented at the joint conference between the 35th Nordic Rheology Conference (NRC) and the 14th International Conference on Mechanics of Time-Dependent Materials (MTDM) in Lund, Sweden from August 26-28, 2026.

The aim was to bring together researchers and industry professionals, covering all aspects of rheology and the mechanics of time-dependent materials.

This year s program welcomed a diverse range of contributions, from fundamental research to industrial case studies, covering experimental, modeling, and application-oriented work. The topics spanned a wide range of rheology, including applications in polymers, foods, coatings, paper, fibers, pharmaceuticals, and more. The conference featured a broad scope of materials and phenomena, with particular emphasis on coupling advanced X-ray and neutron techniques with rheological studies. This included explorations into polymers and composites, soft matter, metamaterials, 3D-printed structures, living tissues, rubber, and beyond.

The conference was successfully organized by a committee comprising representatives from Chalmers University of Technology, RISE, MAX IV, ESS, and Copenhagen University. The team included Roland Kadar and Marko Bek (Chalmers), Mats Stading (RISE & Chalmers), Ann Terry and Kim Nygard (MAX IV), Andrew Jackson (ESS), Alexandra Aulova (Nouryon), Ruifen Li (Aarhus University), and Josefin Martell (LINXS). The theme core group also provided support. The Science Village and Altitude assisted with both the organization and registration processes.

The invited lectures were given by the following experts: Prof. Norman J. Wagner from the University of Delaware, Dr. Vivian Lutz Bueno from Paul Sherrer Institute and ETH Zurich, Prof. Leif Asp from Chalmers University of Technology and Prof. Chris Holland from the University of Sheffield.

The year s Annual Business Meeting of the society was held during the conference days.

A short course for everyone interested in rheology was conducted on the morning of August 26th. The course was held by Annika Sahlstrom (Reokonsa), a well known rheology lecturer in Scandinavia. Ann Terry who is a beamline scientist gave also an introduction to X-ray and neutron techniques.

An industry-academia workshop was held during the conference, open to all participants. The aim was to strengthen connections between academia and industry, facilitate dialogue among researchers, and identify industrially relevant research questions for academic collaboration.

This volume contains 12 oral and 3 poster submissions from Nordic countries and worldwide. The received contributions are divided into the following sessions: 'Combined Methods and Multiscale Analysis , 'Polymeric Materials and Composites , 'Complex Flows and Modeling', 'Biological Systems , 'Cellulosic Systems , Advances in Rheometry', and 'Poster Presentations . The manuscripts will be accessible online as PDF files on the website.

Finally, I would like to express my gratitude to the contributors, reviewers, sponsors, exhibitors, session chairs, and the society board members for their valuable contributions, support and cooperation. I also extend my appreciation to our invited lecturers for sharing their expertise.

The preparation of this volume was made using LaTeX processing code.

Dr. Herimonja A. Rabenjafimanantsoa
University of Stavanger - Norway
June 2026

Contents 2026

Invited Lecturers

Combined Methods and Multiscale Analysis

Polymeric Materials and Composites

Complex Flow and Modeling

Biological Systems

Cellulosic Systems

Advances in Rheometry

Poster Presentations

Invited Lecturers

Mini-biographies

Professor **Norman J. Wagner**'s research focuses on the rheology and microstructure of complex fluids, combining rheology with advanced scattering techniques to uncover structure - property relationships in colloidal suspensions and soft materials. He is a member of the U.S. National Academy of Engineering, recipient of the 2014 Bingham Medal of the Society of Rheology, and former President of the Society of Rheology, among other honours. He is currently the Robert L. Pigford Chair and Professor of Chemical and Biomolecular Engineering at the University of Delaware.

Dr. **Viviane Lütz Bueno** is a Senior Scientist at Paul Scherrer Institute (PSI), Switzerland and lecturer at ETH Zürich working on method development and structural characterization of soft matter using small-angle scattering techniques. Her research focuses on in-situ scattering measurements of complex soft-matter systems, including microfluidic platforms for scattering experiments, chemical reactions under confinement, and dark-field imaging approaches.

Leif Asp is Professor of Lightweight Structures at Chalmers University of Technology and a leading expert in multifunctional composite materials. His research focuses on structural battery composites, where load-bearing materials are designed to simultaneously store electrical energy, enabling entirely new approaches to lightweight system design. His work bridges mechanics, materials science, and energy storage, and has had significant impact on the development of next-generation structural materials for transport and energy applications.

Chris Holland is Professor of Materials Science at the University of Sheffield and a leading expert in bio-derived and hierarchical materials. His research focuses on understanding and replicating the structure–property relationships found in natural materials such as silk, collagen, and other biological polymers, with the aim of developing sustainable high-performance materials. His work combines advanced processing, rheology, and structural characterization to uncover how molecular and mesoscale organization governs macroscopic properties. This includes insights into spinning processes, flow-induced alignment, and the design of biomimetic materials with tailored functionality.

Combined Methods and Multiscale Analysis

FLOW THROUGH FIBRE NETWORKS – EFFECT OF FLUID RHEOLOGY

Mats Stading[1,2], Camilla Öhgren[1], Sandra Barman[1], Torben Nilsson Pingel[1], Innokenty Kantor[3] and Niklas Lorén[1]

[1]RISE Research Institutes of Sweden, Gothenburg, Sweden
[2]Chalmers University of Technology, Gothenburg, Sweden
[3]MAX IV, Science Division, Lund, Sweden

DOI: 10.31265/rt9q0p57

ABSTRACT

Fluid flow in fibrous networks is crucial for many technical applications such as wound care and hygiene products as well as for tissue paper. The flow of Newtonian, low-viscous fluids like water is well studied whereas the flow of viscoelastic fluids is less so. It is nevertheless highly important for the applications.

Model fluids could be used to determine the influence of important rheological properties such as viscosity, elasticity and shear thinning on the flow. Fluids containing the same components can be tuned to have constant viscosity (Newtonian), constant viscosity but elastic (Boger), and shear thinning to determine the influence of each property on the flow. Initially flow was determined in real time for Newtonian and shear thinning fluids using light microscopy and X-ray radiography. The results showed a large influence of the fluid rheology on the flow through the fibre networks.

INTRODUCTION

The flow of Newtonian fluids (water) through fibre networks has been extensively studied[1] and has even resulted in methods for predicting flow from 3D-structure (Gesualdo model)[2].

Viscoelastic flow in porous media has been extensively studied for its applications in geophysics, biology and especially enhanced oil recovery[3,4]. There are also some studies on the flow of viscoelastic fluids through fibre networks, especially modelling[5,6] and in models of fibre systems[7,8].

The flow of viscoelastic fluids through fibrous media is a complex phenomenon. Studies in fibre models have shown e.g. that fluid elasticity significantly increases flow resistance, with elastic effects becoming noticeable at Deborah numbers around 0.5 [7]. The pressure drop in these flows is influenced by both fluid and fibre network properties, with viscoelastic fluids exhibiting an "excess" pressure drop as compared to Newtonian fluids[8,9].

A set of model fluids, as introduced in the abstract (Newtonian, Boger and shear thinning) have previously been utilised for studies of swallowing[10,11] and perception[12]. Boger fluids[13] have a wider use especially for testing constitutive equations for polymer melts. The latter were however more viscous, and here we aimed for model fluids with lower viscosity to match the technical applications.

In an initial study a range of maltodextrin and xanthan solutions were evaluated for flow through fibre materials using light microscopy and X-ray radiography.

MATERIALS AND METHODS

Materials

The fluids used in this study were prepared using maltodextrin Glucidex IT 19 (Roquette, Lestrem, France) and xanthan (Grindstedt Clear 80 (IFF, Brabrand, Denmark).

Stock solutions of maltodextrin of 60% w/w and xanthan 1% were mixed and stirred over night on a magnetic stirrer. The stock solutions were then diluted into the final concentrations and stirred over night. The fluids used in the study were:

- Newtonian: 15%, 30% and 60% w/w maltodextrin
- Shear thinning: 0.01%, 0.1% and 0.8% w/w xanthan

The fluids were finally mixed with 10% Gadovist (Bayer Radiology, Leverkusen, Germany) as a contrast agent for the X-ray studies.

The fibrous matrix was consisted of PET fibres intertwined to a fibrous material as shown in **Fig. 1a**.

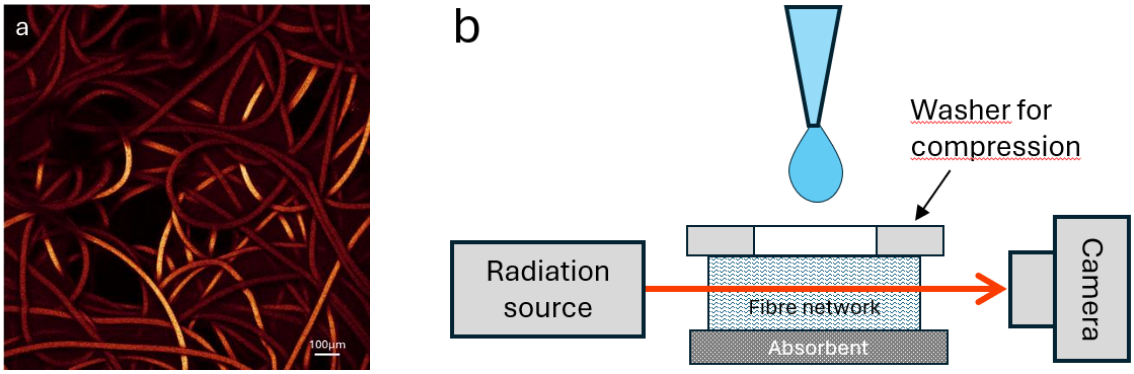

FIGURE 1: a) Microstructure of the fibrous material visualised by confocal laser scanning microscopy, b) Sketch of the experimental setup used for X-ray radiography and for light microscopy.

Methods

Viscometry was performed using an ARES-G2 (TA Instruments, New Castle, DE, USA) equipped with a concentric cylinder system (cup diameter 20 mm). The measurements were performed at 20°C.

A pipette was placed over the fibrous material and a drop of the fluid was dropped onto it while monitoring the fluid flow by light or X-rays, as shown in **Fig. 1b**. The drop volume was regulated by a syringe pump which was operated remotely. The fibrous material could be compressed lightly by a plastic washer and filter paper was placed under the fibrous material as an absorbent to facilitate drainage through the material.

X-ray radiography was performed at the DanMAX beamline at the MAX IV synchrotron in Lund, Sweden. 2D projections of the sample were recorded in a side view (**Fig. 1b**) during the application of the liquid and the initial flow through the porous material. Each recorded

sequence was 54 seconds long, with a time resolution of 5.4 ms, and a spatial resolution (pixel size) of 0.55 μm.

A microscope equipped with a CMOS camera (Olympus BX53F2, CAM-SC50, Tokyo, Japan) was used to study the flow through the fibrous material. The microscope was placed sideways instead of vertically and the same sample holder as used for X-ray radiography was placed in the microscope. The holder was directly on the microscope table so that the focus distance was fixed to the centre of the sample, i.e. so the flowing droplet was in focus. The syringe tip was connected to a Harvard Apparatus syringe pump (Harvard Bioscience, Holliston, USA). The frame rate was 9 frames/s.

RESULTS AND DISCUSSION

The viscosity of the model fluids was measured and the Power Law model was fitted to the data ($\sigma=K\dot{\gamma}^n$). The results in Table 1 show that the Maltodextrin solutions were Newtonian and the xanthan solutions shear thinning as expected.

Table 1. Power Law constants for the fluids containing 10% Gadovist contrast agent.

Polymer	Concentration	n	K
Maltodextrin	15%	1	0,00244
	30%	1	0,0072
	60%	1	0,27
Xanthan	0,01%	0,90	0,0069
	0,10%	0,62	0,054
	0,80%	0,098	4,9

The xanthan and maltodextrin solution with 0.1% Direct Red dye as were allowed to drain through the fibrous material and monitored by video. Snapshots of the videos are shown in **Fig. 2**. The first image shows when the liquid just reached the material, the second halfway during the flow and the last when the last drop of liquid goes into the absorbent material. This process takes very different times depending on the liquid. It was relatively fast for xanthan (1.5 – 25 s) but considerably slower for the concentrated maltodextrin solution (50 s – 7 minutes).

The study showed a large influence of the viscous behaviour on the flow through the fibre material. The lowest maltodextrin concentration as expected behaved similar to water as its viscosity is just about twice that of water, whereas the high viscosity of the concentrated solution considerably slowed down the flow. Xanthan showed a slightly different behaviour due to the shear thinning. The flow at higher shear rates, initially and when the fluid front reached the absorbent, was fast whereas the intermediate flow was slow.

This initial study is continued with evaluation of fluid dynamics and modelling of the effect of the fibre material and will be published separately.

ACKNOWLEDGEMENTS

The Bo Rydin Foundation for Scientific Research is gratefully acknowledged for funding and Charlotta Hanson, Malin Lundman and Ramin Moghadasi, Essity Hygiene and Health AB, and Fredrik Holmberg, Animato are thanked for experimental assistance and fruitful discussions.

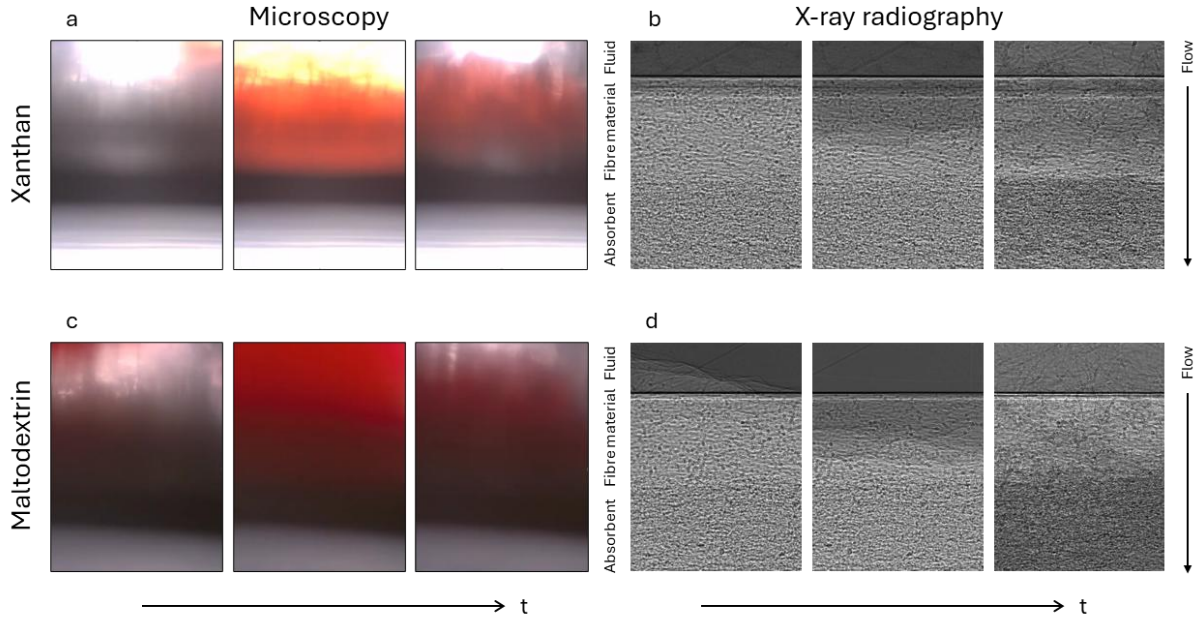

FIGURE 2: Example of the flow visualised as snapshots at the beginning, halfway and end of flow into the fibrous material by a xanthan solution (top, a and b) and a maltodextrin solution (bottom, c and d) visualised by light microscopy (a and c), and X-ray radiography (b and d).

REFERENCES

1. Abedsoltan H. A review on liquid flow through low-density fibrous porous media. *Chem Eng Res Des*. 2023/12/01/ 2023;200:445-455. doi:https://doi.org/10.1016/j.cherd.2023.10.058
2. Gebäck T, Heintz A. A Lattice Boltzmann Method for the Advection-Diffusion Equation with Neumann Boundary Conditions. *Communications in Computational Physics*. 2014;15(2):487-505. doi:10.4208/cicp.161112.230713a
3. Rock A, Hincapie RE, Tahir M, Langanke N, Ganzer L. On the Role of Polymer Viscoelasticity in Enhanced Oil Recovery: Extensive Laboratory Data and Review. *Polymers*. 2020;12(10):2276.
4. Kumar M, Guasto JS, Ardekani AM. Transport of complex and active fluids in porous media. *J Rheol*. 2022;66(2):375-397. doi:10.1122/8.0000389
5. Shahsavari S, McKinley GH. Mobility of power-law and Carreau fluids through fibrous media. *Physical Review E*. 12/10/ 2015;92(6):063012. doi:10.1103/PhysRevE.92.063012
6. Marshall RJ, Metzner AB. Flow of Viscoelastic Fluids through Porous Media. *Industrial & Engineering Chemistry Fundamentals*. 1967/08/01 1967;6(3):393-400. doi:10.1021/i160023a012
7. James DF, Yip R, Currie IG. Slow flow of Boger fluids through model fibrous porous media. *J Rheol*. 2012;56(5)doi:10.1122/1.4732533
8. Gillissen JJJ. Viscoelastic flow simulations through an array of cylinders. *Physical Review E*. 02/07/ 2013;87(2):023003. doi:10.1103/PhysRevE.87.023003
9. Skartsis L, Khomami B, Kardos JL. Polymeric flow through fibrous media. *J Rheol*. 1992;36(4):589-620. doi:10.1122/1.550365
10. Nyström M, Waqas Muhammad, Margareta Bulow, Olle Ekberg, Stading M. Effects of rheological factors on perceived ease of swallowing. *Appl Rheol*. 2015;25(6)
11. Qazi WM, Ekberg O, Wiklund J, Kotze R, Stading M. Assessment of the Food-Swallowing Process Using Bolus Visualisation and Manometry Simultaneously in a Device that Models Human Swallowing. *Dysphagia*. 2019/12/01 2019;34(6):821-833. doi:10.1007/s00455-019-09995-8
12. Koliandris A-L, Rondeau E, Hewson L, et al. Food Grade Boger Fluids for Sensory Studies. *Appl Rheol*. 2011;21(1)doi:doi:10.3933/applrheol-21-13777
13. Boger DV. Viscoelastic flows through contractions. *Annu Rev Fluid Mech*. 1987;19:157-182.

Polymeric Materials and Composites

A Regularized Inverse Framework for Stress and Strain Analysis of Viscoelastic Bodies via DIC–FEA Integration

Yurie Rai, Keisuke Iizuka and Satoru Yoneyama

Aoyama Gakuin University, 5-10-1 Fuchinobe, Sagamihara, Japan

DOI: 10.31265/xqvwvr33

ABSTRACT

A method for obtaining the strain and stress distributions in a viscoelastic body is proposed by combining digital image correlation with finite element analysis based on the principle of superposition. In this method, the boundary conditions within the measurement region are determined via inverse analysis so that the computed displacement fields match those obtained experimentally. A regularization scheme is introduced to mitigate the influence of measurement errors near the boundaries. The strain distributions are obtained simultaneously with the displacement fields. Meanwhile, the streSatoruss distributions are evaluated from the temporal evolution of the strain components, taking into account the time-dependent mechanical properties of the viscoelastic material. The effectiveness of the proposed method is demonstrated through a numerical simulation. Furthermore, as an application example, stress analyses around contact interfaces are presented. The proposed method alleviates difficulties in data processing during measurement and provides an effective approach for stress and strain analysis of viscoelastic bodies.

INTRODUCTION

In recent years, the demand for lightweight and high-strength materials has led to the expansion of polymer materials into a wide range of applications. Typical examples include automobiles and aircraft, where the use of carbon fiber reinforced plastics is increasing. Polymer materials are known to exhibit viscoelastic behavior, and their mechanical properties and responses differ significantly from those of elastic materials in that they show pronounced time and temperature dependence. Therefore, applying the same treatment as for elastic materials to stress–strain analysis of viscoelastic materials often results in outcomes that are far from reality and physically meaningless. Clarifying complex phenomena such as impact, contact, and fracture in viscoelastic bodies is an important issue in both engineering and industrial contexts, and many studies have been conducted, as in the case of elastic and elastoplastic materials.[1-3]

To experimentally evaluate the mechanical behavior of solid materials, surface strain measurement is often performed. Full-field measurement methods such as moiré and digital image correlation are widely used.[4,5] These methods provide two-dimensional displacement distributions, and strain values can be obtained by differentiating the displacement distributions along the surface of the object. However, since differentiation of measured data amplifies measurement errors, it is known that special techniques are required to obtain appropriate strain values. To reduce the influence of measurement errors included in displacement data, it is common to approximate the displacement distribution in a local region using the least-squares method and obtain strain by differentiating the approximated function.[6] Other approaches include smoothing displacement distributions using finite element models,[7,8] smoothing using

spline functions,[9] and hybrid methods in which finite element analysis is performed using the obtained displacements as boundary conditions.[10] One author[11] has also proposed a method for linear elastic bodies in which boundary conditions of a finite element model are identified by inverse analysis from measured displacement distributions to obtain strain and stress.

In the case of viscoelastic bodies, when evaluating strain distributions using measurement methods such as the moiré method or digital image correlation, displacement distributions are obtained from images at each time step, and strain distributions are calculated using one of the aforementioned methods. Furthermore, to evaluate stress, it is necessary to calculate the time variation of stress from the time variation of strain at each point using viscoelastic constitutive equations. Thus, evaluation of stress in viscoelastic bodies requires smoothing the displacement distribution, differentiating it spatially to obtain strain, and then performing temporal convolution (history integration) of the strain to obtain stress. Consequently, it is difficult to achieve high accuracy due to accumulation of errors. Moreover, the use of finite element models is considered convenient for appropriately performing data processing such as spatial differentiation and temporal integration of measurement data.

Therefore, in this study, we propose a method for evaluating strain and stress in viscoelastic bodies using a DIC–FEA hybrid method that combines displacement measurements obtained by digital image correlation (DIC) with the finite element analysis (FEA). This method is an extension of a previously proposed inverse boundary identification method[11] for elastic bodies to viscoelastic bodies. In this method, boundary load values are determined by inverse analysis so that displacement distributions equivalent to those obtained by measurement are reproduced by FEA, and smooth displacement and strain distributions are obtained. Stress distributions are evaluated by numerically integrating viscoelastic constitutive equations based on the time variation of strain at each point. Although this method utilizes FEA results, displacement and strain are evaluated based on measured displacement distributions, and stress is subsequently calculated. Therefore, it is effective for problems in which reliable analysis results cannot be obtained by FEA due to unclear boundary conditions.

STRESS AND STRAIN ANALYSIS OF ELASTIC BODIES BY INVERSE BOUNDARY IDENTIFICATION

Basic Principle

Consider a linear elastic body for which in-plane displacement distributions are obtained in a measurement region by measurement methods such as the moiré method or digital image correlation. Suppose that part of the displacement in the analysis region is constrained, and a unit concentrated load $P_j = 1$ is applied at a point on the boundary. Let the displacement components at an internal point (x_i, y_i) be u'_{ij} and v'_{ij}. Here, i and j are indices for identifying measurement points and boundary load positions, respectively, where $i = 1 \sim M$ and $j = 1 \sim N$. That is, the number of concentrated loads applied on the boundary is N, and the number of displacement evaluation points in the domain is M. The displacement components u'_{ij} and v'_{ij} can be regarded as compliance representing the relationship between a load applied at a boundary point and the displacement at an interior point. If the actual boundary load values are F_j, the following relationship holds by the principle of superposition:

$$\begin{aligned} u_i &= u'_{ij} F_j \\ v_i &= v'_{ij} F_j \end{aligned} \quad (i = 1 \sim M,\ j = 1 \sim N) \tag{1}$$

where u_i and v_i are displacement components at (x_i, y_i). The displacement components u'_{ij} and v'_{ij} can be obtained by FEA, while u_i and v_i are measured values. Therefore, if $M > N$, the boundary loads F_j can be obtained by the least-squares method as follows:

$$\mathbf{F} = \left(\mathbf{A}^T \mathbf{A} \right)^{-1} \mathbf{A}^T \mathbf{U} \tag{2}$$

Here, **F**, **A**, and **U** denote the nodal forces on the boundary, the compliance matrix obtained from unit concentrated loads, and the measured displacement vector, respectively.

Once the boundary load values F_j are obtained, strain values can be obtained by the principle of superposition as follows:

$$\begin{aligned} \varepsilon_{xi} &= \varepsilon'_{xij} F_j \\ \varepsilon_{yi} &= \varepsilon'_{yij} F_j \quad (i = 1 \sim M,\ j = 1 \sim N) \\ \gamma_{xyi} &= \gamma'_{xyij} F_j \end{aligned} \tag{3}$$

where ε_{xi}, ε_{yi} and γ_{xyi} are strain components at (x_i, y_i), and the primed quantities denote components obtained when a unit load is applied at the j-th point. In this method, boundary loads are determined so that the displacement distribution matches the measured distribution. Furthermore, since the least-squares method is used considering measurement errors, the obtained results are considered to be highly reliable.

Introduction of Regularization

In the above method, the influence of measurement errors included in the input displacement leads to fluctuations in the identified boundary loads. As a result, while smooth and appropriate displacement and strain distributions are obtained inside the analysis region, some irregularities appear near the boundaries. Such phenomena are common in inverse problem analysis, and various regularization methods have been proposed.[12] In this study, we propose introducing a regularization term that minimizes the second derivative of displacement:

$$\mathbf{F} = \left(\mathbf{A}^T \mathbf{A} + \alpha \mathbf{A}_{,xx}^T \mathbf{A}_{,xx} + 2\alpha \mathbf{A}_{,xy}^T \mathbf{A}_{,xy} + \alpha \mathbf{A}_{,yy}^T \mathbf{A}_{,yy} \right)^{-1} \mathbf{A}^T \mathbf{U} \tag{4}$$

where α is the regularization parameter. By minimizing the second derivative of displacement, i.e., the variation of strain, fluctuations in strain near the boundary are reduced. As a result, appropriate strain values can be obtained not only inside the measurement region but also near the boundaries.

Extension to Viscoelastic Bodies

Consider the case where the measurement target is a linear viscoelastic body. In this case, the relationship between boundary loads and displacement varies depending on loading rate and elapsed time, and therefore it is not possible to correctly determine the boundary load values directly from the displacement distribution. On the other hand, since superposition holds for displacement and strain distributions, it is possible to obtain displacement and strain distributions by determining apparent boundary load values using the same method as for elastic bodies. However, stress values cannot be determined by superposition in the same manner as boundary loads. Therefore, after determining the time-dependent strain distribution, stress is

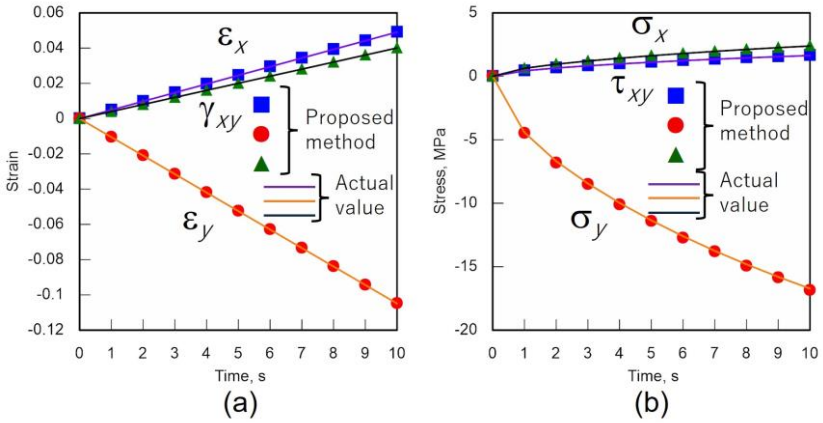

FIGURE 1: (a) Variation of strain components and (b) corresponding stress components

calculated from the temporal variation of strain at each point using viscoelastic constitutive equations.[13] Here, it is necessary to consider the time dependence of Poisson's ratio. In generating the compliance matrix **A**, analyses are performed by applying unit concentrated loads; however, if the Poisson's ratio used in this analysis is not correct, the superposition of displacements cannot be performed accurately. Since the Poisson's ratio of viscoelastic materials exhibits time dependence,[14] the displacement components u'_{ij} and v'_{ij} obtained by applying unit loads must be calculated using viscoelastic analysis, and the matrix **A** must be constructed at each time step.

Validation of Effectiveness

To validate the effectiveness of the proposed method, displacement distributions obtained by FEA are used as input in place of measured values. The viscoelastic material properties of acrylic reported by Schapery et al.[15] are used, and converted to a temperature of 463 K using the WLF time–temperature superposition principle.[16]

A constant displacement rate of 0.1 mm/s is applied to the top of the 20 mm × 10 mm model for 10 seconds. Displacement distributions within a central region of 6 mm × 6 mm are extracted every second and used as simulated measurement data. The two-dimensional finite element model consisted of 8-node quadratic elements, with 200 elements and 666 nodes. For the analysis region of 6 mm × 6 mm, a separate finite element model is constructed using 8-node quadratic elements with 36 elements and 133 nodes. The same material properties and temperature are used. Unit concentrated loads are applied in the x and y directions at boundary nodes, and viscoelastic analyses are performed to obtain time-dependent displacement and strain distributions. By repeating this procedure for different load positions and directions, the matrix **A** is constructed at each time step. The number of boundary load conditions is $N = 93$, and the number of data points is $M = 900$. Since no measurement error is assumed in this simulation, regularization is not applied.

Stress values in the proposed method are calculated from the temporal variation of strain components using history integration, where Simpson's rule is employed for numerical integration. **Figure 1** shows the time variation of strain components at a certain point and the corresponding stress components calculated from them. As shown in **Fig. 1**, the strains and stresses obtained by the proposed method agree well with the exact solutions, demonstrating that the proposed method can accurately determine strain and stress in viscoelastic bodies.

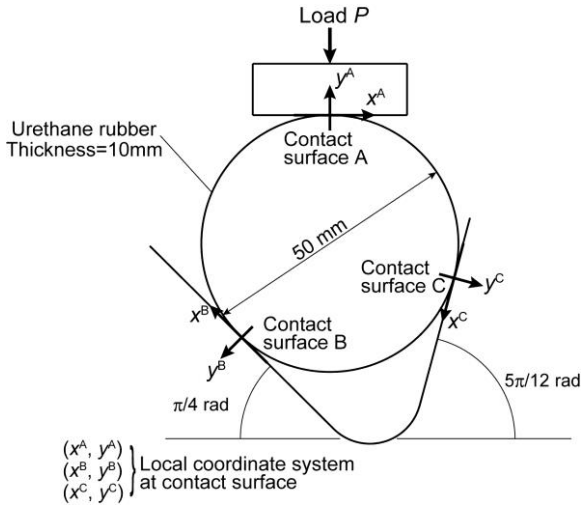

FIGURE 2: Specimen and loading condition for contact stress analysis

APPLICATION TO CONTACT PROBLEMS IN VISCOELASTIC BODIES

Experimental Method

Contact problems are generally difficult because boundary conditions at contact surfaces are not well known, resulting in low reliability of direct FEA. For example, at a contact interface, regions of slip and stick coexist, and these cannot be determined solely from a friction coefficient, making it difficult to accurately evaluate contact stress distributions.[17] In contrast, the proposed method allows boundary loads, including those on contact surfaces, to be obtained from internal measurement data through inverse analysis. That is, it becomes possible to determine load distributions on contact surfaces. In this section, an example of stress evaluation near contact regions in a viscoelastic body using the proposed method is presented.

Figure 2 shows the specimen and loading conditions used. The specimen is a circular disk made of polyurethane rubber. A random speckle pattern is applied to the specimen surface using black and white spray to enable displacement measurement by DIC. The relaxation bulk modulus and shear modulus of the material are determined using the virtual fields method.[18]

Using the loading fixture shown in the figure, three types of contact conditions—normal and shear loading—can be realized.[19] Independent coordinate systems are defined at each contact point. The experiment is conducted in a temperature-controlled chamber at 265 K, and the specimen is compressed vertically at a constant displacement rate of 0.045 mm/s. Images near the contact surface are captured at 1 frame/s using a monochrome CMOS camera with a resolution of 2048 × 2048 pixels (8-bit). A macro lens with a focal length of 200 mm and an aperture of f/11 is used. For DIC analysis, subsets of 31 × 31 pixels are used, with bicubic interpolation, a first-order shape function, and a step size of 5 pixels. Displacement and displacement gradients are obtained using the Newton–Raphson method.[20]

Experimental Results

Figure 3 shows examples of images obtained near each contact surface, displaying a region of 1600 × 1600 pixels. As shown, a region of 10 mm × 5.5 mm including the contact surface is used as the analysis area. **Figure** 4 shows the displacement distribution obtained by DIC near contact surface A at t = 40 s. Using the displacement distributions obtained every second as input, stress analysis near the contact region is performed using the proposed method. Unit concentrated loads are applied in the x and y directions at each boundary node of a finite element

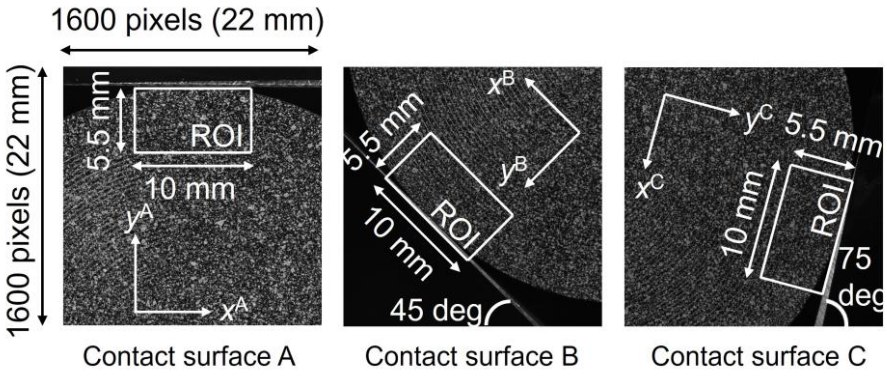

FIGURE 3: Images around contact surfaces

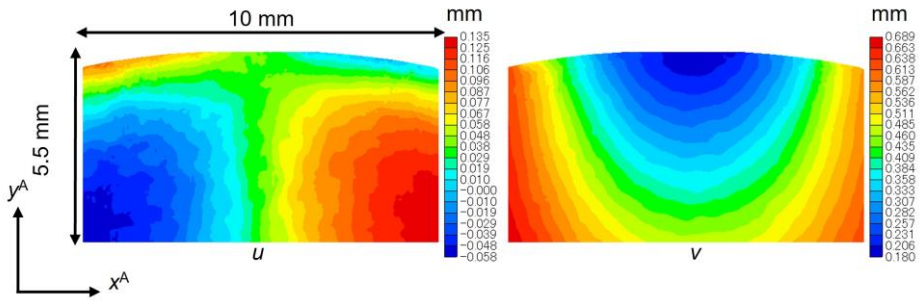

FIGURE 4: Displacement distributions around contact surface A (t = 40 s)

model, and time-dependent displacement distributions are computed to construct the matrix **A**. The regularization parameter is selected as $\alpha = 0.01$.

Figure 5 shows the strain distribution at t = 40 s and the corresponding stress distribution obtained from the temporal strain history. Since contact surface A is subjected to normal loading, the strain and stress distributions are symmetric. Although the boundary conditions of the specimen are asymmetric, the analyzed region is a local region near contact surface A and sufficiently far from other contact surfaces B and C. Therefore, the stress and strain states in this region are dominated by the boundary conditions at contact surface A, and the observed symmetry is reasonable. Focusing on the normal stress component, the maximum compressive stress does not necessarily occur at the center of the contact surface but is distributed nearly uniformly or appears slightly off-center. On the other hand, the maximum compressive strain occurs at the center. This is attributed to earlier loading initiation at the center, leading to more advanced stress relaxation compared to surrounding regions.Furthermore, in normal contact, sticking occurs at the center while slipping occurs in surrounding regions, which also influences the stress distribution.

Figure 6 shows stress distributions near contact surfaces B and C at t = 40 s. Under tangential loading, stress distributions are significantly skewed compared to those under normal loading, and exhibit complex patterns. Since stress varies significantly along the contact surface, it is inferred that regions of stick and slip coexist, similar to the case of normal contact. These regions may potentially be identified from the strain and stress distributions obtained by the proposed method, which will be investigated in future work.

CONCLUSIONS

In this study, a hybrid experimental–numerical method is proposed for obtaining strain and stress distributions in viscoelastic bodies. In this method, boundary conditions in the

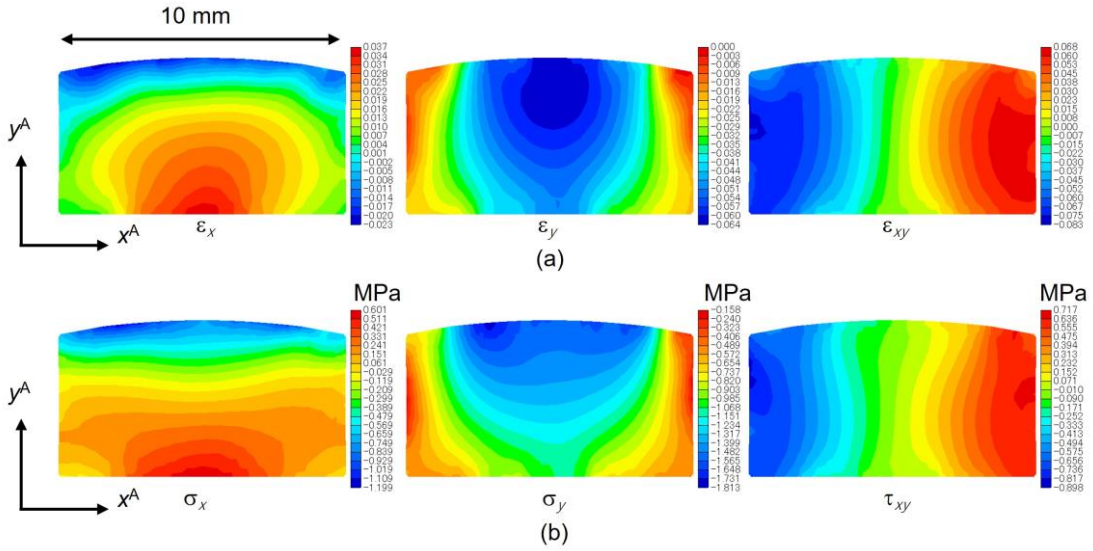

FIGURE 5: (a) Strain distributions and (b) stress distributions at contact surface A obtained by the proposed method (t = 40 s)

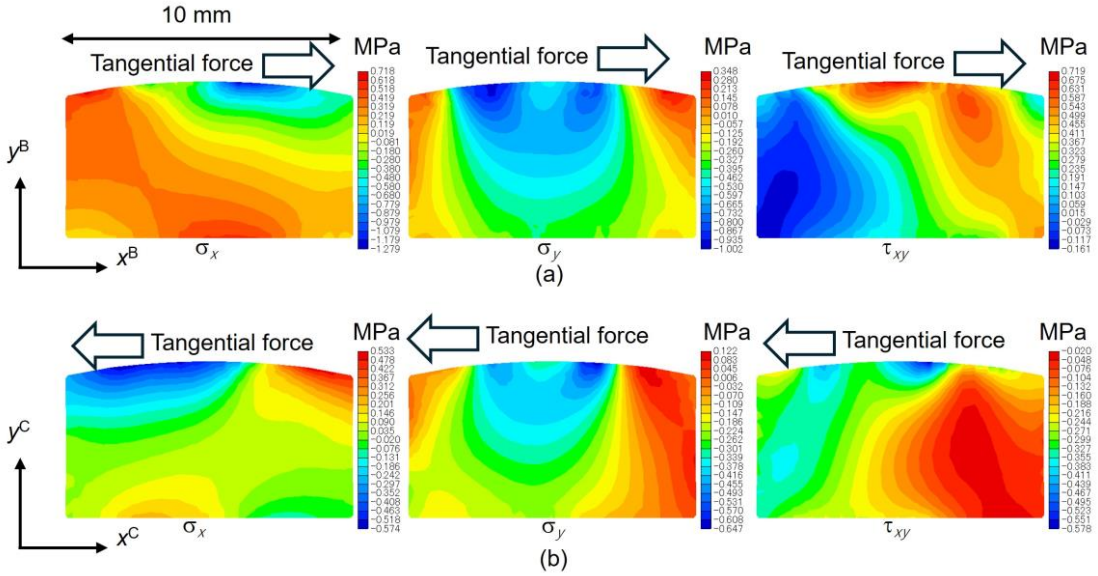

FIGURE 6: Stress distributions around (a) contact surface B and (b) contact surface C obtained by the proposed method (t = 40 s)

measurement region are determined by inverse analysis so that displacement distributions obtained by measurement are reproduced. Regularization is introduced to reduce the influence of measurement errors. As a result, strain distributions can be obtained simultaneously with displacement fields. Since stress evaluation in viscoelastic bodies requires consideration of time-dependent material properties, stress is calculated from the temporal variation of strain using history integration. As examples of the application, contact problems in viscoelastic bodies is demonstrated. In full-field measurement methods such as DIC and moiré, the measured quantity is displacement, and strain must be obtained by differentiation, which

amplifies errors. In viscoelastic materials, stress must further be calculated from the temporal variation of strain, leading to cumulative errors and difficulty in achieving high accuracy. The proposed method overcomes these difficulties and is effective for stress and strain analysis of viscoelastic bodies.

ACKNOWLEDGEMENT

The authors appreciate financial support from the Research Instutite at Aoyama Gakuin University.

REFERENCES

1. Knauss, W.G. A review of Fracture in Viscoelastic Materials. *Int. J. Fract.* **2015**, 196, 99−146. https://doi.org/10.1007/s10704-015-0058-6
2. Yoneyama, S. and Takashi, M. Quantitative Characterization of Cracks and Contact Stresses Using Photoviscoelasticity. In *Advances in Mechanics of Time-Dependent Materials* (Altenbach, H., Kaplunov, J., Lu, H. and Nakada, M. eds.), Springer, 2023, 215−247. https://doi.org/10.1007/978-3-031-22401-0_13
3. Shull, K.R. Contact Mechanics and the Adhesion of Soft Solids. *Mater. Sci. Eng.* **2002**, 36, 1−45.
4 Post, D., Han, B. and Ifju, P. *High Sensitivity Moiré*. Springer, 1994.
5. Sutton, M.A., Orteu, J.-J. and Schreier, H.W. *Image Correlation for Shape, Motion and Deformation Measurement*. Springer, 2009.
6. Yoneyama, S. Computing Strain Distributions from Measured Displacements on a Three-dimensional Surface. *J. JSEM* **2010**, 10, 113−118. https://doi.org/10.11395/jjsem.10.s113
7. Segalman, D.J., Woyak, D.B. and Rowlands, R.E. Smooth Spline-like Finite-element Differentiation of Full-field Experimental Data Over Arbitrary Geometry. *Exp. Mech.* **1979**, 19, 429−437. https://doi.org/10.1007/BF02326046
8. Yoneyama, S. Smoothing Measured Displacements and Computing Strains Utilizing Finite Element Method. *Strain* **2011**, 47, 258−266. https://doi.org/10.1111/j.1475-1305.2010.00765.x
9. Sutton, M.A., Turner, J.L., Bruck, H. and Chae, T.A. Full-field Representation of Discretely Sampled Surface Deformation for Displacement and Strain Analysis. *Exp. Mech.* **1991**, 31, 168−177. https://doi.org/10.1007/BF02327571
10. Nishioka, T., Kurio, K. and Nakabayashi, H. An Intelligent Hybrid Method to Automatically Detect and Eliminate Experimental Measurement Errors for Linear Elastic Deformation Fields. *Exp. Mech.* **2000**, 40, 170−179. https://doi.org/10.1007/BF02325043
11. Yoneyama, S. and Arikawa, S. Identification of Boundary Condition from Measured Displacements for Linear Elastic Deformation Fields. *Procedia IUTAM* **2012**, 4, 215−226. https://doi.org/10.1016/j.piutam.2012.05.023
12. Kubo, S. *Inverse Problems* (in Japanese), Baifukan,1992.
13. Christensen, R.M. *Theory of Viscoelasticity*, 2nd ed., Elsevier, 1982.
14. Hoshino, Y., Tamai, K., Zhang, Y. and Yoneyama, S. Direct Measurement and Master Curve Construction of Viscoelastic Poisson's ratio with Digital Image Correlation. *Strain* **2018**, 54, e12294. https://doi.org/10.1111/str.12294
15. Parks, S.W. and Shapery, R.A. Methods of Interconversion between Linear Viscoelastic Material Functions. Part I—A Numerical Method Based on Prony Series. *Int. J. Solids Struct.* **1999**, 36, 1653−1675. https://doi.org/10.1016/S0020-7683(98)00055-9
16. Williams, M.L., Landel, R.F. and Ferry, J.D. The Temperature Dependence of Relaxation Mechanisms in Amorphous Polymers and Other Glass-forming Liquids. *J. Am. Chem. Soc.* **1955**, 77, 3701−3707. https://doi.org/10.1021/JA01619A008
17. Johnson, K.L. *Contact Mechanics*, Cambridge University Press, 1985.
18. Sun, D., Taguchi, S., Niki, I., Iizuka, K. and Yoneyama, S., The Virtual Fields Method for Identifying Viscoelastic Properties Based on Stress Sensitivity Virtual Fields. *Mech. Time-depend. Mater.* **2025**, 29, 43. https://doi.org/10.1007/s11043-025-09781-0
19. Yoneyama, S., Arikawa, S. and Kobayashi, Y. Linear and Nonlinear Algorithms for Stress Separation in Photoelasticity, *Exp. Mech.* **2012**, 52, 529−538. https://doi.org/10.1007/s11340-011-9512-1

20. Yoneyama, S. Basic Principle of Digital Image Correlation for In-plane Displacement and Strain Measurement, *Adv. Compos. Mater.* **2016**, 25, 105−123. https://doi.org/10.1080/09243046.2015.1129681

ENERGY DISSIPATION IN COMPLEX TIME-DEPENDENT INTERACTIONS

Simon Oman[1], Sanel Avdić[1], Igor Emri[2], Jernej Klemenc[1] and Marko Nagode[1]

[1]University of Ljubljana, Faculty of Mechanical Engineering, 1000 Ljubljana, Slovenia
[2] Zhejiang Tiantie Science&Technology Co., Ltd, Tiantai, Zhejiang, China

DOI: 10.31265/6q8as012

ABSTRACT

Granular damping elements (GDEs) are promising tunable systems for energy absorption, vibration isolation, and damping applications. Their behaviour is governed by complex particle–particle interactions, including frictional sliding, inelastic collisions, and the formation of force-chain networks. This study investigates the influence of particle properties and casing stiffness on the static and dynamic response of GDEs using a combined approach of Discrete Element Method (DEM) simulations and experiments. Numerical simulations were conducted on monodisperse assemblies of metallic-like and polymer-like particles with varying diameters. The results show that energy dissipation is strongly linked to the evolving contact network topology, coordination number, sliding ratio, and particle compliance. Although softer particles exhibit higher absolute energy dissipation due to increased deformation, the specific damping capacity remains relatively consistent across cases, suggesting that frictional contact mechanics dominate the dissipation process. Experimental tests were performed using catenoidal thermoplastic polyurethane (TPU) casings of different wall thicknesses filled with glass beads. The results indicate that casing stiffness significantly influences both dynamic stiffness and damping behaviour. More compliant casings allow greater relative particle motion, leading to increased energy dissipation. However, they also exhibit higher dynamic stiffness, which in turn affects the system's natural frequency. Overall, the findings demonstrate that dynamic stiffness and damping in GDE systems are inherently coupled and cannot be independently optimised. These results provide valuable insights for the design of next-generation granular damping systems with enhanced and tunable energy dissipation performance.

INTRODUCTION

Energy absorption and dissipation are leading mechanisms behind many beneficial technologies. Their use in critical systems (transportation, industrial machinery, power plants, etc.) and infrastructure (buildings, roads, railways, etc.) is foundational to enhancing safety, performance, efficiency, and well-being in modern society. Nonetheless, existing state-of-the-art technologies often fall short in at least one of the key areas: performance, efficiency, sustainability, and adaptability. These systems frequently have limited energy absorption and dissipation capabilities, are typically made from non-recyclable materials, and have a narrow scope of applicability. The economic impact of these inefficiencies is significant, with losses from earthquakes, vibration-related industrial downtime, reduced turbine efficiency, transport

disruptions, and health-related costs collectively reaching billions to hundreds of billions of dollars.

Tunable granular damping elements (GDEs) represent a transformative approach to energy absorption and dissipation. As an emerging class of new damping systems generation, they can be specifically tailored to achieve desired behaviour: shock absorption, energy dissipation, sound insulation, vibration isolation and damping, energy harvesting and so on. GDEs are structured assemblies of particles that interact through contact forces, which can include elastic, plastic, frictional, or dissipative interactions[1,2] and can also provide load-bearing capacity via tunable mechanical properties such as elastic, shear, and bulk moduli[3]. By adjusting particle size, shape, material, and arrangement, their behaviour can be effectively "programmed" under external loading. In some configurations, granular materials enclosed in elastic containers have demonstrated up to 10× improvements in vibration damping compared to current state-of-the-art solutions[3].

GDEs have broad potential across civil engineering (earthquake protection and infrastructure damping), transportation (rail vibration reduction), manufacturing (machine isolation), automotive and aerospace (crash protection and adaptive damping), defence (blast mitigation), medical devices (prosthetics and surgical tools), and energy systems (improved turbine stability and energy harvesting). They also support green transition[4] and circular economy goals by enabling reuse of waste materials such as tires, conveyor belts, and composites, as well as the use of abundant natural granular materials like gravel.

Compared to metamaterials with complex geometries or polymer-based damping systems, GDEs rely on force chain formation, friction, inelastic particle collisions, and internal material dissipation like shown in Fig. 1. **Energy dissipation in GDE systems emerges from transient evolution of force-chain topology under constrained relative particle motion**. Therefore, by simply filling elastic structures with granules can significantly enhance energy absorption and dissipation. Prior research on granular damping systems has shown 10–100× performance improvements[5] over bulk material approaches due to pressure-dependent changes in stiffness and damping within confined granular media. However, accurately predicting and optimizing custom-designed GDE behaviour still requires deeper understanding of their underlying mechanisms.

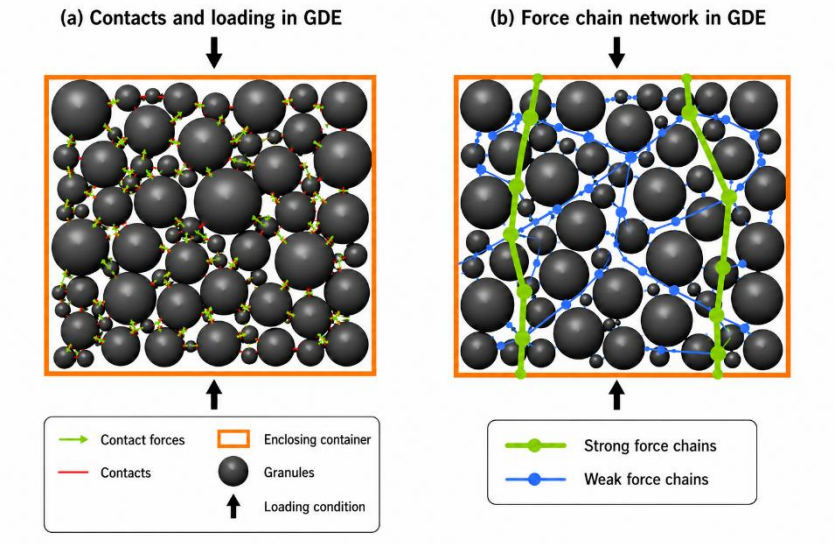

FIGURE 1: Main energy absorbing and damping mechanisms in GDEs.

This research will present the influence of particle parameters and GDE casing stiffness to the GDE static and dynamic stiffness and damping capabilities. The research is based on DEM simulations in combination with the experimental results.

DEM SIMULATIONS

The numerical analysis consisted of uniaxial compression simulations performed on monodisperse sphere assemblies confined within a rigid cylindrical specimen of 20 mm diameter and approximately 50 mm height, corresponding to an aspect ratio of 2.5. Two materials were considered: metallic-like (M1, E=80 GPa) and polymer-like (M2, E=3.5 GPa), representing a stiff-to-compliant material pair with an elastic modulus ratio of approximately 23. Poisson's ratios were 0.3 and 0.38 for M1 and M2 respectively, and the inter-particle friction coefficient was set to 0.3 for both materials. To enable direct comparison of material effects at equivalent contact network topology, the number of particles was kept the same between both materials for each diameter: 18000 spheres for the 1 mm cases and 2250 spheres for the 2 mm cases. For the polymer-like assemblies (M2), this corresponds to a total mass of approximately 13.4 g for both diameters. For metallic-like assemblies (M1), the identical particle counts yield a substantially higher mass of approximately 74.0 g, reflecting the density ratio of the two materials (7850 kg/m^3 versus 1420 kg/m^3). For each material and diameter combination, four quantities were extracted from the stabilised fifth loading cycle: assembly stiffness C, specific damping capacity η, coordination number Z, and sliding ratio S. The stiffness is defined as the slope of the loading curve and is calculated based on the maximum and minimum compressive forces (Fmax and Fmin) and displacements (dmax and dmin) of the rigid plate. Specific damping capacity is defined as the ratio of the dissipated energy ΔU (which corresponds to the area enclosed by the hysteresis loop on a force–displacement diagram) and the maximum possible reversible energy of the system U. The coordination number is defined as the average number of contacts per particle, while the sliding ratio represents the fraction of sliding contacts (contacts for which the tangential force exceeds the Coulumb sliding treshlod). Together, these four parameters provide a coupled macroscopic and contact-level characterisation of the dynamic response.

The mechanical response of the four granular assemblies was characterised through force-displacement (F-d) curves recorded over five uniaxial compression cycles. Assembly stiffness and specific damping capacity were extracted from the stabilised fifth cycle, while the coordination number and sliding ratio were tracked as functions of applied compression force to provide contact-level insight into the observed macroscopic behaviour.

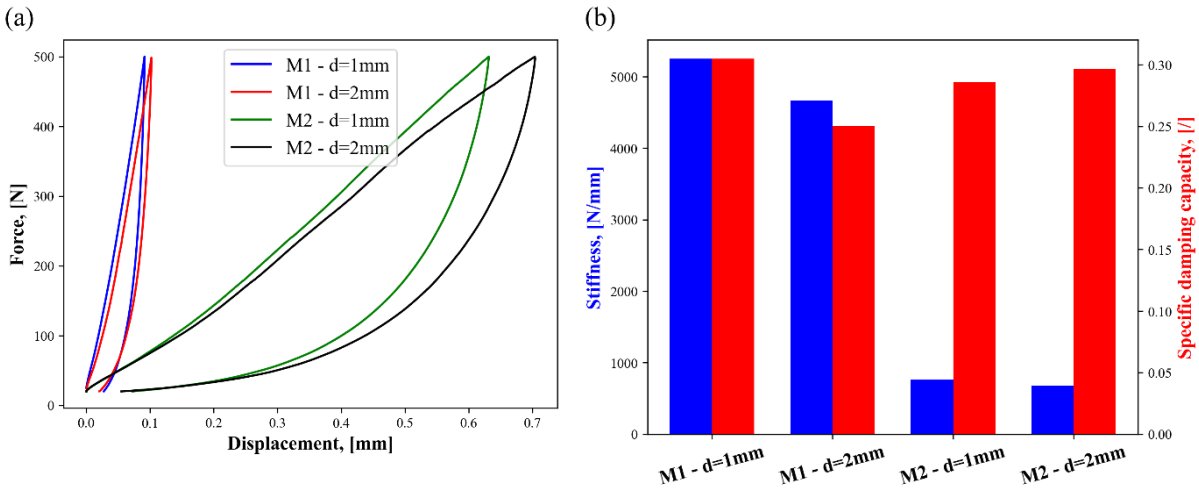

FIGURE 2: (a) Force-displacement curves, (b) stiffness and specific damping capacity

The F-d curves in Figure 2(a) reveal a strong material dependence in both compliance and energy dissipation. M1 assemblies exhibit near-vertical loading branches, reaching 500 N within approximately 0.092 mm (1 mm) and 0.11 mm (2 mm), while M2 assemblies require displacements up to 0.63 mm and 0.70 mm, respectively. The substantially wider hysteresis loops of M2 immediately suggest higher energy dissipation per cycle, yet the quantified specific damping capacity given in Figure 2(b) reveals that η values range only from 0.250 to 0.305 across all four cases. This narrow spread indicates that the dissipation fraction, energy lost relative to maximum potential elastic energy, is governed primarily by contact-level friction mechanics rather than bulk compliance, since the large difference in stiffness between M1 and M2 does not translate into a proportionally large difference in specific damping capacity. The absolute energy dissipated per cycle is, however, far greater for M2 due to its much larger displacement amplitude at the same force level.

The stiffness shows a clear material-driven hierarchy (M1 approximately seven times stiffer than M2) and a consistent, material-independent size effect, 1 mm assemblies are approximately 12% stiffer than their 2 mm counterparts for both materials. This size effect is directly correlated with the coordination number data in Figure 3(a), where 1 mm assemblies maintain higher Z values throughout loading, reaching approximately 4.55 versus 4.30 for M1, and 5.25 versus 5.00 for M2 at 500 N. The denser contact network in smaller-particle assemblies provides more parallel load-bearing paths, explaining the stiffness increase. Importantly, M2 assemblies exhibit consistently higher coordination numbers than M1 across the entire loading range. This reflects the greater compliance of M2 contacts. At any given force level, M2 contacts deform more, increasing the likelihood of new contact formation and sustaining a richer force-chain network.

The coordination number data also explain the evolution of the sliding ratio in Figure 3(b). All assemblies show a sharp drop in sliding ratio from approximately 0.26–0.28 at 5 N to a minimum near 0.14–0.16 at 100 N. This transition coincides with the steep rise in Z in the same force range, confirming that rapid contact formation redistributes the applied load across an expanding network, bringing individual contacts away from their Coulomb sliding threshold. Beyond 100 N, Z grows more gradually and the sliding ratio recovers steadily, indicating that newly formed contacts are progressively loaded toward sliding. Critically, M1 assemblies reach significantly higher sliding ratios at peak compression (~0.23–0.24) compared to M2 (~0.14–0.18).

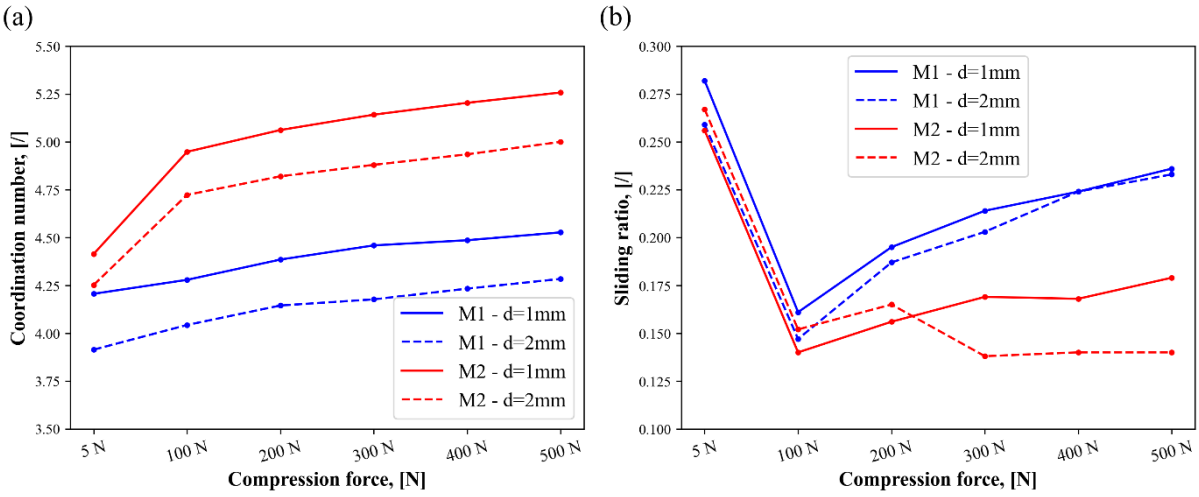

FIGURE 3: (a) Coordination number, (b) sliding ratio

This inverse correlation between coordination number and sliding ratio across the two materials is physically consistent, suggesting that the higher Z in M2 distributes load more uniformly, keeping a greater fraction of contacts below the frictional limit. For M1, the lower Z concentrates force on fewer contacts, driving more of them into sliding which is a mechanism that directly links contact network topology to frictional activity. The relationship between contact network topology and η is clearest within the M1 assemblies. Despite M1 d=1 mm and M1 d=2 mm exhibiting nearly identical sliding ratios at peak load (~0.23), their specific damping capacities differ noticeably (0.305 versus 0.250). This is better explained by their coordination numbers: the higher Z of the 1 mm assembly (~4.55 versus ~4.30 at 500 N) provides more active contacts contributing to micro-slip, increasing the total dissipated energy without a proportional increase in stored energy. For M2 assemblies, the size effect operates differently: M2 d=2 mm has both a lower sliding ratio and lower Z than M2 d=1 mm at peak load, yet records the higher η (0.297 versus 0.286). Here the greater contact deformation of the more compliant 2 mm spheres amplifies the tangential micro-slip amplitude at each contact, offsetting the sparser contact network. Taken together, these results indicate that specific damping capacity is not controlled by a single contact-level quantity, but by the interplay between contact network density, captured by coordination number, and per-contact deformation, which scales with particle compliance.

EXPERIMENTAL SECTION

The numerical DEM results show that the amount of dissipated energy within the GDE element is strongly related to its stiffness. In our previous studies[6] we demonstrated that the magnitude of dissipated energy is most significantly influenced by friction between the granules as well, which simultaneously also affects stiffness. For this reason, optimal specific damping capacity requires an appropriate level of friction that enables good flowability, or relative movement between the granules during loading, while at the same time ensuring sufficient energy loss due to sliding between them.

To increase the possibility of relative movement between the granules during loading, it is necessary to provide an elastic casing for the GDE element. Since the DEM analysis presented in the previous chapter does not allow simulations with elastic boundary elements, this chapter

presents the influence of casing stiffness on the dynamic stiffness and the specific damping capacity of the GDE through experimental results.

To show the influence of the stiffness of the GDE casing on its characteristics a catenoidal shape of GDE casing with three different thicknesses (0.8, 1.2 and 1.6 mm) was selected and experimentally validated. GDE casings were 3D printed from soft TPU material and filled with glass beads of Mesh #20 size with some additional Vaseline added to decrease the friction between the beads. Simple 3D printed parts were used to cover the bottom part of the GDE casings after filling it with granulate. Bottoms were glued to TPU casings using a super glue. The shape of the sample is presented in Figure 4.

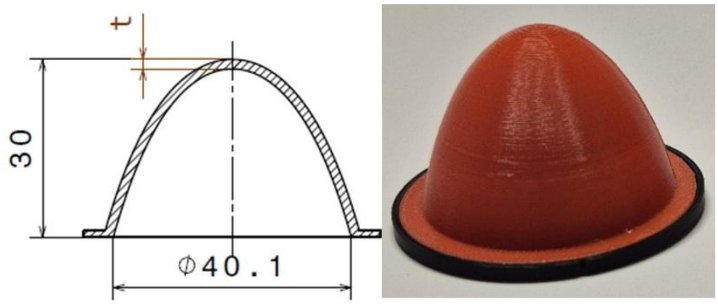

FIGURE 4: Shape of GDE element used for experimental evaluation

To check how dynamic stiffness and specific damping capacity change with static preload, several different preloads have been used (50, 100, 150, 200, 250, 300, 400, 500 and 600 N) on which cyclic loading with constant displacement amplitude of 0.125 mm has been added (10 cycles at each preload). The processed experimental results are shown in two graphs in Figure 5.

Results for all investigated specimens show that dynamic stiffness increases progressively with the preload. Due to the progressive characteristics of the catenoid, such results are expected. If we look more closely at the specific damping capacity results, we can find that it is maximal at a specific preload of the test specimen, which, however, varies from test specimen to test specimen. A closer examination of the obtained results reveals that the optimal specific damping capacity for a given catenoidal shape occurs at approximately the same static height. However, since the static stiffness is conditioned by the thickness of the shell, the optimal height for samples with different thicknesses is obtained at different static loads. The optimal preload height for used shape is around 21 mm (9 mm compressed sample).

If specific damping capacities are further compared, it is observed that the highest values are found in the samples with the lowest wall thickness, which are also characterized by the greatest elasticity in terms of their static behaviour. Combining these findings, we can conclude that in order to ensure the optimal shape and consequently characteristics (best specific damping capacity), it is important to properly adapt the damping element to the static load, which can be done by optimizing the thickness and geometry of the GDE casing or the stiffness of the material from which it is made.

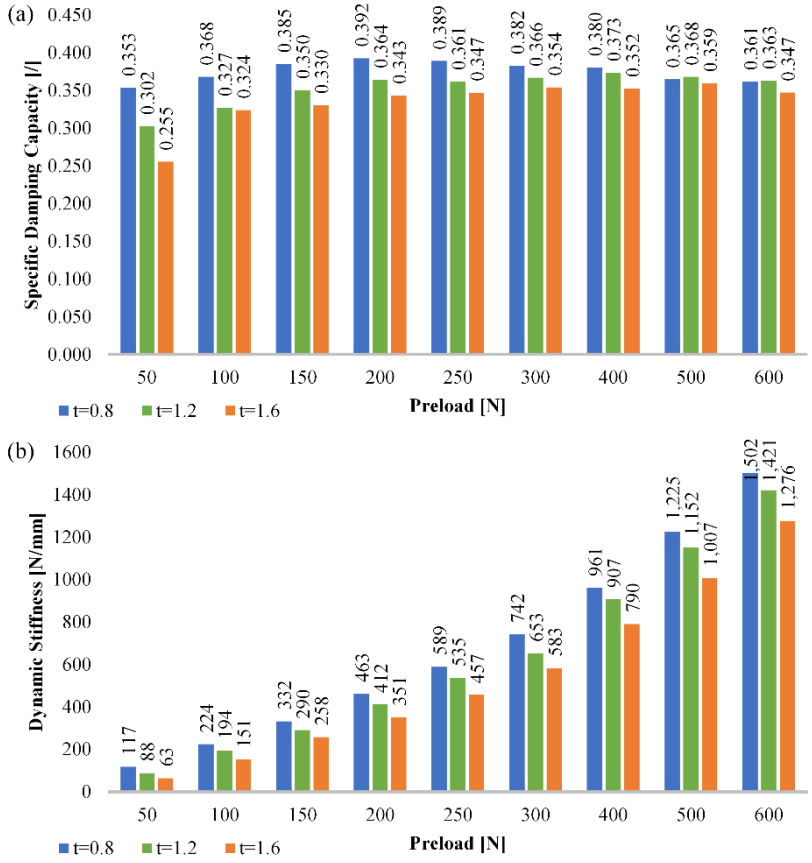

FIGURE 5: Experimental results: (a) Specific Damping Capacity, (b) Dynamic Stiffness

A very important finding from these results is that the dynamic stiffness of samples with lower static stiffness is higher than those with higher static stiffness. This is partly related to the fact that the height of the sample on which the dynamic loading is performed is different between samples. For samples with lower static stiffness, it is already shifted more into the progressively increasing part of the stiffness curve, while for samples with higher static stiffness it can remain in the flatter part of the curve. The second part for this phenomenon is related to the fact that in samples with lower stiffness the proportion of damping compared to stiffness is higher, which results in much steeper unloading curve of the Force-Displacement characteristic and consequently higher dynamic stiffness. This indicates that stiffness and damping are closely related and therefore cannot be independently controlled at the level of an individual GDE element.

CONCLUSIONS

This study investigated the energy dissipation mechanisms and dynamic behaviour of granular damping elements (GDEs) using a combination of DEM simulations and experimental analysis. The obtained results demonstrate that the damping performance of GDE systems is governed by the complex interplay between particle-scale contact mechanics and the global stiffness of the enclosing structure. The presented results also indicate that the behaviour of granular damping systems cannot be fully understood through bulk constitutive descriptions alone, but requires explicit consideration of evolving contact-network topology and constrained particle kinematics.

The numerical simulations showed that the amount of dissipated energy is strongly related to the contact network topology, coordination number, sliding ratio, and particle compliance. Softer materials exhibit significantly larger deformation amplitudes and therefore greater absolute energy dissipation. However, the specific damping capacity is governed predominantly by frictional interactions at particle contacts, indicating that the damping behaviour originates primarily from transient internal reconfiguration processes within the granular contact network.

The experimental investigation confirmed that the stiffness of the elastic GDE casing has a major influence on the dynamic response of GDE elements. Softer casings allow greater relative movement between granules, resulting in improved specific damping capacity. The results further revealed that the optimal specific damping capacity is achieved at a specific static preload level corresponding to an optimal compressed height of the element. This indicates that the geometry, wall thickness, and material properties of the casing must be carefully adapted to the expected operating conditions.

An important finding of this work is that specific damping capacity and dynamic stiffness are strongly coupled properties and therefore cannot be independently controlled at the level of an individual GDE element. Consequently, achieving optimal performance requires simultaneous optimization of particle properties, inter-particle friction, particle size, casing geometry, and casing stiffness.

The presented results contribute to a better understanding of complex time-dependent interactions in granular systems and provide a foundation for the development of advanced tunable damping solutions for applications in civil engineering, transportation, manufacturing, energy systems, and vibration-sensitive technologies.

ACKNOWLEDGMENTS

The authors would like to thank the Slovenian Research Agency (P2-0182, Development evaluation) and Zhejiang Tiantie Industry Co Ltd for providing financial and material support.

REFERENCES

1. Jaeger, H.M.; Nagel, S.R. Physics of the Granular State. Science 1992, 255, 1523–1531.
2. Venkatesh, R.; Brojan, M.; Emri, I.; Voloshin, A.; Govekar, E. Influence of Particle Size Distribution Width on GFA Index of Uniaxially Compressed Granular Materials. Powder Technology 2021, 377, 666–675.
3. Gosar, A.; Emri, I.; Klemenc, J.; Nagode, M.; Oman, S. On the Vibration-Damping Properties of the Prestressed Polyurethane Granular Material. Polymers 2023, 15, 1299.
4. Plastic pollution is growing relentlessly as waste management and recycling fall short, says OECD | OECD
5. Avdić, S.; Nagode, M.; Klemenc, J.; Oman, S. Experimental Evaluation of a Granular Damping Element. Polymers 2024, 16, 1440.
6. Avdić, S.; Nagode, M.; Klemenc, J.; Emri, I.; Oman, S. The influence of inter-particle friction on multiscale response of uniaxially loaded granular material. Journal of Materials Research and Technology 2025, 38, 3208-3217.

BACKWARD INCREMENTAL DIGITAL VOLUME CORRELATION FOR HIGH-FIDELITY INTERNAL DEFORMATION MAPPING IN IDOX/ESTANE PARTICULATE COMPOSITES

Ehsan Mehrdad[1], Pooyan Brandon Javadzadeh[1], Yao Ren[1], Nathan Peterson[2], Amy Clarke[2], Richard Regueiro[3], Alex K Arzoumanidis[4], Brian K Bay[5], Hongbing Lu[1*]

[1] Department of Mechanical Engineering, The University of Texas at Dallas, 800 W. Campbell Street, Richardson 75080, TX, USA
[2] Department of Metallurgical and Materials Engineering, Colorado School of Mines, Golden 80401, CO, USA
[3] Department of Civil, Environmental and Architectural Engineering, University of Colorado at Boulder, 1800 Euclid Ave, Boulder 80309, CO, USA
[4] Psylotech Inc., Evanston 60201, IL, USA
[5] School of Mechanical, Industrial, and Manufacturing, Engineering, Oregon State University, Corvallis, OR, USA

DOI: 10.31265/wvmrjm34

ABSTRACT

In-situ X-ray micro-computed tomography (μCT) combined with Digital Volume Correlation (DVC) has become a cornerstone for quantifying internal deformation and damage in particulate composite materials. However, conventional DVC often struggles to maintain accuracy when materials undergo large nonlinear deformations accompanied by severe cracking and structural discontinuity. This paper addresses these limitations by implementing a robust backward incremental DVC approach to analyze the failure mechanisms of a mock plastic-bonded explosive (PBX) composite. The experimental setup involved a cylindrical specimen composed of IDOX crystals (75–150 μm) embedded in a polyurethane-based Estane binder. During unconfined compression, sequential μCT scans were acquired to capture the internal structural evolution. Unlike conventional forward-marching methods, the backward approach performs correlations in reverse, processing from the most deformed and fragmented state back to the original undeformed configuration through incremental steps. This methodology significantly enhances displacement tracking fidelity, particularly in regions where severe cracking and interfacial failure typically cause a loss of correlation in traditional frameworks. The results demonstrate that backward incremental DVC provides superior resolution of displacement and deformation fields near crack-affected regions. This high-fidelity mapping allows for the detailed observation of critical failure stages, including grain-binder interface delamination and subsequent crack coalescence. By successfully capturing these complex, grain-scale interactions, the study provides a vital dataset for the validation of high-fidelity numerical simulations. Ultimately, this approach offers a more reliable pathway for characterizing the intricate mechanical response and fracture evolution of heterogeneous particulate composites under extreme loading conditions.

INTRODUCTION

Quantifying the internal mechanical response and damage evolution of highly filled particulate composites, such as plastic-bonded explosives (PBXs), remains a formidable challenge in experimental mechanics. These energetic materials consist of a high volume fraction of crystalline particles embedded in a soft polymeric binder, a microstructural design intended to optimize both functional output and safe handling [1-3]. Due to the distinct stiffness mismatch between the rigid grains and the compliant binder, the macro-scale structural integrityof PBXs is highly dependent on complex, localized micro-scale interactions [4-6].

To avoid the hazards associated with live explosives, inert surrogate materials such as IDOX/Estane are heavily utilized in experimental characterization, exhibiting mechanical similarity to active composites across various thermal and loading regimes [3, 7-9]. While surface-based optical techniques like Digital Image Correlation (DIC) capture macroscopic failure patterns that eventually reached to the surface of the specimen, understanding subsurface behavior requires three-dimensional internal characterization. In-situ X-ray micro-computed tomography (μCT) coupled with Digital Volume Correlation (DVC) has thus emerged as the premier method for resolving volumetric deformation fields [1, 11].

Despite its advantages, standard DVC algorithms conventionally operate in a forward-marching manner, using the undeformed image as the continuous reference state. When dealing with particulate composites under compressive loads, severe cracking, interface delamination, and subsequent material fragmentation induce significant structural discontinuities. These events frequently cause conventional forward DVC algorithms to decorrelate, losing critical kinematic data exactly where damage localization is most severe. To overcome these fundamental limitations, this study utilizes a backward incremental DVC methodology [1]. By designating the heavily damaged, peak-deformed geometry as the initial reference and stepping backward toward the continuous undeformed state, the technique stabilizes correlation convergence and provides unprecedented resolution of crack coalescence and grain-binder interactions.

MATERIALS AND METHODS

Material Synthesis and Specimen Preparation

A high-fidelity inert surrogate was manufactured using recrystallized IDOX crystals with grain sizes ranging between 75 and 150 μm. These particulates were combined with a polyurethane-based Estane binder at a 19:1 weight ratio, achieving a 95% particle loading density characteristic of high-performance PBX formulations. Following blending, the composite mixture was hot-pressed at 50°C under 152.8 MPa of pressure for a duration of one minute. The compacted billets were subsequently machined into cylindrical specimens with optimized dimensions of 5 mm in both diameter and height, tailored specifically for unconfined compressive testing. (See also FIGURE 1.)

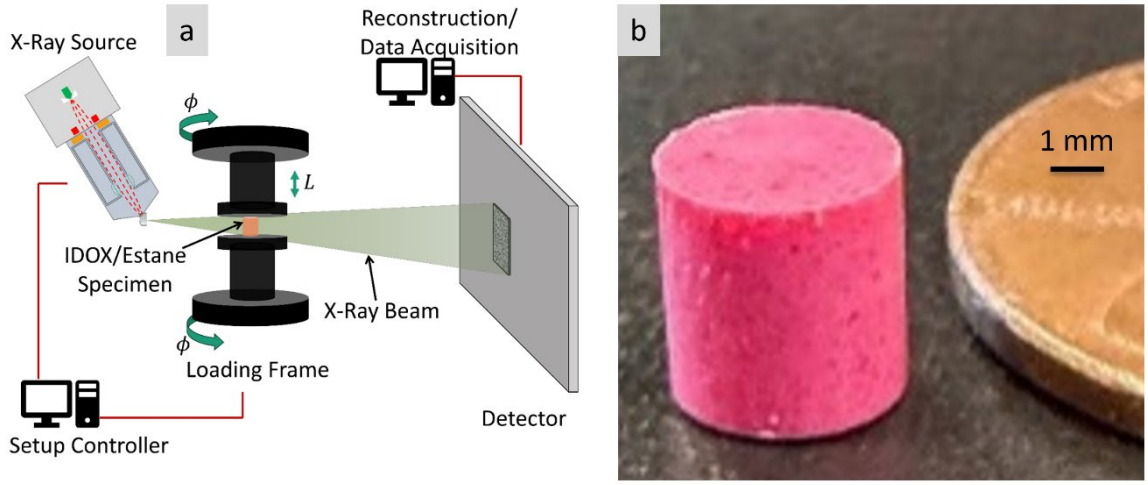

FIGURE 1: (a) Schematic of the in-situ X-ray micro-computed tomography system (b) IDOX/Estane Composite Specimen.

In-Situ Micro-Computed Tomography (μCT) Setup

The compression testing was conducted entirely in-situ within a ZEISS Xradia 520 Versa X-ray microscope, equipped with a customized unconfined compression loading stage. To mitigate frictional barreling artifacts at the boundary interfaces, the top and bottom surfaces of the composite cylinder were lubricated prior to testing. The loading platen compressed the specimen at a quasi-static displacement rate of 0.5 mm/min. Volumetric image datasets were acquired at six specific engineering strain (ϵ_z) intervals: 0.0%, -4.0%, -8.0%, -12.0%, -13.2%, and -14.4%. At each load step, the μCT system captured projections over a full 360° rotation using an X-ray source set to 160 kV and 50.3 μA, with an 8-second exposure time per projection. This procedure yielded highly detailed reconstructions featuring an isotropic voxel resolution of 12.93 μm, which were subsequently cropped to 601x601x501 pixel volumes to streamline computational correlation.

Backward Incremental Digital Volume Correlation

To evaluate the complex internal deformation, an open-source correlation tool (i.e., iDVC) was utilized. A critical advantage of this framework is its reliance on the local correlation of discrete subvolumes, effectively bypassing the need to formulate a global coupled stiffness matrix that frequently destabilizes during severe material fracture. Because standard tracking algorithms fail when cracks open and introduce void spaces, a reverse-tracking scheme was implemented and adopted for partciculate composites with major fracture patterns and fragmentation. In this study, the analytical process began at the maximum compressive strain state ($\epsilon_z = -14.4\%$) and systematically traced material points backward to the pristine, undeformed state (ϵ_z =0.0%). This reverse orientation ensures that control points remain anchored exclusively in solid material. Kinematic data was resolved by minimizing a normalized sum of squared differences (NSSD) function, which evaluates intensity variations between the reference and deformed configurations. The computational analysis employed 40-pixel cubic sub-volumes populated with 10,000 random sampling points. Sub-voxel precision was attained via tricubic interpolation, while the Newton-Raphson numerical method drove the minimization convergence.

RESULTS AND DISCUSSION

The in-situ tomographic scans provided a clear, uninterrupted timeline of internal degradation within the IDOX/Estane specimen. Initially, up to a compressive strain of -4.0%, the composite deformed homogeneously with only minor rigid body rotation and no visible fracturing. The critical damage occurred before -8.0% strain, marked by the rupturing of the polymeric binder, separation at the grain-binder interfaces, and the fracture of individual IDOX crystals. As the compressive load reached the final evaluated state (-14.4%), these isolated defects rapidly expanded and merged. The resulting fracture morphology presented a fragmented fracture profile throughout the specimen. This localized damage divided the cylindrical specimen into a relatively intact inner core surrounded by heavily fragmented peripheral wedges.

Standard forward-marching correlation attempts collapsed during the early stages of crack formation due to the rapid introduction of discontinuities. Conversely, by treating the most severely damaged configuration as the baseline, the backward incremental approach effectively modeled a virtual unloading process. Control points were securely positioned within intact material regions, successfully navigating around the complex crack networks. This method yielded exceptional computational stability; even during the most demanding correlation step where major fractures were virtually closed, the failure rate for control points was a mere 0.23% (representing only 10 points out of 4298). The algorithm maintained high-quality NSSD metrics, processing each load step in 1000 to 2485 seconds using a dual Intel Xeon workstation.

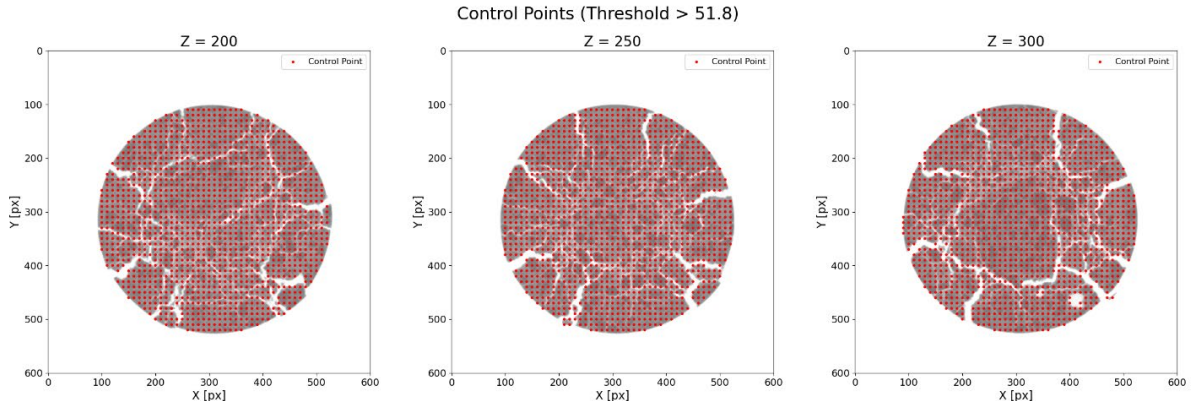

FIGURE 2: The distribution of control points throughout the sample shown in multiple slices.

By mathematically inverting these reverse trajectories, accurate forward-oriented displacement fields were successfully recovered. These 3D maps highlighted severe kinematic disparities across the fractured zones. For instance, following the primary fragmentation event, there is a further expansion in crack morphology in different sections of the sample up to the last step of the compressive strain (i.e., -14.4%). Furthermore, displacement magnitudes in the upper portion of the composite were nearly an order of magnitude greater than those at the fixed base, directly reflecting the downward influence of the moving platen.

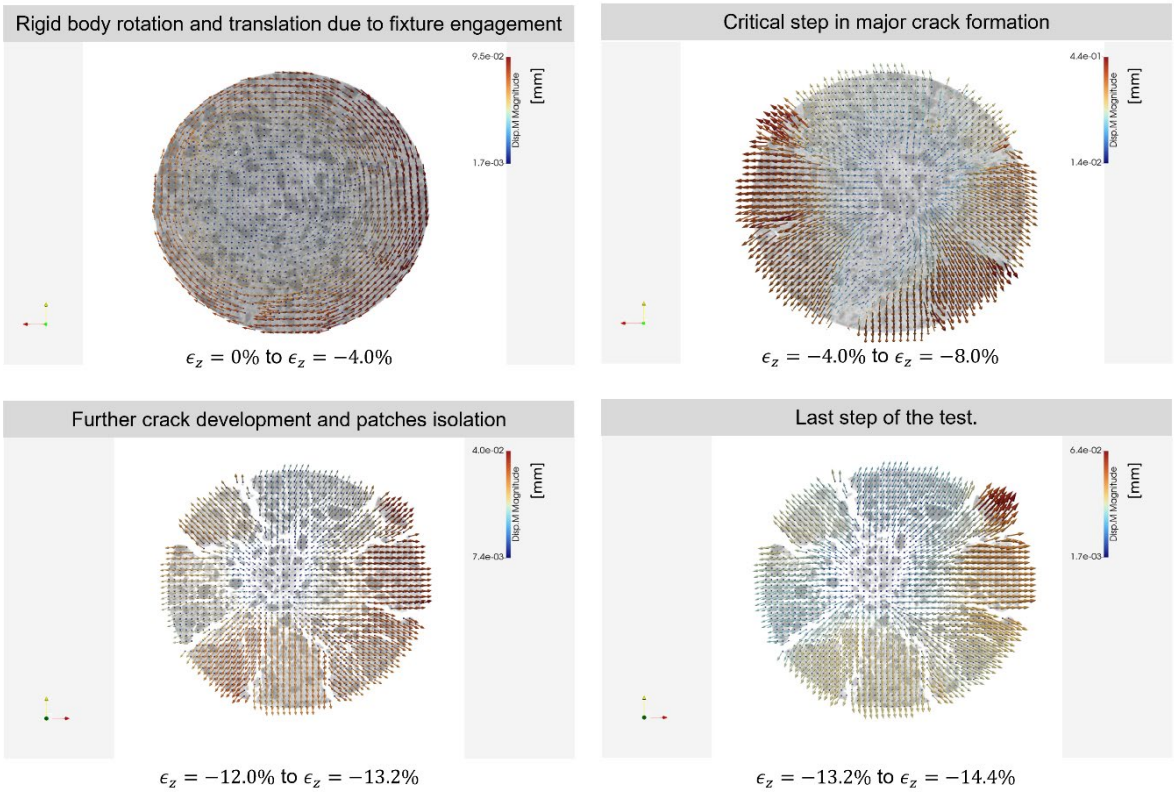

FIGURE 3: Post-processed incremental displacement vector field**.**

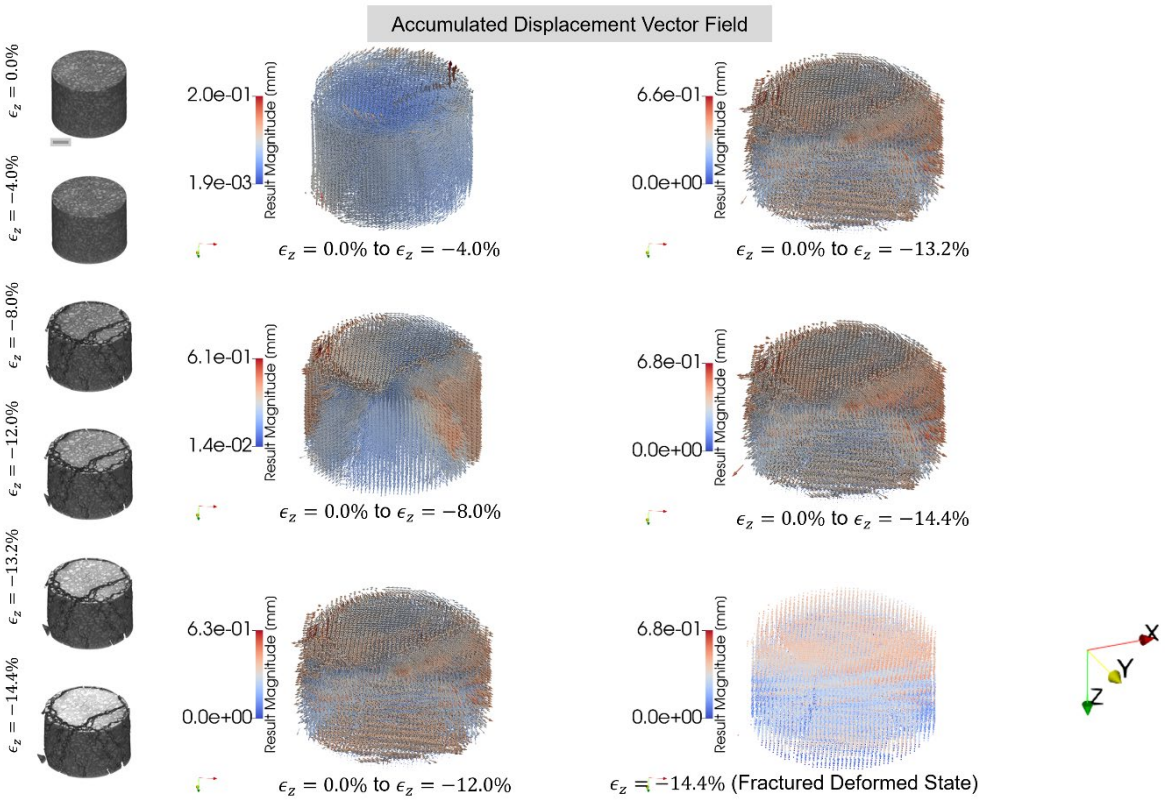

FIGURE 4: Full field cumulative displacement vector field post processed from backward DVC results.

CONCLUSION

This research demonstrates the efficacy of a reverse-marching correlation strategy for mapping the complex internal mechanics of dense particulate systems. Using the IDOX/Estane composite as a structural analog for high-explosive formulations, the study successfully captured the macroscopic shift from uniform viscous flow to catastrophic brittle failure. The analysis identified two distinct failure mechanisms: localized, patchy fracturing driven by microstructural grain interactions, and the eventual development of dominant, shear-driven macroscopic bands.These high-resolution kinematic fields serve as crucial validation targets for advanced multiscale numerical simulations. Subsequent investigations will leverage these 3D datasets to formulate micromechanical damage models and extend the backward tracking methodology to evaluate failure mechanisms in KelF/F50 polymer sand composites under diverse loading regimes.

Bibliography

1. Mehrdad, E., Javadzadeh, P. B., Ren, Y., Peterson, N., Clarke, A., Regueiro, R.; Arzoumanidis, A. K., Bay, B. K., Lu, H. In-Situ Internal Deformation Measurement of an IDOX Particulate Estane Binder Composite via Backward Digital Volume Correlation. Exp. Mech. 2025, 1–17. https://doi.org/10.1007/s11340-025-01253-3.
2. Burch, A. C., Euser, V. K., Morrow, B. M., Cady, C. M., Yeager, J. D. Compressive Strength of the Plastic-Bonded Explosive Surrogate Idoxuridine under Quasistatic and Dynamic Compression. J. Compos. Mater. 2022, 56 (26), 3949–3956. https://doi.org/10.1177/00219983221125904.
3. Thompson, D. G., Deluca, R., Brown, G. W. Time-Temperature Analysis, Tension and Compression in PBXs. J. Energ. Mater. 2012, 30 (4), 299–323. https://doi.org/10.1080/07370652.2011.569831
4. Zhang, C., Jiao, F., Li, H. Crystal Engineering for Creating Low Sensitivity and Highly Energetic Materials. Cryst. Growth Des. 2018, 18 (10), 5713–5726. https://doi.org/10.1021/acs.cgd.8b00929.
5. Thompson, D. G., Wright, W. J. Mechanical Properties from PBX 9501 Pressing Study. In AIP Conference Proceedings; 2004, 706 (1), 503–506. https://doi.org/10.1063/1.1780287.
6. Burch, A. C., Yeager, J. D., Bahr, D. F. Nanoindentation of HMX and Idoxuridine to Determine Mechanical Similarity. Crystals 2017, 7 (11), 335. https://doi.org/10.3390/cryst7110335.
7. Liu, C., Woznick, C. S., Scott, S. J., Duque, A. L., Herman, M. J., Yeager, J. D. Brazilian Disk Compression Testing of Plastic-Bonded Idoxuridine Mock Explosive. J. Energ. Mater. 2023, 41 (3), 319–350. https://doi.org/10.1080/07370652.2021.1968073.
8. Javadzadeh, P. B.; Ren, Y., Peterson, N., Clarke, A. J., Lu, H. Unconfined Uniaxial Compression of Estane Bonded Idoxuridine Under Quasi-Static and High Strain Rate Loading. In SEM Annual Conference and Exposition on Experimental and Applied Mechanics; 2024, 101–108. [https://doi.org/10.1007/978-3-031-85829-1_15].
9. Javadzadeh, P. B., Mehrdad, E., Ren, Y., Peterson, N., Clarke, A., Lu, H. Surface Deformation Measurements of a Composite Cylinder Composed of Particulate Idoxuridine Crystals Embedded in Estane Under Compression. In Dynamic Behavior of Materials, Volume 1; 2025, 15–19. [https://dx.doi.org/10.13052/9788743808275-4].
10. Bay, B. K., Smith, T. S., Fyhrie, D. P., Saad, M. Digital Volume Correlation: Three-Dimensional Strain Mapping Using X-ray Tomography. Exp. Mech. 1999, 39, 217–226. https://doi.org/10.1007/BF02323555.
11. Hu, Z., Luo, H., Bardenhagen, S. G., Siviour, C. R., Armstrong, R. W., Lu, H. Internal Deformation Measurement of Polymer Bonded Sugar in Compression by Digital Volume Correlation of In-situ Tomography. Exp. Mech. 2015, 55, 289–300. https://doi.org/10.1007/s11340-014-9856-4.

12. Javadzadeh P. B. , Runnels S.R., Kazemi M.T., Ren Y., Martinez T., Peterson N., Clarke A.J., Regueiro R.A., Song B., Lu H. Characterization of IDOX/Estane Particulate Composites Using X-ray Computed Tomography and Surface Deformation Measurements under Compression. Exp. Mech. 2026. https://doi.org/10.1007/s11340-026-01317-y

Complex Flow and Modeling

THE EFFECT OF SHEARING ON BARITE SAG

Arild Saasen[1,2], Jan David Ytrehus[3] and Hanne Rokstad[3]

[1]ALKAS Atlantic AS, NO-3426 Gullaug, Norway
[2]University of Stavanger, NO-4036 Stavanger, Norway
[3]SINTEF, Trondheim, Norway

DOI: 10.31265/j2qxh126

ABSTRACT

Sag of weight material is an oil or geothermal well drilling phenomenon that is difficult to determine from industry standard measurements. To create a sag free fluid, it is necessary to create a structure in the fluid even though it is in a liquid state. Thus, the elastic responds must be larger than the energy loss responds in the fluid. This is possible in a water-based drilling fluid, but not in an oil-based fluid. Oil-based fluids is a combination of a multimodal dispersion and an emulsion. There are no real gels formed in an oil-based drilling fluid. The fluid is thickened by having Brownian motion to develop a geometrical structure of water droplets or solid particles. Adding barite to a drilling fluid will increase the density and also bring more particle with a huge surface area and thus viscosify the fluid.

Sag in water-based drilling fluids has its highest severity at 1.55 sg. However, because of the nature of polymers in water-based drilling fluids, sag is not a problem as long as the polymers are well dispersed. For higher densities the sagging barite particles float up on the material creating a counterflow helping to disperse the barite. The situation is more complex for oil-based drilling fluids. There are normally no real networks creating a real yield stress or a real gel structure. The viscosity is constructed by adding emulsified water with additives working in the oil-phase between the water droplets.

Because of the size of the barite, the oilfield viscometer size is constructed with a gap somewhat larger than 1mm to provide viscosity data relevant for frictional pressure losses in the drill pipe and in the annulus. As mentioned above barite act like a viscosifier in addition to act as a weighting agent. Thus, sag cannot be determined by the properties of the fluid m being much larger than the barite particle volumes. The interesting parts controlling the sag is likely to be due to the droplet emulsion as it forms the fluid volume relevant for the barite.

If the drilling fluid is sheared properly, both the droplet size and the interdroplet distances are reduced. The barite particle size has not been changed. But the barite particle cannot move without creating a flow making a collision between water droplets. Even though it is not measured on viscosity measurements made in accordance with standards, this increases the viscosity significantly seen from the individual barite particles. Hence, sag can be reduced by shearing.

INTRODUCTION

Barite sag is a phenomenon that is challenging, or sometimes impossible, to detect using industry standard measurements[1,2]. It has been suggested that to create a sag free fluid, the fluid must develop a structured network even when it is in a liquid state. In other words, the fluid's elastic modulus, G', should exceed the energy loss modulus, G'' also when being subject to shear. This condition can be achieved in water-based drilling fluids, but is generally not possible in oil-based fluids. Oil-based drilling fluids do not form true gels; instead, they thicken due to Brownian motion creating a geometrical structure of water droplets and solid particles. Adding barite increases the drilling fluid's density, but it also introduces a large number of particles with extensive surface area. This makes barite act as a viscosifier as well as a weighting agent. This is illustrated in **Fig. 1** which is based on data from Halvorsen et al.[3] who measured Herschel-Bulkley parameters as function of density for an oil-based drilling fluid. The Herschel-Bulkley model is used here with dimensionless shear rates, indicating that the drilling fluid's viscosity is proportional to the sum of its yield stress and excess stress at shear rates relevant to drilling operations, divided by the relevant shear rate[4] as shown in Eq. 1.

$$\tau = \tau_y + \tau_s \left(\frac{\dot{\gamma}}{\dot{\gamma}_s}\right)^n \tag{1}$$

where τ_y is the yield stress, τ_s is the additional stress or surplus stress at the typical flow shear rate, $\dot{\gamma}_s$, $\dot{\gamma}$ is the actual shear rate and n is the flow index. As illustrated in **Fig. 1**, the yield stress of the drilling fluid exhibited a gradual increase with the addition of barite. At a shear rate of 170 s^{-1}, representative of conditions encountered when drilling 8½″ sections, the corresponding shear stress increases to an even greater extent than the yield stress alone. This additional contribution, referred to as the surplus stress, becomes increasingly pronounced as barite concentration rises, whereas the flow index, or curvature index remains largely unaffected. The shear stress at 170 s^{-1} can therefore be obtained by summing the yield stress and the surplus stress, as expressed in Eq. 1[5].

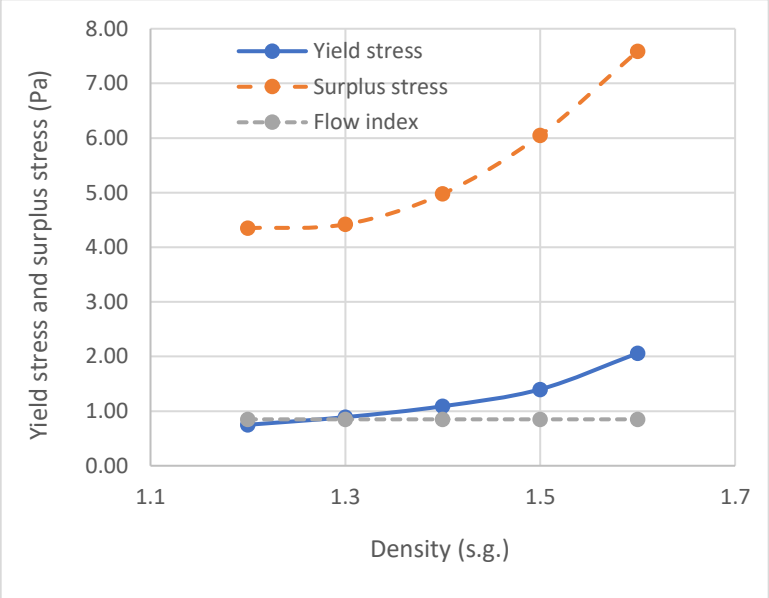

FIGURE 1: Barite as viscosifier in an oil-based drilling fluid. Data based on Halvorsen et al.[3]

The Bingham plastic model as defined in API and ISO procedures[6,7], does not provide sufficiently accurate viscosity estimates in the low shear-rate regime that is critical for evaluating barite sag[2]. In contrast, the Herschel–Bulkley model provides a reasonable approximation of drilling-fluid viscosity across a broad range of shear rates and is therefore widely applied in hydraulic pressure-loss calculations. Because the model is strictly empirical and have only limited relations to internal structures in the fluids, it cannot simultaneously reproduce accurate viscosity values for hydraulic calculations and for improving fluid stability. The low shear-rate yield point (LSYP), as defined by Zamora and Power and incorporated into API specifications[8,6], offers a practical approximation of the yield stress for use in pressure-loss predictions. The LSYP is calculated as $\tau_y = 2\tau_3 - \tau_6$, where $\tau_3$and $\tau_6$correspond to dial readings at 3 and 6 rpm on a standard rotational viscometer. Although this parameterization is adequate for hydraulic modeling, the following analysis demonstrates that LSYP-based values are insufficient for determining the rheological characteristics required to prevent barite sag.

The yield stress of a complex fluid cannot be represented by a single, well-defined value. Rønningsen[9], in his analysis of the rheology of waxy crude oils, describes the yielding process as a sequence of distinct deformation regimes: *"When subjected to a given shear stress, the rheological response is characterized by an initial, transient elastic deformation, followed by a creep flow period at very low shear rate, the length of which depends on the shear stress, then a fairly rapid collapse of the gel towards an equilibrium shear rate, characteristic for a given temperature".* This behaviour illustrates that flow initiation does not occur instantaneously. Instead, yielding begins only once the applied shear stress exceeds a critical level, and the rate at which flow develops depends both on the magnitude of the applied stress and on the microstructural characteristics of the fluid. Consequently, startup flow may proceed gradually or abruptly, depending on the fluid composition and the imposed stress conditions.

SAG IN OIL-BASED DRILLING FLUIDS

Sag in water-based drilling fluids reaches its maximum severity at a density of approximately 1.55 sg[2]. At higher fluid densities, the settling barite particles induce a counter-flow of the continuous phase, which enhances barite dispersion and mitigates further sag. In water-based systems, the presence of well-dispersed polymers generally prevents significant sagging, as these polymers establish sufficient structural integrity to stabilize the suspension.

The behaviour of oil-based drilling fluids is more complex. These systems typically lack a true three-dimensional network capable of generating a substantial yield stress effect or a robust gel structure. Instead, their viscosity arises primarily from internal placement of emulsified water droplets and the action of oil-phase additives that interact within the continuous oil medium.

Because barite particles and fluid loss additives are relatively large, oilfield viscometers are designed with a measurement gap of 1.17 mm to ensure that the recorded rheological properties reflect frictional pressure losses in both the drill pipe and the annulus. As noted previously, barite functions not only as a weighting material but also contributes to the apparent viscosity of the fluid. Consequently, sag cannot be reliably assessed using rheological measurements obtained at measurement volume scales significantly larger than the characteristic barite particle size.

A key factor influencing sag behaviour is likely the droplet emulsion, since the barite particles are suspended within the continuous oil phase that contains dispersed water droplets.

The barite therefore experiences a two-phase flow environment in which the suspended solids interact with a fluid microstructure composed of elements significantly smaller than the barite itself. For a typical oil-to-water ratio of approximately 80/20 and a reasonably uniform droplet size distribution, the mean spacing between water droplets will be on the order of the droplet diameter. This geometrical observation is independent of the absolute droplet size.

Omland[10] presented an electron microscopy image of an unsheared oil-based drilling fluid showing water droplets approaching 100 µm in diameter (**Fig. 2**), illustrating the variation in the scales of the emulsion structure that governs barite suspension behaviour.

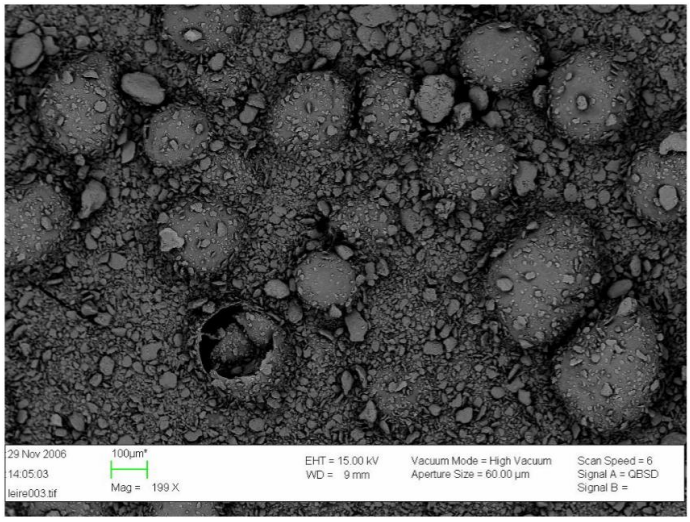

FIGURE 2: Example of a nearly un-sheared oil-based drilling fluid[10]. Courtesy of T.H. Omland

In the illustrative example shown in **Figs. 3–4**, an unsheared drilling fluid contains numerous barite particles whose D_{50} values are comparable to, or smaller than, the emulsion droplet size. Under these conditions, many barite particles encounter relatively unobstructed oil channels between the large droplets, allowing them to settle rapidly through the continuous phase (**Fig. 3**). In such a system, the only mechanism resisting sag is the viscosity of the base oil itself.

Referring to the fluid sample shown in **Fig. 2**, if the emulsion droplet size approaches 100 µm, then all barite particles in a standard API barite particle size distribution would be prone to settle. This effect is anticipated as the emulsion microstructure expectedly provides insufficient hindrance to the barite particles downward migration. It is necessary to comment that this tendency of all barite particles sagging down is modified also by other phenomena. For barite particle sizes close to 5 micron, the settling speed due to gravity becomes equal to the particle speed caused by Brownian motion. Furthermore, several oil wettable additives are introduced in the oil phase, such as organophilic clays and oil wetting surfactants, and sometimes polymeric materials. Thus, it is the larger barite particles that may be prone to sag if the internal fluid properties are not designed to sufficiently prevent this.

When the emulsion in the drilling fluid illustrated in **Fig. 3** is subjected to sufficient shear, the water droplets are reduced in size, as depicted in **Fig. 4**. This reduction decreases the inter-droplet spacing, which becomes comparable to the new, smaller droplet diameter. The barite particle size, however, remains unchanged by the shearing process. Under these conditions, the barite particles that previously settled freely through the large droplet network in **Fig. 3** can no longer move without creating frequent collisions with the dispersed water droplets. These

droplets, in turn, also interact with one another, producing localized rearrangements and occasional leapfrogging behaviour. Collectively, these interactions substantially increase the effective internal viscosity as experienced by the barite particles. Thereby, this phenomenon markedly reduce sag even though the viscosity of the bulk drilling fluid creating the frictional pressure loss for the annulus flow can remain unchanged.

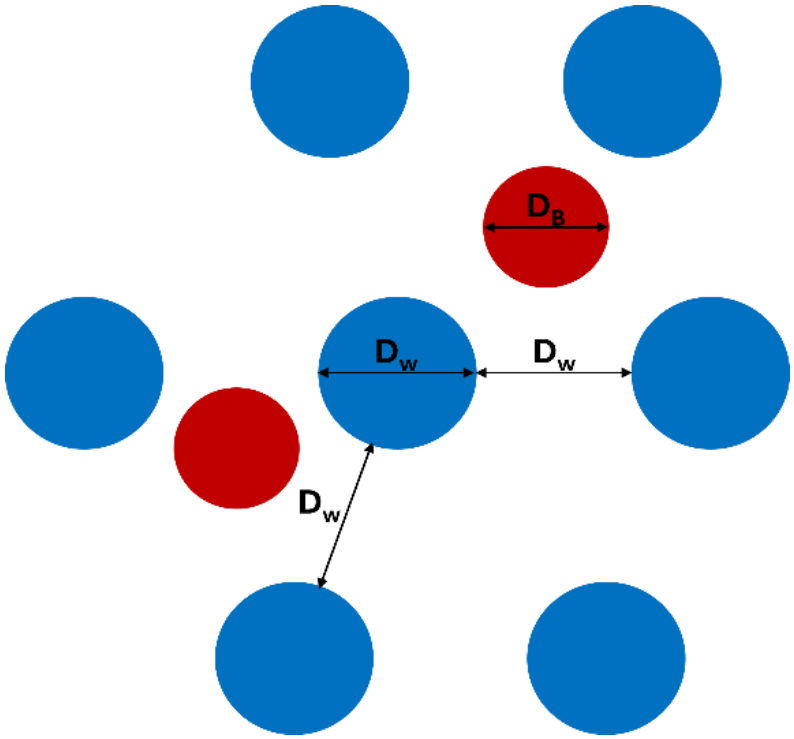

FIGURE 3: Illustration of a nearly un-sheared oil-based drilling fluid emulsion with oil-water ratio around 80/20 (blue particles are water droplets) with one similar size barite particle (red particles)

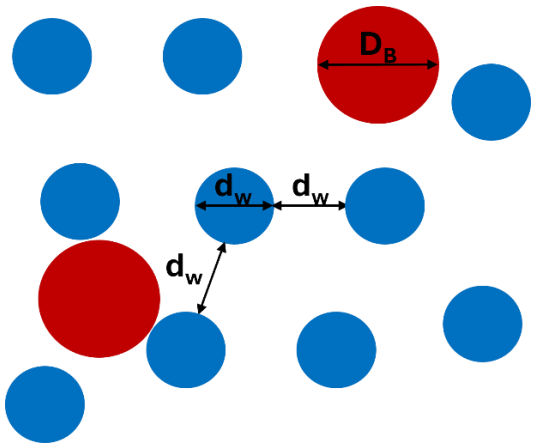

FIGURE 4: Illustration of a sheared oil-based drilling fluid emulsion with oil-water ratio around 80/20 (blue particles are water droplets) with barite particles of the same size as illustrated in **Fig. 3** (red particles).

Field experience clearly demonstrates that applying sufficient shear to a drilling fluid reduces its tendency to exhibit barite sag[10,11] for the time period where the droplet distribution

remains stable. In a shear test conducted at a drilling-fluid plant, a 25 m³ premix was subjected to intensive shearing. Although no measurable change in filtrate viscosity was detected using the standard rheological procedures provided by API, the electrical stability (ES) increased markedly. This rise in ES indicates that the emulsion droplets were broken into smaller droplets, which experience greater hydrodynamic resistance when moving through the base oil to bridge off the electrical circuit in the ES measurements. Such microstructural refinement is therefore expected to significantly diminish barite sag[11].

PROPERTIES OF OIL-BASED DRILLING FLUIDS

Most introductory fluid-mechanics texts include a brief discussion of the characteristic length scales required for continuum descriptions of fluid flow. Batchelor's *An Introduction to Fluid Dynamics*[12] is no exception. In his treatment, he presents measurements of fluid density for a simple Newtonian fluid as a function of the sample volume to which the measuring instrument responds. For a large such volume the density may vary because of natural variations of spatial distribution of density. When this volume becomes sufficiently small, a constant density is obtained representing the local value of fluid density. For even smaller volumes measured the measured density begins to fluctuate due to molecular-scale variations, illustrating the breakdown of the continuum approximation at very small length scales.

For an oil-based drilling fluid the situation becomes less predictable. Measurable variations in density, along with variations in viscosity and other properties arise at fluid volumes far larger than those at which molecular-scale fluctuations appear in simple liquids. This behaviour is illustrated in **Fig. 5**. An oil-based drilling fluid comprises a heterogeneous mixture of emulsified brine in a base oil, organophilic clays or polymers, barite, and several additional additives. The relevant characteristic length scale is on the order of ten times the diameter of the largest barite particles. When API-grade barite is used, this requirement yields a representative element volume corresponding to a spherical volume with diameter of approximately 0.70 mm, below which the fluid can no longer be assumed to exhibit uniform properties.

Figs. 5 and 6 provide an illustration of this effect. As the measurement volume is progressively reduced along the trajectory indicated by the boxes in the diagonal in **Fig. 5**, a corresponding density response illustrated in **Fig. 6** is obtained. Even so, the density variations observed here occur at volumes several orders of magnitude larger than those reported by Batchelor[12] for simple fluids, reflecting the much coarser microstructural heterogeneity inherent to oil-based drilling fluids. In addition to density, similar effects caused by the measurement volume will be found for other properties like rheological parameters.

A consequence of using the simplified representation shown in **Fig. 5**, the flow behaviour of an oil-based drilling fluid is most appropriately interpreted within the framework of multiphase or multicomponent flow. For the larger barite particles, stability depends on their interaction with a surrounding mixture composed of droplets and smaller solid components that are orders of magnitude smaller than the barite itself. When the characteristic barite size approaches that of the surrounding dispersed entities, a multicomponent flow description may be required.

In such cases as described in the previous sections, constitutive models developed for suspensions using physical framework, such as the Quemada model[13,14,15,16], may offer a more useful starting point than applying empirical models based on curve fitting viscosity data. With suitable modification or extension, a model should potentially be adapted to describe barite sag under conditions where particle–droplet and particle–particle interactions dominate the suspension rheological performance.

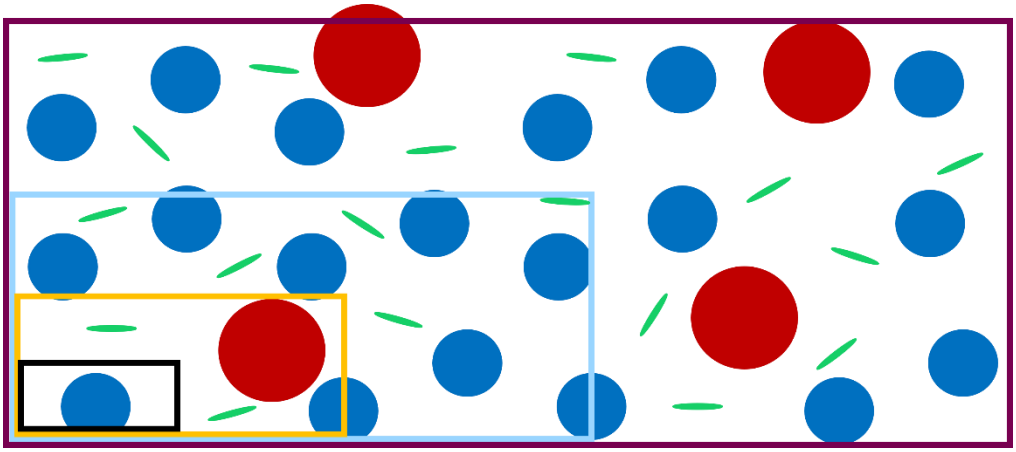

FIGURE 5: Illustration of a simplified oil-based drilling fluid composition (blue particles are water droplets) with one size barite particles (red particles) and other additives (green bars). The squares show the volumes of fluid to which the measurements belong. The volumes vary in size along the diagonal.

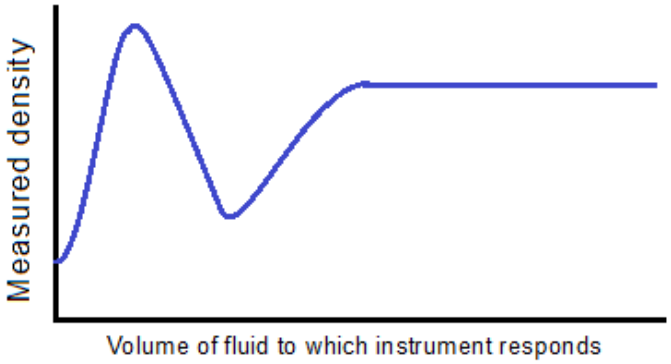

FIGURE 6: Example of an oil-based drilling fluid density as function of the measurement volume

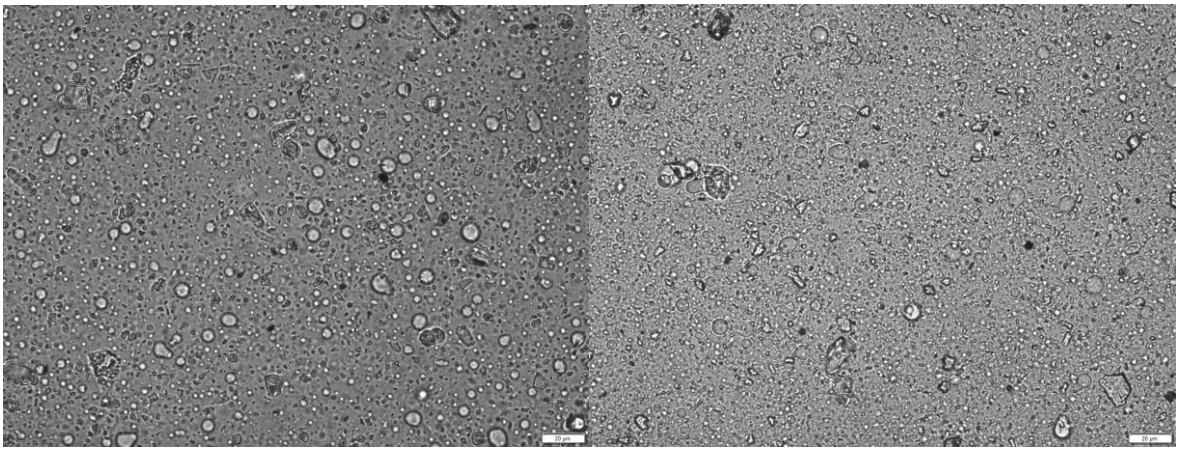

FIGURE 7: Un-sheared oil-based drilling fluid premix (no Barite) to the left and sheared premix to the right. Measurement bar length is 20 micron.

The viscometer specified by API requirements[6] is designed to generate rheological data appropriate for pressure-loss calculations. It operates using a rotating-cylinder geometry in which the sample is contained within a measurement cup, following the classical configuration

described by Whorlow[17]. To ensure valid continuum-scale measurements, the gap between the cylinders must be at least an order of magnitude larger than the largest suspended particles. For drilling and wellbore fluids, these largest particles are typically on the order of 75 μm, necessitating a gap width exceeding 1 mm.

Because of the large measurement gap in oilfield viscometers, viscosity values obtained from such instruments cannot be expected to reflect the stability of fluids whose governing flow phenomena occur at much smaller length scales within the microstructure. In common well circulated oil-based drilling fluids, emulsion droplets typically fall within the 5–10 μm range, as illustrated in **Fig. 7** for diluted samples. Consequently, API-type viscometers probe a volume far too large to capture the microstructural interactions that control barite suspension and sag behaviour.

SUMMARY

Barite sag in oil-based drilling fluids arises from interactions within a multiphase system composed of barite particles, emulsion droplets, and base oil. Because barite particles are much larger than the surrounding droplets, their stability depends on how effectively the smaller dispersed phases hinder particle settling. When droplet sizes are large or insufficiently sheared, barite can move through free oil channels and sag rapidly. Proper shearing reduces droplet size and thus spacing without destroying other typical oil-based drilling fluid components (with the exception of calcium carbonate), increasing hydrodynamic resistance and creating a more complex multiphase flow environment that significantly suppresses barite sag. These internal flow effects cannot be monitored using viscosity measurements in accordance with API requirements.

REFERENCES

1. Saasen, A., Ytrehus, J.D and Rokstad, H. Barite Sag Fundamentals - Sag in Oil-Based Drilling Fluids. Proc. ASME 45th International Conference on Ocean, Offshore and Arctic Engineering, Tokyo, Japan, June 7-12.
2. Saasen, A., Liu, D., Marken, C.D., Sterri, N., Halsey, G.W. and Isambourg, P., Prediction of Barite Sag Potential of Drilling Fluids from Rheological Measurements, In 1995 IADC/SPE Drilling Conference, Amsterdam, https://doi.org/10.2118/29410-ms.
3. Halvorsen, H., Blikra, H.J., Grelland, S.S., Saasen, A. and Khalifeh, M. Viscosity of Oil-Based Drilling Fluids, *Ann. Trans. Nordic Rheol. Soc*., **2019**, 27, 77-85.
4. Saasen, A. and Ytrehus, J.D. Rheological Properties of Drilling Fluids – Use of Dimensionless Shear Rates in Herschel-Bulkley Models and Power-Law Models, *Applied Rheology*, **2018**, 28(5), paper 54515. doi.org/10.3933/ApplRheol-28-54515
5. Saasen, A., and Ytrehus, J.D. Viscosity Models for Drilling Fluids-Herschel-Bulkley Parameters and Their Use, *Energies*, **2020**, 13(20), 5271. https://doi.org/10.3390/en13205271.
6. American Petroleum Institute, *Recommended Practice for Testing Oil-Based Drilling Fluids*, API Recommended Practice 13B2; **2014**, API: Washington, DC, USA.
7. International Organization for Standardization, *Petroleum and Natural Gas Industries. Field Testing of Drilling Fluids. Part 1: Water-Based Fluids*, Report ISO 10414-1; **2008**, ISO: Geneva, Switzerland.
8. Power, D. and Zamora, M. Drilling Fluid Yield Stress: Measurement Techniques for Improved Understanding of Critical Drilling Fluid Parameters. American Association Drilling Engineers 2003 National Technology Conference, **2003**, Houston.
9. Rønningsen, H.P. Rheology of Petroleum Fluids. *Ann. Trans. Nordic Rheology Soc.*, **2012**, 20, 11-18
10. Omland, T.H. *Particle Settling in non-Newtonian Drilling Fluids*, PhD Thesis no 80, **2009**, University of Stavanger, Norway

11. Ånesbug, G.O., Lembourn, P., Amiri, M.M., Fimreite, G., Askø, A., Ytrehus, J.D. and Saasen, A. Field Application and Drilling Fluid Plant Tests of Dual Jet Shear Gun for Drilling Fluid Stability Maintenance. Proc. ASME 45th International Conference on Ocean, Offshore and Arctic Engineering, Tokyo, Japan, June 7-12.
12. Batchelor, G.K. *An Introduction to Fluid Dynamics*, Cambridge University Press, 1967, Cambridge, UK.
13. Quemada, D. Rheological modelling of complex fluids. I. The concept of effective volume fraction revisited. *European. Physics. J., AP.* **1998**, 1(1), 119–127. dx.doi.org/10.1051/epjap:1998125
14. Baldino, S., Osgouei, R.E., Ozbayoglu, E., Miska, S., May, R. Quemada model approach to oil or synthetic oil based drilling fluids rheological modelling. *J. Pet. Sci. Eng*. **2018**, 163, http://dx.doi.org/10.1016/j.petrol.2017.12.042.
15. Knutsen, S., Cayeux, E., Saasen, A., Khalifeh, M. Application of the Quemada viscosity model for drilling fluids. Int. Conf. on Offshore Mechanics and Arctic Engineering. In: Petroleum Technology, 10, V010T1123, **2021**. http://dx.doi.org/10.1115/OMAE2021-60500.
16. Bjørkevoll, K.S. Using the Quemada rheology model for drilling fluids — Practical considerations. *Geoenergy Sci. and Engn.*, **2024**, 240, 213051. https://doi.org/10.1016/j.geoen.2024.213051
17. Whorlow, R.W. *Rheological Techniques*, Ellis Horwood Ltd. **1980**, Chichester, UK.

MEASUREMENT METHOD FOR DENSITY OF DRILLING FLUIDS AT HIGH PRESSURE AND TEMPERATURE

Tinku Saikia[1], Blandine Feneuil[1], Elie N'gouamba[1], Jan Ole Skogestad[2] and Harald Linga[2]

[1]SINTEF Industry, Applied Geosciences, Trondheim, Norway
[2]SINTEF Industry, Applied Geosciences, Bergen, Norway

DOI: 10.31265/gm0ykm74

ABSTRACT

Large-scale deployment of CO_2 storage will require the drilling of numerous new wells, introducing additional operational challenges. One key concern is the potential influx of CO_2 into the wellbore during drilling operations, which can significantly alter the thermophysical properties of drilling fluids, including density and viscosity. A reduction in drilling fluid density or hydrostatic pressure may compromise well control and, in severe cases, lead to blowout incidents. It is therefore essential to quantify the impact of CO_2 dissolution on drilling fluid properties under representative downhole conditions, with pressures up to 400 bar and temperatures up to 100 °C.

Conventional densitometers are not suitable for these measurements due to the presence of solid particles in drilling fluids. To address this limitation, a dedicated experimental method was tested based on monitoring the volume changes of the fluid under controlled pressure, temperature, and CO_2 loading conditions. This paper first presents a detailed description of the experimental methodology. Subsequently, representative results are provided for drilling fluid density measurements, highlighting the influence from dissolved CO_2, pressure and temperature on fluid density behavior.

INTRODUCTION

Drilling fluids, commonly known as drilling muds, are essential to oil and gas well construction. Although they may appear to be simple circulating fluids, they are carefully engineered systems designed to perform several critical functions simultaneously. As drilling progresses, the drill bit generates significant heat and friction; drilling fluids cool and lubricate the bit, improving drilling efficiency and extending equipment life. They also transport drilled cuttings from the bottom of the wellbore to the surface, preventing accumulation that could cause blockages or stuck pipe. In addition, drilling fluids help maintain wellbore stability by forming a thin filter cake on the borehole wall, reducing fluid invasion and minimizing the risk of formation collapse. They also transmit hydraulic energy to downhole tools and suspend weighting materials and solids when circulation stops[1].

Among all drilling-fluid properties, density is arguably the most important because it directly controls the hydrostatic pressure exerted by the fluid column[2]. Maintaining the correct pressure balance is essential throughout drilling operations. If the fluid density is too low,

formation fluids such as oil or gas may enter the wellbore, leading to kicks and potentially blowouts[3]. Conversely, excessive density can fracture the formation, causing lost circulation and increasing operational costs. Achieving and maintaining the optimal density therefore requires continuous monitoring and adjustment.

The importance of density becomes even greater in complex drilling environments where gases such as CO_2 dissolve into the fluid or where multiple phases, including oil, water, and solids, coexist[4]. Under these conditions, density is not constant but varies with pressure, temperature, and composition. Even small changes can significantly affect well control. Consequently, accurate characterization of drilling-fluid density under realistic downhole conditions is essential for safe and efficient drilling operations.

Several techniques are available for density measurement. Simple methods include hydrometers, which determine density through buoyancy, and pycnometers, which calculate density from precise mass and volume measurements[5]. While both methods can provide reliable results, they are generally limited to laboratory conditions at ambient pressure and temperature. More advanced techniques include vibrating U-tube densitometers, oscillating piston densitometers, and optical methods such as refractometers and ultrasonic density meters. These instruments offer high precision for many fluids but are often best suited for particle-free, homogeneous systems[6].

For high-pressure and high-temperature applications, specialized instruments are required. Common options include high-pressure vibrating-tube densitometers, sinker-based densimeters, and pressure–volume–temperature (PVT) cells. However, when measuring drilling-fluid density in the presence of dissolved CO_2 over a wide pressure range (approximately 30–400 bar) and temperatures up to 100 °C, many conventional methods become inadequate.

Hydrometers and pycnometers cannot operate under controlled high-pressure conditions, while optical techniques are affected by suspended solids, emulsions, and CO_2 bubbles that interfere with light transmission or sound propagation. Vibrating U-tube densitometers, although highly accurate for single-phase fluids, face challenges with drilling muds containing barite, clays, cuttings, and dissolved gas. Solid particles can alter oscillation behavior, while CO_2 may come out of solution during pressure changes, forming bubbles that disrupt measurements. Tube fouling and erosion further reduce long-term reliability[7].

Similar limitations affect oscillating piston and sinker-based systems. Suspended solids can cause wear or sticking in piston mechanisms, while buoyancy-based measurements assume a uniform fluid phase that may not exist when CO_2 induces phase separation, foaming, or gas release. Temperature variations also influence fluid rheology and compressibility, further complicating accurate density determination[8].

Among the available techniques, the PVT cell offers significant advantages for complex drilling-fluid systems. Unlike oscillation- or buoyancy-based instruments, it determines density from direct measurements of fluid volume under controlled pressure and temperature conditions. This approach is less sensitive to solids, gas bubbles, and multiphase behavior, making it particularly suitable for CO_2-laden drilling fluids. Furthermore, PVT cells provide excellent control of thermodynamic conditions and can accommodate heterogeneous fluids while capturing the effects of gas dissolution, phase changes, and compressibility[9].

In this study, a high-pressure PVT cylindrical piston cell was used to investigate the influence of CO_2 on drilling-fluid density over pressures ranging from approximately 30 to 400 bar and temperatures from ambient conditions to 100 °C. The results provide valuable insight into density variations under realistic downhole conditions and demonstrate the suitability of the PVT-cell method for density measurements in CO_2-invaded drilling fluids. This validation is important because conventional density-measurement techniques are generally unable to

capture the combined effects of CO_2 dissolution, multiphase behavior, and suspended solids under high-pressure, high-temperature conditions.

METHOD

The experimental methodology for evaluating the density variation of drilling fluids under varying pressure, temperature, and CO_2 concentration is based on a high-pressure piston–cylinder (PVT) system designed to replicate downhole conditions. The cylindrical piston cell made up of titanium was used to perform experiments at high pressure and high temperature conditions. The core component of the setup is a 1 L piston-operated mixing cylinder connected to a hydraulic pump, which enables precise control of pressure and volume through piston displacement. The system is capable of operating up to approximately 400 bar and temperatures up to 100 °C, thereby covering the relevant thermodynamic range for drilling applications[10].

Initially, the base drilling fluid (oil-based or water-based) is introduced into the mixing cylinder at ambient conditions. Carbon dioxide, and in some cases methane, is then injected into the system using a secondary piston-cylinder gas transfer method. In this approach, the gas is first loaded into a separate gas cylinder at controlled pressure and volume and subsequently transferred into the mixing cylinder. This procedure allows accurate determination of the mass of injected gas and therefore the precise control of CO_2 concentration, expressed as the mass fraction of the total fluid–gas mixture[11].

Following gas injection, the system is pressurized and the mixture is homogenized to achieve thermodynamic equilibrium. Homogenization is enhanced by placing a rolling steel ball inside the cylinder and mounting the system on an oscillating platform or rocker. The mixture is typically agitated for extended periods (e.g., overnight) at high pressure to ensure complete dissolution of CO_2 into the drilling fluid and to avoid phase segregation.

To ensure that density measurements are conducted under single-phase conditions (i.e., with fully dissolved gas), the bubble point of the mixture is determined using a pressure–volume (P–V) expansion method. In this procedure, the piston is gradually withdrawn at a constant rate, resulting in controlled expansion of the fluid while continuously recording pressure. A distinct change in the slope of the P–V curve indicates the onset of phase separation, and the corresponding pressure is identified as the bubble point. All subsequent density measurements are performed at pressures above this threshold to prevent the formation of free gas and maintain a homogeneous fluid phase.

The density of the drilling fluid–CO_2 mixture is determined indirectly from the volume changes measured via piston displacement. Since the total mass of the system is known from the initial fluid loading and controlled gas addition, the density is calculated based on the measured volume of the mixture. The volume is inferred from the displacement of the hydraulic fluid in the piston system, with corrected for the compressibility of the hydraulic fluid and the mechanical deformation of the cylinder. By gradually adjusting the piston position, the relationship between pressure and volume is obtained, allowing evaluation of density as a function of pressure.

The measurement procedure typically begins with establishing a reference condition by determining the density of the base drilling fluid without dissolved gas over the pressure range of interest. Subsequently, CO_2 is introduced, and the density of the gas-loaded fluid is measured under identical pressure conditions while maintaining pressure above the bubble point. Temperature effects are incorporated by heating the mixing cylinder using an external heating jacket to specified values (e.g., 50 °C or 100 °C) and repeating the pressure–volume

measurements at each temperature. This approach allows systematic evaluation of density variation with respect to pressure, temperature, and CO_2-concentration within a single experimental framework[12].

Due to potential uncertainties in absolute volume determination, such as the presence of microscopic air bubbles in the hydraulic fluid, the method is particularly suited for determining relative density changes rather than absolute density values. Therefore, the results are often reported as density variations with respect to a reference state, typically defined as the density of the gas-free drilling fluid at ambient conditions. This approach improves measurement reliability while still capturing the impact of CO_2 dissolution and thermodynamic conditions on fluid density.

Overall, the piston–cylinder PVT method provides a robust and controlled approach for investigating the thermophysical behavior of drilling fluids exposed to CO_2. By integrating precise control of pressure, temperature, and gas concentration with continuous monitoring of volume changes, the method enables detailed characterization of density variation under realistic downhole conditions, thereby supporting both experimental analysis and the development of predictive models for well-control applications.

RESULTS AND DISCUSSION

Evaluation of the cylinder volume

The density evaluation first requires a careful evaluation of the cylinder volume in the whole range of studied pressure and temperature. The assessment of the cylinder volume was carried out in three steps:

1- Evaluation of a reference volume, at room temperature and one pressure (50 bar)
2- Evaluation of volume change under pressure variations.
3- Evaluation of the volume change under temperature variations.

For the first step, the volume of the cylinder at 50 bar was evaluated by displacing the inner piston from one end of the cylinder to the other at constant pressure, we found that the volume at 50 bar and 23°C was 1010 mL.

Secondly, a test was performed with water only to evaluate the dilatation of the cylinder at room temperature. The pressure increased from atmospheric pressure to 400 bar, then decreased from 400 bar to atmospheric pressure. The data in **FIGURE 1** shows the volume change of the cylinder during pressure ramp (b), calculated from the amount of water received by the pump (a).

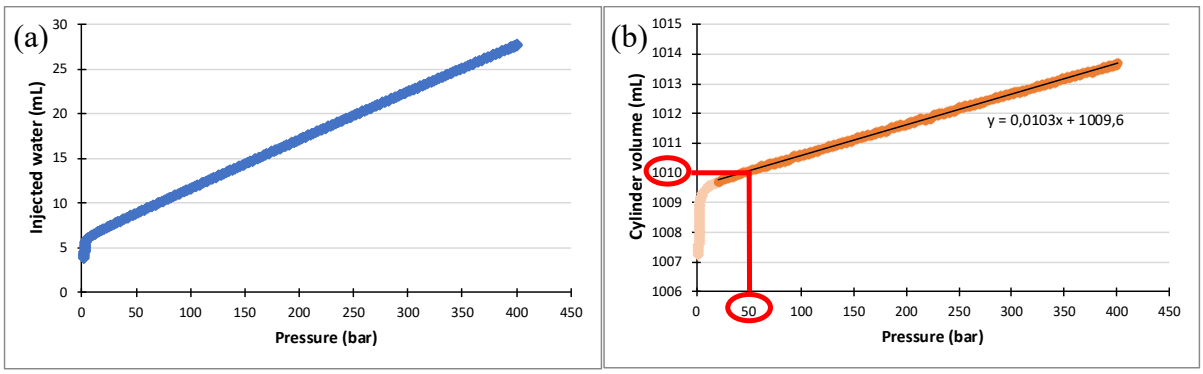

FIGURE 1: (a) Cumulative water volume injected by the pump during pressure increase at 23°C. (b) Deduced cylinder volume at room temperature, deduced from graph (a) and taking into account water

compressibility. The orange curve shows the experimental data, while the black line shows the linear regression in the range 20 - 400 bar.

We first note that the injected water – pressure relation is linear in the range 30 – 400 bar. However, at lower pressure, the curve does not follow this linear trend. We believe that this is due to the presence of a small amount of air bubbles in the water, which dissolve when the pressure reaches 30 bar. This indicates that the density method presented in this paper should be limited to for pressures above about 30 bar. The cylinder volume is calculated from the injected water volume, taking into account the compressibility of water. The volume at 50 bar is adjusted to the reference value 1010 mL. We see that when the pressure is about 30 bar, the pressure sensitivity for the cylinder volume at 23°C is given by the linear relation:

$$\mathrm{V\ [in\ mL]} = 0{,}0103\ \mathrm{P\ [in\ bar]} + 1009{,}6 \qquad (1)$$

To take into account the effect of temperature on the volume, Eq. 1 is corrected using the volumetric thermal dilatation coefficient of titanium: $\alpha = 3 \cdot 10^{-5}\ K^{-1}$, giving:

$$\mathrm{V\ [in\ mL]} = (0{,}0103\ \mathrm{P\ [in\ bar]} + 1009{,}6) \cdot (1 + \alpha(T\ [in\ °C] - 23)) \qquad (2)$$

Eq. 2 shows that the cylinder volume increases by about 4 mL when the pressure is increased from 50 to 400 bar, while an increase of the temperature from 23°C to 100°C leads to a volume increase of 2 mL

Validation of the method

Some tests have been performed using a base oil to check that the effect of density variation with pressure are well captured with the cylinder method. The density measured with the cylinder is compared with densitometer measurements in **FIGURE 2**.

As mentioned before, the cylinder tests do not provide an absolute density evaluation, therefore the initial oil volume has been manually adjusted to ensure that the density at 50 bar measured by both method match. **FIGURE 2** shows that the slope of the pressure-density curve is the same for both methods. The density at 1 bar obtained from the cylinder method is 5 kg/m^3 lower than the density read from the densitometer; this is as explained before due to a small amount of bubbles in the liquid in the cylinder.

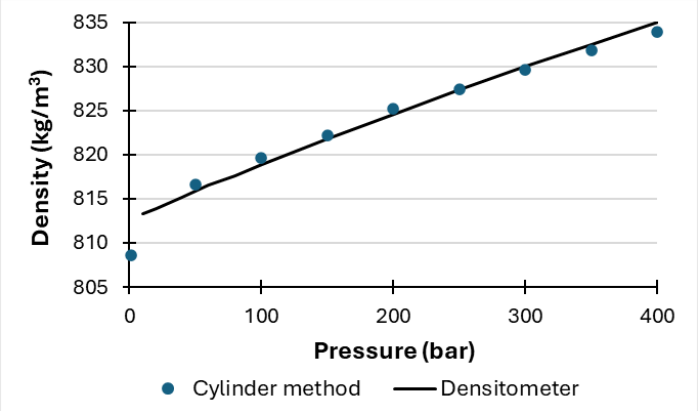

FIGURE 2: Comparison of density measured by the cylinder method and by an Anton Paar densitometer

Results on an oil-based drilling fluid with dissolved CO2

A drilling fluid – CO2 mixture has been prepared following the method described by Skogestad et al. (2024)[12]. Here, we present the results of the density measurements obtained with the cylinder method. In these experiments, we measured consecutively the density for the following conditions (pressure was not decreased below 30 bar after the experiment was started):

1- Fluid without CO_2 at 23°C
2- Fluid without CO_2 at 50°C
3- Fluid without CO_2 at 100°C
4- Fluid with CO_2, 4% of the total weight, at 23°C
5- Fluid with CO_2, 4% of the total weight, at 50°C
6- Fluid with CO_2, 4% of the total weight, at 100°C
7- Fluid with CO_2, 4% of the total weight, at 23°C

Steps 4 and 7 are similar conditions and allow us to check the repeatability of the test. The measured pressure-density curves are shown in **FIGURE 3**. We observe that the density of the drilling fluid decreases when the temperature increases and decreases when CO_2 is dissolved.This is in agreement with previous observations[10,11].

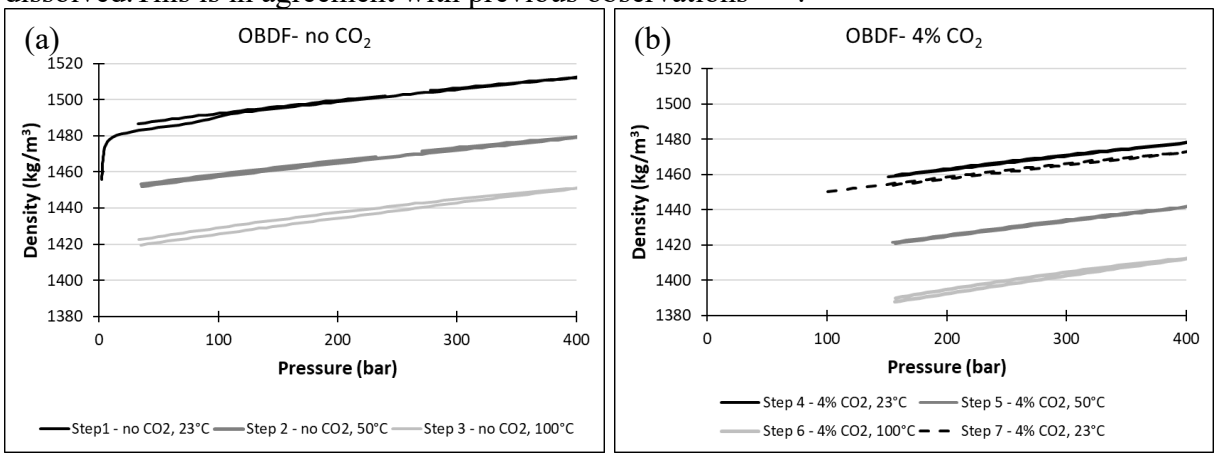

FIGURE 3: Density measurement on oil-based drilling fluid at three different temperatures, (a) without dissolved CO_2 and (b) with 4% CO_2 weight fraction.

Skogestad et al. (2024)[12] have shown that the density of an oil-based drilling fluid after dissolution of 8% CO_2 by weight could be correlated with the density of base-oil – CO_2 mixture, under the assumption that the CO_2 dissolves only in the base oil (and not in the brine droplet or solid phases). Similarly, we can compare the experimental density values from **FIGURE 3** with the theoretical density, calculated from the density of the components. The assumptions for this calculation are as follows:

- The initial fluid is composed of three phases: base oil (56.6%, 835 kg/m^3), brine (24.3%, 1200 kg/m^3) and solids (19.1%, 3900 kg/m^3). The solid fractions have been provided by the manufacturer, the base oil density has been measured, the other densities at 400 bar have been estimated so that the density of the OBDF at 23°C and 400 bar is about 1510 kg/m^3.
- The volumetric thermal dilatation coefficient of brine is 4.10^{-4} K^{-1} [13]; the density of the brine droplets is therefore 1187 kg/m^3 at 50°C and 1164 kg/m^3 at 100°C. No CO_2 dissolves in brine.
- The volumetric thermal dilatation coefficient of solids is 4.10^{-5} K^{-1} [14]; the density of the solids is therefore 3896 kg/m^3 at 50°C and 3888 kg/m^3 at 100°C.

- The density of the base oil is affected by the temperature and the CO_2 loading, as shown in **FIGURE 4** (a). Assuming that the CO_2 dissolves only in the base oil, 4% of CO_2 by weight of OBDF corresponds to 12% of CO_2 by weight of base oil. The densities of the base-oil with dissolved CO_2 are therefore 852 kg/m^3 at 23°C, 833 kg/m^3 at 50°C and 797 kg/m^3 at 100°C.

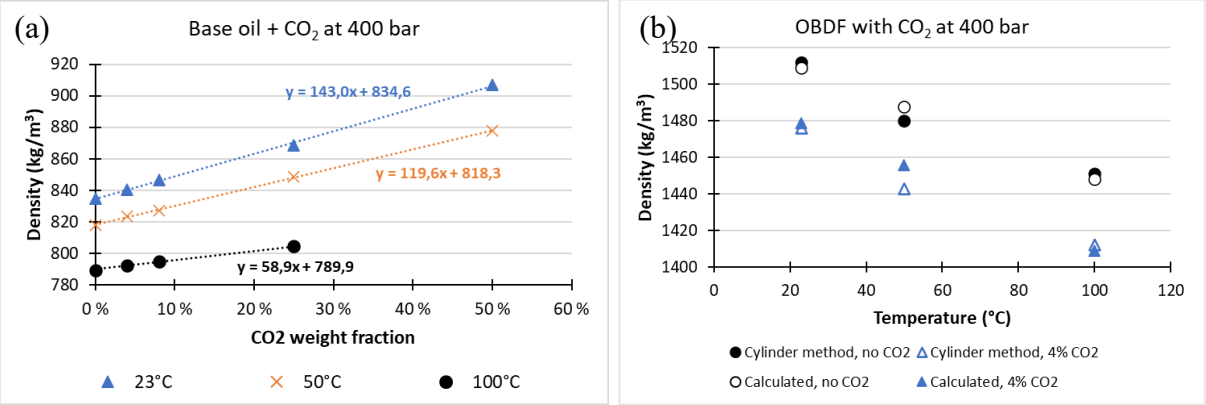

FIGURE 4: (a) Density measured with the densitometer for base-oil CO_2 mixtures, at 400 bar. Data from Skogestad et al. (2024)[12]. (b) Density of OBDF – CO2 mixtures at 400 bar. The filled symbols represents measurements with the cylinder method and are taken from **FIGURE 3**. The empty circles and triangles are calculated values.

FIGURE 4 (b) shows that under these assumptions, the calculated values are similar to the values measured by the cylinder method. It confirms that the cylinder method serves to accurately measure the variation of the drilling fluid density as a function of temperature, pressure, and dissolved gas content.

CONCLUSION

We have presented in this paper a method to evaluate how the density of a fluid is affected by pressure, temperature and gas content. We show that for a simple fluid (base oil), this method gives similar results as a densitometer. The advantage of this method is that it is effective to study complex industrial fluids such as drilling fluids, as it does not have any limitations regarding volume content and size of particles.

ACKNOWLEDGEMENTS

The authors gratefully acknowledge the financial support provided by Gassnova, Equinor, Shell, EBN, CNOOC, and eDrilling through the CLIMIT-Demo project 622128, "Well Control for CO_2 Wells". Additional support was provided by Gassnova, Equinor, BP, and eDrilling through the CLIMIT-Demo project "CO_2 Hydrate Risk Prediction". The authors also thank Baker Hughes for supplying the fluids used in the experiments.

BIBLIOGRAPHY

(1) Saikia, T.; Mahto, V. Experimental Investigations and Optimizations of Rheological Behavior of Drilling Fluids Using RSM and CCD for Gas Hydrate-Bearing Formation. *Arabian Journal for Science and Engineering 2018 43:11* **2018**, *43* (11), 6541–6554. https://doi.org/10.1007/S13369-018-3292-1.

(2) Alizadeh, S. M.; Alruyemi, I.; Daneshfar, R.; Mohammadi-Khanaposhtani, M.; Naseri, M. An Insight into the Estimation of Drilling Fluid Density at HPHT Condition Using PSO-, ICA-, and GA-LSSVM Strategies. *Scientific Reports 2021 11:1* **2021**, *11* (1), 7033-. https://doi.org/10.1038/s41598-021-86264-5.

(3) Mirderikvand, H.; Razavian, F.; Nakhaee, A.; Moradi Ghiasabadi, B.; Gholamnia, R. A Barrier Risk-Based Evaluation Model for Drilling Blowouts. *J. Loss Prev. Process Ind.* **2022**, *74*, 104624. https://doi.org/10.1016/J.JLP.2021.104624.

(4) Ren, Y.; Yang, S.; Li, L.; Bai, Y.; Luo, P. CO2 Impact on Water-Based Drilling Fluids: Excessive Thickening Characteristics and Mechanisms. *Petroleum* **2026**. https://doi.org/10.1016/J.PETLM.2026.03.003.

(5) Zhou, Z.; Ren, T.; Li, M.; He, M.; Zhou, X. Study on Temperature Measurement of Petroleum Product Density Analyzer Based on Hydrometer Method. *J. Phys. Conf. Ser.* **2023**, *2428* (1), 012001. https://doi.org/10.1088/1742-6596/2428/1/012001.

(6) Ombe, E. M.; Elyas, O. A.; Qader, T. A.; Mehdi, M. Application of a Real Time Mud Density and Rheology Monitoring System to Enhance Drilling in High Pressure High Temperature Gas Wells with MPD Systems. *International Petroleum Technology Conference 2020, IPTC 2020* **2020**. https://doi.org/10.2523/IPTC-19909-ABSTRACT.

(7) Blencoe, J. G.; Drummond, S. E.; Seitz, J. C.; Nesbitt, B. E. A Vibrating-Tube Densimeter for Fluids at High Pressures and Temperatures. *Int. J. Thermophys.* **1996**, *17* (1), 179–190. https://doi.org/10.1007/BF01448220.

(8) Dabiri, M. S.; Haji-Hashemi, R.; Ashoorian, S.; Schaffie, M.; Zabihi, R.; Hemmati-Sarapardeh, A. Modeling Drilling Fluid Density at High-Pressure High-Temperature Conditions Using Advanced Machine-Learning Techniques. *Geoenergy Science and Engineering* **2025**, *244*, 213369. https://doi.org/10.1016/J.GEOEN.2024.213369.

(9) Demirdal, B.; Cunha, J. C. Olefin-Based Synthetic-Drilling-Fluids Volumetric Behavior Under Downhole Conditions. *SPE Drilling & Completion* **2009**, *24* (02), 239–248. https://doi.org/10.2118/108159-PA.

(10) Feneuil, B.; N'Gouamba, E.; Skogestad, J. O.; Linga, H. Effect of Dissolution of CO2 and CH4 on the Flow Curve of Drilling Fluids. *Annual Transactions of the Nordic Rheology Society* **2025**, *33*, 79–88. https://doi.org/10.31265/ATNRS.867.

(11) Skogestad, J. O.; Lund, B.; Feneuil, B.; N'Gouamba, E.; Aasen, A.; Linga, H.; Vold, L.; Bruton, Z.; Helgeland, S.; Ødegård, S. I. CO2 Well Control Scenario Prediction Using Experimentally Verified Models. *SPE - International Association of Drilling Contractors Drilling Conference Proceedings* **2025**, *2025-March*. https://doi.org/10.2118/223812-MS.

(12) Skogestad, J. O.; Feneuil, B.; N'Gouamba, E.; Linga, H.; Aasen, A.; Skår, G.; Roggeband, S. M.; Nedrum, J.; Helgeland, S. CCS Well Control Impact of CO2 on Drilling Fluid Performance. *SPE - International Association of Drilling Contractors Drilling Conference Proceedings* **2024**, *2024-March*. https://doi.org/10.2118/217711-MS.

(13) Shao, H.; Hesser, J.; Wang, W.; Kolditz, O. Modeling Thermally Driven Migration of Brine in Bedded Salt. *Geomechanics for Energy and the Environment* **2024**, *38*, 100542. https://doi.org/10.1016/J.GETE.2024.100542.

(14) Ye, Z.; Li, B.; Chen, W.; Tang, R.; Huang, S.; Xu, J.; Fan, D.; Zhou, W.; Ma, M.; Xie, H. Phase Transition and Thermoelastic Behavior of Barite-Group Minerals at High-Pressure and High-Temperature Conditions. *Physics and Chemistry of Minerals 2019 46:6* **2019**, *46* (6), 607–621. https://doi.org/10.1007/S00269-019-01026-0.

Biological Systems

IN SITU RHEOLOGY OF THE BIOFILM FROM A NITRYFYING BIOREACTOR RELEVANT FOR RAS – A PROOF OF PRINCIPLE STUDY

Sharada Navada[1], Amalie J. H. Mathisen[1] and Catherine T. Nordgård[1]

[1]Department of Biotechnology and Food Science, Norwegian University of Science and Technology (NTNU), N-7491, Trondheim, Norway

DOI: 10.31265/19hjr005

ABSTRACT

Nitrifying bioreactors are a vital component of recirculating aquaculture systems (RAS) to maintain the required water quality. Bioreactors contain suspended plastic carriers on which nitrifying microorganisms grow. Understanding the rheology of biofilms that form on these carriers can provide useful information that can be correlated with other analyses to monitor the development and stability of the microbial communities, both over the lifetime of the bioreactor and in response to environmental changes, such as the salinity changes typical of salmonid aquaculture. The standard carriers have an open patterned geometry for biofilm formation and good fluid flow through but is not convenient for *in situ* rheological measurements. In this study, we included carriers in the same material (HDPE) and with the same external dimensions but with a 20mm diameter flat surface area suitable for placement within the rheometer. The carriers were placed in stainless steel "tea-ball" cages in two lab-scale bioreactors with different configurations for five weeks and then retrieved. After securing the carrier within the rheometer (Kinexus Ultra+ with a 20mm roughened parallel plate upper geometry) the upper plate was lowered to a normal force of 0.05N. Oscillatory measurements (frequency sweep and amplitude sweep) and creep compliance measurements confirmed the biofilm on the carrier surface as a solid dominant viscoelastic solid at low strain. This is comparable with the reported behaviour of microbial biofilms.

INTRODUCTION

A biofilm is a complex community of micro-organisms, such as bacteria and fungi, embedded in an extracellular matrix composed of self-excreted polymeric substances, which provides adhesion to a growing surface, cohesion to the community, and a barrier against external agents as well as protection from shear forces and mechanical disruption[1, 2]. Biofilms may be problematic if they grow in medical or hygiene settings and provide pathogenic bacteria with protection against antibiotics and disinfectants, but in other circumstances, such as in recirculating aquaculture systems (RAS) bioreactors, they can be beneficial, and provide stability for a microbial community that performs an industrial function[3]. The secreted extracellular polymeric substances (EPS) of the biofilm may variably include polysaccharides, protein, lipids and DNA. As with other cellular systems imbedded in extracellular matrices, the rheology of both the EPS itself and the total biofilm is important for functionality.

In RAS, nitrifying microorganisms are grown in a biofilm on solid phase carriers within a bioreactor. The biofilm microbial community is essential for removing the ammonia produced by the fish from the recirculating water through the process of nitrification. These are not static systems, and the microbial communities are dynamic, developing over time and responding to resource competition and changes in environmental conditions. For salmonid aquaculture, the transition from freshwater to saltwater conditions represents a significant environmental change which can influence the performance of the bioreactor and where the EPS matrix may play a role in the robustness of the microbial community [4].
It is well established that biofilm rheology can be influenced by the mechanical perturbations involved in removal from the growth surface[5-7] so it is desirable to measure rheology *in situ*. The standard biofilm carriers used in bioreactors have an open patterned geometry for biofilm formation and good fluid flow through that is not convenient for *in situ* rheological measurements. In this proof of principle study, we included within the bioreactor carriers in the same material (HDPE) and with the same external dimensions but with a 20mm diameter flat surface area suitable for *in situ* rheological characterisation of the biofilm.

MATERIALS AND METHODS

Carriers were produced at the Mechanical Workshop of the Faculty of Natural Sciences, NTNU, in HDPE in cylindrical form with external dimensions 5mm height, 25mm diameter as shown in **Fig. 1** to match the standard carriers.

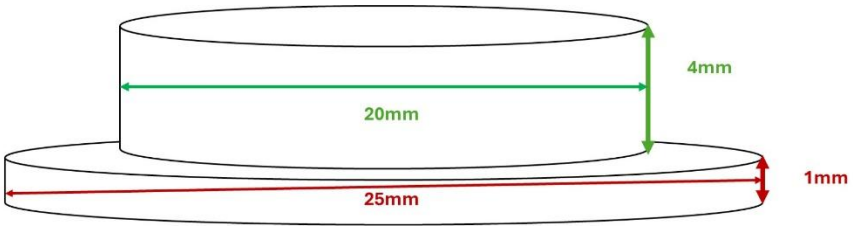

FIGURE 1. design of the rheometer compatible bioreactor carrier

Carriers were submerged for five weeks in either a lab-scale activated sludge bioreactor or a moving bed biofilm reactor (MBBR). The bioreactors were operated under environmental conditions that selected for nitrifying microbes, including continuous aeration and addition of required substrates. To prevent interference from other carriers and ensure consistent orientation, the carriers were enclosed in a metal mesh to protect the surface that would be used for rheology, (the smaller disc as seen in **Fig. 1**). Both bioreactors were operated under continuous flow with a hydraulic retention time (HRT) set to 25-26h, a pH range of 7-8, and room temperature. The media fed to the reactors were synthetic wastewater composed of ammonium sulphate ($(NH_4)_2SO_4$, 0.2 g/L), potassium dihydrogen phosphate (KH_2PO_4, 0.3 g/L), sodium carbonate (Na_2CO_3, 1 g/L), and 10 mL/L trace metal solution. pH of the media was adjusted to 7.5. During the experimental period, the system was challenged by decreasing HRT and/or increasing the ammonium concentration in the media. Spectrophotometric analyses showed that both reactors had a full conversion of ammonium to nitrate, indicating that the nitrification process was established. The carriers were stored in the fridge for 2 days before rheology measurements.

Rheology measurements were carried out using a Kinexus Ultra + rheometer (Netzsch), fitted with a 20mm diameter roughened parallel plate upper geometry at room temperature. The lower surface of the biofilm covered carrier was cleaned with 70% ethanol and the carrier was secured to the lower plate of the rheometer, and the upper plate was lowered to a normal force of 0.05N before commencing measurements. The following rheological tests were performed in the order given:
Frequency sweep 10-0.1Hz, logarithmic sampling (10 points per decade) with a target strain of 0.1%. Creep compliance repeated cycle 3x (20 Pa stress for 30s, with 2 minutes recovery time) followed by 3x (50 Pa stress for 30s, with 2 minutes recovery time). Amplitude sweep 0.1-100% strain logarithmic sampling (10 points per decade) at a frequency of 1 and 0.1Hz.

RESULTS

Oscillatory measurements showed the biofilm behaved as a viscoelastic solid dominant material at low strains, transitioning to flow dominant behaviour at higher strains (see **fig. 2 A & B**). Within the linear viscoelastic region, the absolute moduli were frequency dependent with a trend towards slightly higher phase angle at lower frequency (see **fig.2 C**). As the amplitude sweep is a potentially destructive test (if the material is not rheologically reversible) these were carried out last on the test biofilm matrix, after both the frequency sweep and the creep compliance measurements. However, the second amplitude sweep at lower frequency carried out after a rest period of 10 minutes shows a recovery of viscoelastic properties with broadly comparable moduli values to the frequency sweep.

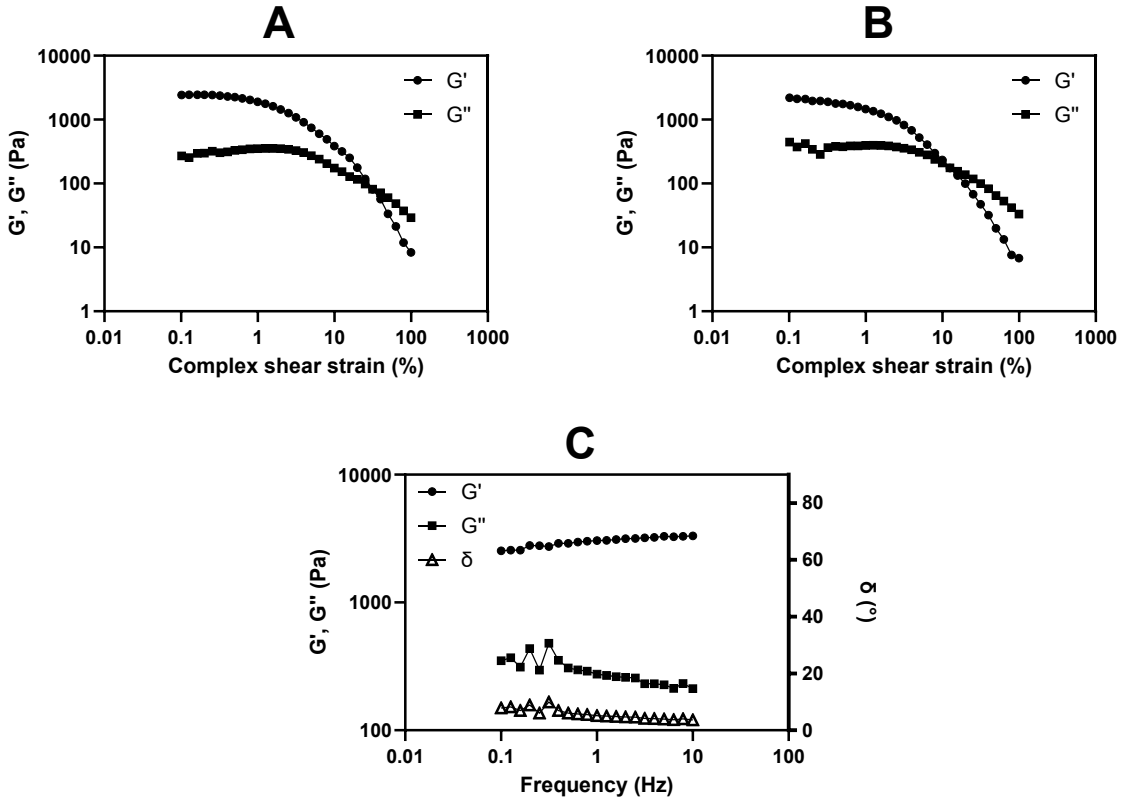

FIGURE 2. oscillatory rheology of the biofilm *in situ* on the bioreactor carrier showing an amplitude sweep at 1Hz (A), an amplitude sweep at 0.1Hz (B), and a frequency sweep in the linear viscoelastic region (0.1% strain) (C)

Creep compliance measurements also showed the biofilm behaved as a viscoelastic material with recovery of initial properties during the 2 minute recovery time (**fig. 3**). The compliance values were higher for 50Pa stress (**fig. 3 D-F**) than for 20Pa stress (**fig. 3 A-C**) indicating the stress was outside the linear viscoelastic regime and the *in situ* biofilm was more prone to deformation, however the 3 repeats showed similar behaviour suggesting that the material was not permanently weakened by the applied stress despite exceeding the limits of the linear regime.

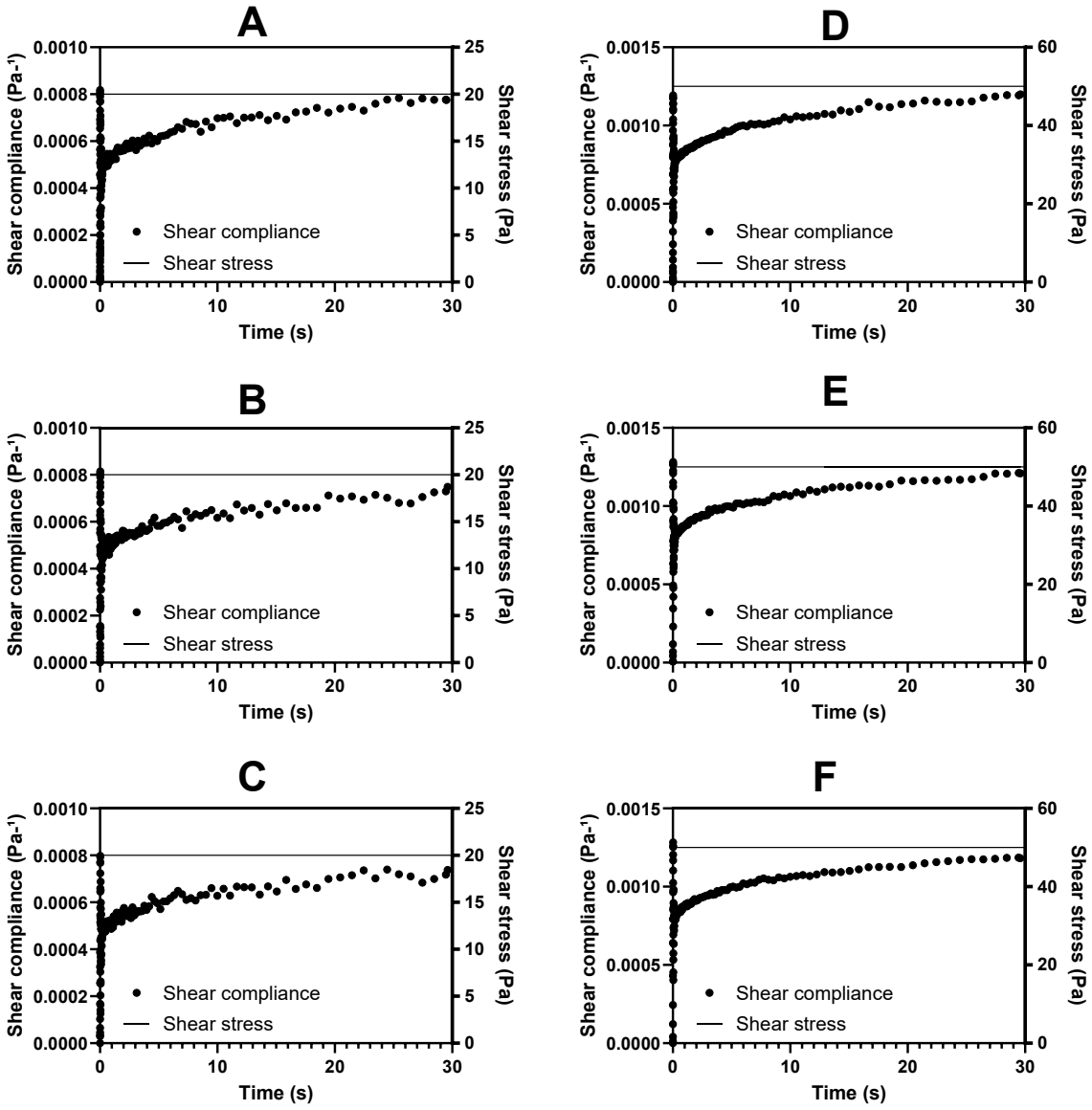

FIGURE 3. creep compliance of the *in situ* biofilm with 3 cycles of 20Pa constant stress for 30 seconds with 2 minutes recovery time (A-C), followed by 3 cycles of 50Pa constant stress for 30 seconds with 2 minutes recovery time (D-F)

DISCUSSION

This proof of principle study was intended to investigate the possibility of *in situ* measurements of rheology in biofilms present RAS bioreactors. To approach this question, we utilised laboratory scale nitrifying bioreactors and adapted carriers for initial testing. Visually, examination of the carrier surface suggested the presence of microbial biofilm material and the rheological testing carried out indicted a thin layer of viscoelastic material present on the carrier surface. The rheological data obtained indicate the biofilm was reasonably robust to perturbations, with repeated measures outside the linear viscoelastic regime generating similar data with relatively short recovery times (**fig. 2 A&B, fig. 3**). However, the *in situ* measurement system avoided the major perturbations linked to scraping and compression during loading onto the rheometer for testing that have been shown to significantly influence rheological results [5-7]. Whilst reported rheology of biofilms varies widely based on the microorganisms involved and the growing conditions [6-10], the data reported here show similar fundamental viscoelastic behaviours to previous reports, particularly for biofilms grown on solid supports [5, 6]. Based on these data, we believe the method has potential for monitoring aspects of biofilm stability in RAS.

1. Bamford, N.; MacPhee, C.; Stanley-Wall, N. Microbial Primer: An introduction to biofilms - what they are, why they form and their impact on built and natural environments. *Microbiology-Sgm* **2023**, *169* (8). DOI: 10.1099/mic.0.001338.
2. Elumalai, P.; Gao, X.; Cui, J.; Kumar, A.; Dhandapani, P.; Parthipan, P.; Karthikeyan, O.; Theerthagiri, J.; Kheawhom, S.; Choi, M. Biofilm formation, occurrence, microbial communication, impact and characterization methods in natural and anthropic systems: a review. *Environmental Chemistry Letters* **2024**, *22* (3), 1297–1326. DOI: 10.1007/s10311-024-01715-5.
3. Rurangwa, E.; Verdegem, M. Microorganisms in recirculating aquaculture systems and their management. *Reviews in Aquaculture* **2015**, *7* (2), 117–130. DOI: 10.1111/raq.12057.
4. Navada, S.; Vadstein, O.; Gaumet, F.; Tveten, A.; Spanu, C.; Mikkelsen, O.; Kolarevic, J. Biofilms remember: Osmotic stress priming as a microbial management strategy for improving salinity acclimation in nitrifying biofilms. *Water Research* **2020**, *176*. DOI: 10.1016/j.watres.2020.115732.
5. Daalkhaijav, U.; Walker, T. DEVELOPING A NONDESTRUCTIVE TECHNIQUE FOR MEASURING BULK RHEOLOGY OF PSEUDOMONAS AERUGINOSA BIOFILM. *Applied Rheology* **2017**, *27* (6). DOI: 10.3933/applrheol-27-64033.
6. Geisel, S.; Secchi, E.; Vermant, J. Experimental challenges in determining the rheological properties of bacterial biofilms. *Interface Focus* **2022**, *12* (6). DOI: 10.1098/rsfs.2022.0032.
7. Siri, M.; Sarlet, A.; Ziege, R.; Zorzetto, L.; Guzman, C.; Amini, S.; Hengge, R.; Blank, K.; Bidan, C. Mechanical Comparison of Escherichia coli Biofilms with Altered Matrix Composition: A Study Combining Shear-Rheology and Microindentation. *Acs Biomaterials Science & Engineering* **2025**, *11* (7), 4523–4536. DOI: 10.1021/acsbiomaterials.5c00261.
8. Beckwith, J.; Ganesan, M.; VanEpps, J.; Kumar, A.; Solomon, M. Rheology of Candida albicans fungal biofilms. *Journal of Rheology* **2022**, *66* (4), 683–697. DOI: 10.1122/8.0000427.
9. Gao, J.; Abriat, C.; Laekas-Hameder, M.; Virgilio, N.; Dozois, C.; Quach, C.; Heuzey, M.; Lemay, G.; Daigle, F. Microbiological and rheological dynamics of mixed biofilms formed by bacteria and eukaryotic virus. *Scientific Reports* **2026**, *16* (1). DOI: 10.1038/s41598-026-39314-9.
10. Rouillard, K.; Markovetz, M.; Kissner, W.; Boone, W.; Plott, L.; Hill, D. Altering the viscoelastic properties of mucus-grown Pseudomonas aeruginosa biofilms affects antibiotic susceptibility. *Biofilm* **2023**, *5*. DOI: 10.1016/j.bioflm.2023.100104.

MICRO-RHEOLOGY OF BIOLOGICAL AND BIO-ARTIFICIAL FLUIDS

Elke Bradt[1], Thessa-Carina Bauer[1], Sabine Hild[1], Andreas Gruber[2,3], Tobias Rossmann[2,3], Francisco Ruiz-Navarro[2,3], Johannes Oberndorfer[2,3], Harald Stefanits[2,3], Thomas Voglhuber-Brunnmaier[4], Alexander O. Niedermayer[4], Milan Kracalik[1]

[1]Institute of Polymer Science, Johannes Kepler University, Altenberger Str. 69, 4040 Linz, Austria
[2]Department of Neurosurgery, Kepler University Hospital, Wagner Jauregg Weg 15, 4020 Linz, Austria
[3]Clinical Research Institute for Neurosciences, Faculty of Medicine, Johannes Kepler University, Krankenhausstr. 5, 4020 Linz, Austria
[4]Institut für Mikroelektronik und Mikrosensorik, Science Park 1, Altenberger Str. 69, 4040 Linz, Austria

DOI: 10.31265/q5k1fv71

ABSTRACT

Microrheology is a quite new, but interesting technique in the biological field. This non-destructive measuring methods infers elastic and viscous flow parameters from the motion of embedded tracer particles using the generalized Stokes-Einstein relation. It is offering access from 1 to 10.000 Hz with small sample volumes (µl) and cellular-scale resolution. This study has been focusing on the viscosity of different biological fluids like cerebrospinal fluid (CSF, human), synovial fluid (SF, dog, horse) and artificial CSF and SF.

The viscoelastic behavior of the studied samples is largely attributable to their protein content. To test this, artificial cerebrospinal fluid (CSF) and synovial fluid (SF) as well as their individual components were prepared and analyzed, using the same parameters as for corresponding biological samples. To validate the method, measurements were compared with macro-rheological data and demonstrated that the results from both approaches are complementary[1,2,6,8].

INTRODUCTION

Microrheology studies the mechanical properties of viscous materials in a microscopic behavior. Due to the low sample amount and the non- destructive measuring technique, this method is quite interesting for biological probes. Compared with conventional rheology, microrheology can cover a broader frequency range from 1 to 10000 Hz. It has been shown that microrheological measurements agree very well with conventional double gap measurements. For this reason, this technique is perfect for biological samples due to the fact that it is often difficult to get enough sample volume for conventional measurements (e.g. tears, synovial fluid). This method can be divided in two different measuring types, i.e. the active and the passive. In active microrheology particles are driven by an external force, for example a magnetic field, whereas the passive form uses well defined and freely diffusing tracer particles exhibishing Brownian motion, driven by thermal energy. This mobility is measured to obtain the viscosity and the structure of the fluid. The mean square displacement (MSD) is an important parameter in microrheology for quantitative interpreting of the viscosity and sheer modulus of

the sample. In Newtonian fluids, the slope of the MSD directly yields the diffusion coefficient and thus the viscosity via the Stokes–Einstein relation. In viscoelastic samples, the MSD enabling determination of the frequency-dependent modulus from passive tracer motion [1,8,12].

In this study, artificial cerebrospinal fluid (CSF)[3,4,5,7,14], artificial synovial fluid (SF)[13], human cerebrospinal fluid, and synovial samples from dogs and horses were used [3,4,5]. It should be noted that the synovial fluid samples from dogs were collected from animals with joint problems, whereas the horse samples were taken from unaffected joints post mortem.

MATERIALS AND METHODS

Human CSF samples were collected from patients suffering from hydrocephalus, as part of the standard medical therapy.

Synovial fluid samples from dogs were collected from "Tierklinik Sattledt" as excess material during necessary treatments or examinations.

Synovial fluid sample from horses were collected from "Tierklinik Tillysburg" post mortem. As the horses showed no abnormalities in their gait or signs of discomfort, it was assumed that there were no pathological changes in the synovial fluid; however, no clinical examinations were performed.

Artificial SF

TABLE 1: Composition of artificial SF, with a concentration of 3 g/L in total[13].

Substance	Amount
Ig G	20 mg
Hyaluronic Acid, 1440 kDA	5,6 mg
Human Albumin (20%)	0,2 ml
Ringersolution	1,8 ml

Artificial CSF

TABLE 2: Composition of artificial CSF, with a concentration of 19 g/L in total[14].

Substance	Amount
Glucose	69,8 mg
Lactate	18,2 mg
Human Albumin	180 µl
Ringersolution	up to 100 ml in total

Collection

All fluids were collected under sterile conditions, and the samples were stored in sterile sample containers at 4 °C until measurement.

Conventional Rheometry

All samples were measured using the double-gap method with an Anton Paar rheometer (Anton Paar, MCR 702, Graz, Austria) at 37 °C with a double gap geometry (DG26.7/T200/SS).

Microrheology

For passive microrheology measurements, a sample volume of 1 mL was spiked with 30 µL of tracer particles (0.1 µm, Polystyrene, Sigma-Aldrich) in a plastic microcuvette and homogenized. Measurements were performed on the Malvern Zetasizer Nano Plus with a 621 nm laser at a 173° backscattering angle at 37 °C.

Conventional Rheology

The measurements were performed on an Anton Paar Rheometer 702, with the double gap method also at 37 °C[9,10,11].

High Frequency Rheology

An electromechanical quartz crystal tuning fork (dimensions of 6x1,5x0,35mm³) vibrates at a frequency of 25 - 28 kHz with amplitudes in the nm range. Fluid forces acting on the vibrating element change the resonance characteristics of the electrical frequency response. From these changes the sheer moduli are determined. The exact sheer rates are non-unform und unknown,

but low. Also, the vibration frequency cannot be adjusted. However, this method is most sensitive to changes of rheological fluid properties and features additional benefits including low sample volume, fast temperature control, low cleaning effort, high robustness, and low fouling due to conformal parylene coating of the sensor.

RESULTS AND CONCLUSION

Comparing microrheological measurements of hyaluronic acid and humane albumin (**Fig. 1**) shows stronger interactions in humane albumin compared to pure hyaluronic acid, which suggests the formation of a protein network in the human albumin. All measurements are performed at body temperature for better comparison of the results.

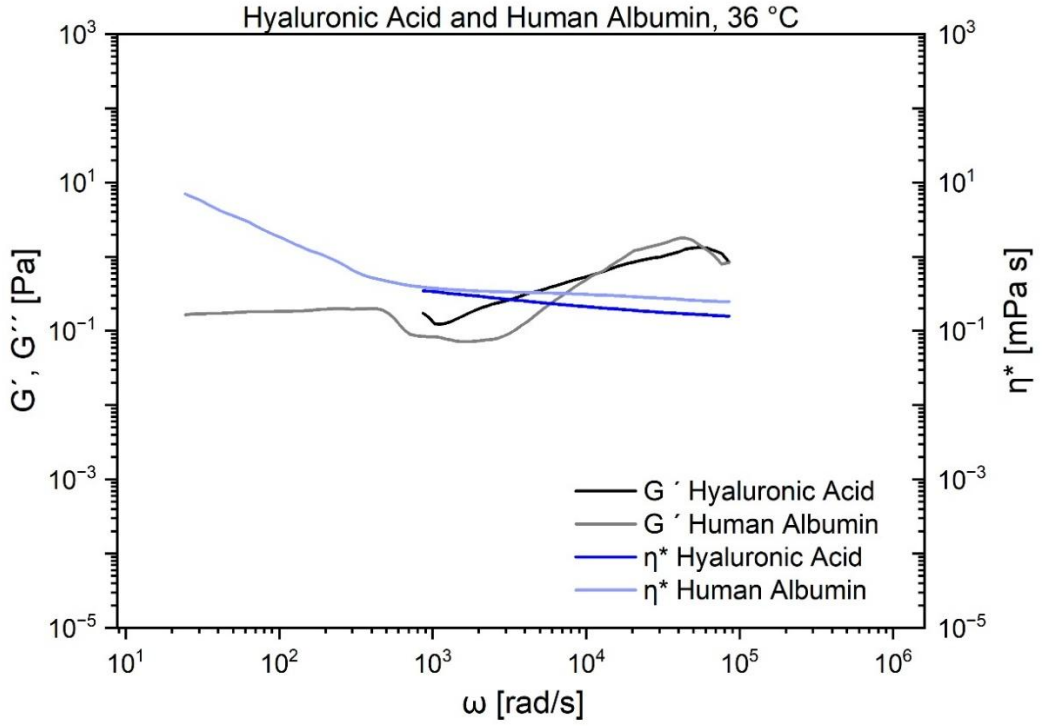

FIGURE 1: Storage modulus and viscosity of hyalurionic acid and humane albumin at 36 °C.

In **Fig. 2**, artificial synovial fluid was compared with the synovial fluid of a horse and a dog. It can be shown that the storage modulus and viscosity of the artificial synovial fluid behave similarly to those of the horse. In contrast, the values for the dog's synovial fluid are lower. One possible reason is that the dog suffered from joint disorder, whereas the horse showed no abnormalities in its joint apparatus.

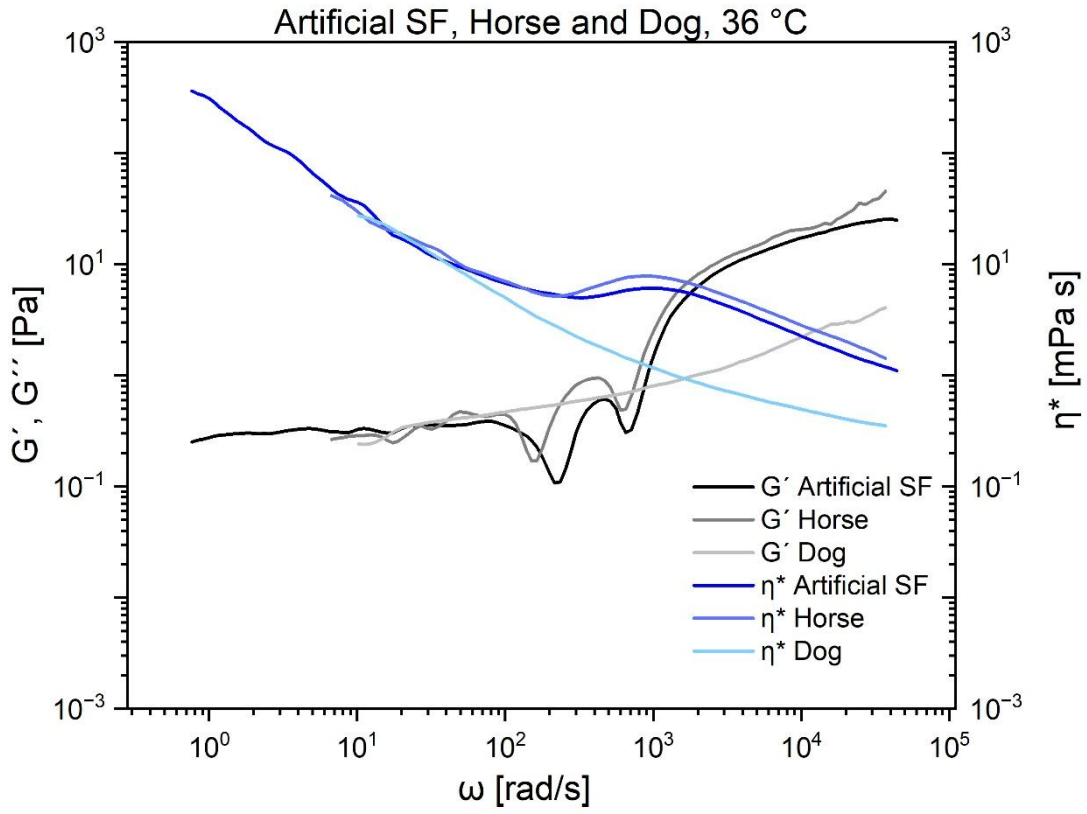

FIGURE 2: Storage modulus and viscosity of artificial SF and SF from horse and dog at 36 °C.

Fig. 3 shows a comparison between human CSF and artificial CSF. The storage modulus and viscosity values of the human samples are very similar, whereas the artificially prepared CSF falls within a much higher frequency range, and its viscosity is below the storage modulus.

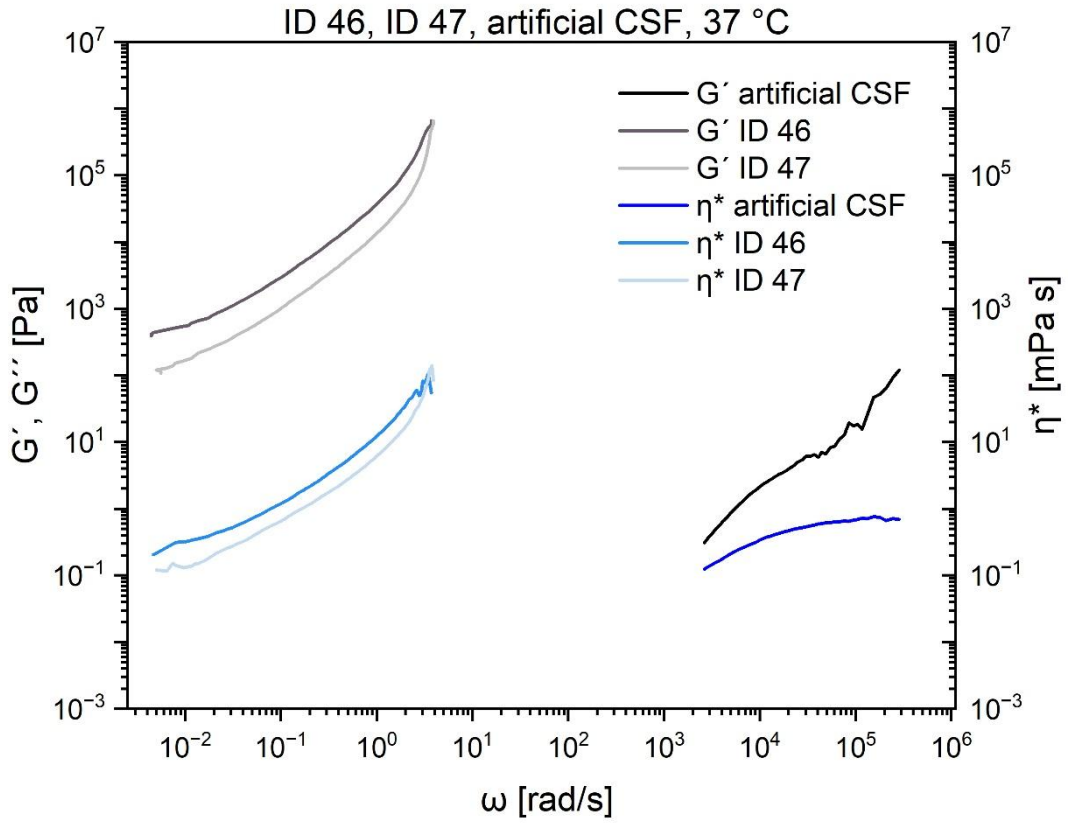

FIGURE 3: Storage modulus and viscosity of artificial CSF, ID 46 and ID 47 at 37 °C.

In **Fig. 4**, the integration of conventional rheology with microrheology is shown. On the right, a red dot marks a measurement with a high-frequency sensor. It was demonstrated that all three measurement methods agree very well and can be effectively combined. In other words, microrheological measurements on biological samples with small sample volumes can provide a good prediction for the frequency range of conventional measurements [5].

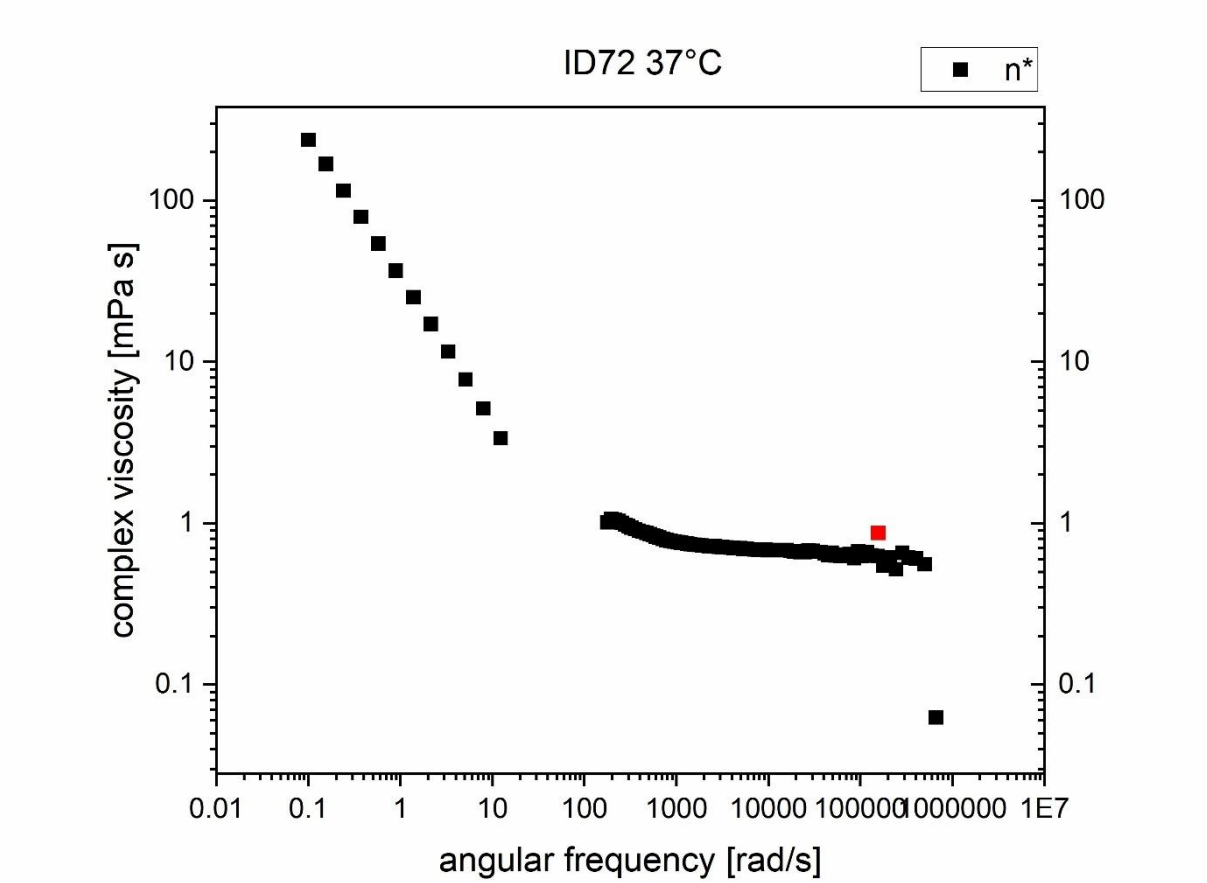

FIGURE 4: Comparison of Micro- (right hand side) and Macrorheology (left hand side) and a red sensor point of ID 72 at 37 °C.

In summary, it can be shown that biological samples from humans and animals exhibit a network structure that is less pronounced in artificially prepared solutions. These viscous properties are important for joint lubrication in the case of synovial fluid. In patients with hydrocephalus, the viscosity of the CSF might become an important clinical parameter for deciding whether a shunt will be necessary after intraventricular or subarachnoid hemorrhage. Initial experiments with a high-frequency sensor showed that this very fast method also yields values similar to those from microrheological investigations. Further samples need to be examined and compared with laboratory parameters, and the artificial solutions may need to be adjusted to achieve better viscosity values.

REFERENCES

1. Yating, M.; Paige, N.; Jamel, A.; Passive and Active Microrheology for Biomedical Systems. Frontiers in Bioengineering and Biotechnology **2022**, 10:916354. https://doi.10.3389/fbioe.2022.916354.
2. Bradt, E.; Hild, S.; Reichel, E.K.; Kracalik, M. Microrheology of Biofluids. In Book of Abstracts Annual European Rheology Conference, Sorrento, Italy, 17–18 April **2018**; European Society of Rheology: Zurich, Switzerland, 2018.
3. Tomaiuolo, G.; Carciati, A.; Caserta, S.; Guido, S. Blood linear viscoelasticity by small amplitude oscillatory flow. Rheol. Acta **2016**, 55, 485–495.
4. Barrand, M.; Hladky, S. Mechanisms of fluid movement into, through and out of the brain: Evaluation of the evidence. Fluids Barriers CNS **2014**, 11, 26.
5. Ropper, A.H.; Samuels, M.A.; Klein, J.P. Adams & Victor's Principles of Neurology, 10th ed.; McGraw-Hill Education: New York, NY, USA, **2014**; pp. 615–638.
6. Bauer, T.; Bradt, E.; Hild, S.; Gruber, A.; Rossmann, T.; Navarro, F.; Oberndorfer, J.; Stefanits, H.; Kracalik, M.; Analysis of interactions in cerebrospinal fluid under different temperature conditions using rotational rheometry, Biorheology 59 (**2022/2023**) 99–112. https:// 10.3233/BIR-239002.
7. Bauer, T.; Bradt, E.; Hild, S.; Gruber, A.; Rossmann, T.; Navarro, F.; Oberndorfer, J.; Stefanits, H.; Kracalik, M.; Rheological Characterization of Cerebrospinal Fluid Under Different Temperature Conditions, Fluids **2026**, 11 (2), 38. https://doi.org/10.3390/fluids11020038.
8. Bradt, E.; Bauer, T.; Hild, S.; Gruber, A.; Rossmann, T.; Navarro, F.; Oberndorfer, J.; Stefanits, H.; Kracalik, M.; Application of macro- and microrheology for biological fluids, Biorheology 59 (**2022/2023**) 99–112. https:// 10.3233/BIR-239002.
9. Addis, A.; Gaasch, M.; Schiefecker, A.J.; Kofler, M.; Ianosi, B.; Rass, V.; Lindner, A.; Broessner, G.; Beer, R.; Pfausler, B.; et al. Brain temperature regulation in poor-grade subarachnoid hemorrhage patients—A multimodal neuromonitoring study. J. Cereb. Blood Flow Metab. **2021**, 41, 359–368.
10. Kunitsyn, V.G.; Panin, L.E.; Polyakov, L.M. Anomalous change of viscosity and conductivity in blood plasma lipoproteins in the physiological temperature range. Int. J. Quantum Chem. **2001**, 81, 348–369.
11. Michieletto, D.; Marenda, M. Rheology and Viscoelasticity of Proteins and Nucleic Acids Condensates. JACS Au **2022**, 2, 1506–1521.
12. Weihs, D.; Mason, T. G.; Teifel, M. A.; Bio-Microrheology: A Frontier in Microrheology, Biophysical Journal, Volume 91, 4296-4305.
13. Bortel, E.L.; Charbonnier, B.; Heuberger, R.;Development of a Synthetic Synovial Fluid for Tribological Testing, Lubricants 3 (4), **2015**, S. 664-686 https://doi.org/10.3390/lubricants3040664.
14. Wilhelm F.; Krause, M.; Schob S.;Merkenschlager, A.; Wachowiak, R.;Härtig, W.; Meixenberger, J.; Gburek-Augustat, J.; Wende, T.; Cerebrospinal Fluid Protein Concentrations in Hydrocephalus, Children **2023**, 10(4), 644. https://doi.org./10.3390/children10040644.

This study involving human samples was approved by the Ethics Commitee, Faculty of Medicine, Johannes Kepler University Linz, MED Campus I, ADMBuilding 7th Floor, Krankenhausstaße 5, 4020 Linz (approval No. 1025/2022) on 1 July 2022. This study was conducted in accordance with local legislation and institutional requirements. The participants provided written informed consent to participate in this study.

RHEOLOGY OF BIOLOGICAL AND BIO-ARTIFICIAL FLUIDS

Thessa-Carina Bauer[1], Elke Bradt[1], Sabine Hild[1], Andreas Gruber[2,3], Tobias Rossmann[2,3], Francisco Ruiz-Navarro[2,3], Johannes Oberndorfer[2,3], Harald Stefanits[2,3], Milan Kracalik[1]

[1]Institute of Polymer Science, Johannes Kepler University, Altenberger Str. 69, 4040 Linz, Austria
[2]Department of Neurosurgery, Kepler University Hospital, Wagner Jauregg Weg 15, 4020 Linz, Austria
[3]Clinical Research Institute for Neurosciences, Faculty of Medicine, Johannes Kepler University, Krankenhausstr. 5, 4020 Linz, Austria

DOI: 10.31265/7cvfy049

ABSTRACT

Although rheology is not widely utilized in medical research as compared to polymer science, it can provide valuable contributions wherever biological fluids are studied. Rheology applies a certain mechanical load to the sample and the receiving flow properties are measured. This can help to investigate the flow behavior of biological fluids under simulated "natural" conditions and achieve a better understanding of the flow behavior of these fluids.

This study focused on investigating the flow behavior of cerebrospinal fluid (CSF, human) and synovial fluid (SF, horse). A closer look at CSF and SF shows that these biological fluids exhibit certain similarities to polymer solutions. CSF and SF are aqueous solutions which contain certain amounts of macromolecules, such as different proteins. These macromolecular components are only present in low concentrations; however, they are expected to be responsible for the specific flow behavior. In order to support this relation, corresponding artificial bio-fluids were prepared and rheologically characterized following the same procedure as for the biological fluids. Specific interactions in such biological fluids can be reflected by viscoelasticity. Therefore CSF, SF and the relevant artificial fluids were compared based on their viscoelastic behavior.

The overall goal is to gain a better understanding of the rheological behavior of these biological fluids and their response to applied mechanical load in shear flow. Additionally, it is investigated whether rheological measurements can aid clinical practice for disorders involving CSF or SF.

INTRODUCTION

Studying the flow behavior of materials is a cornerstone of polymer science as it allows for the mechanical characterization of polymer samples. Rheology is comparatively underrecognized in the medical sciences[1, 2]. Biological fluids are typically dilute aqueous matrices that contain macromolecular components, such as proteins, which are expected to modulate their flow and viscoelastic properties[3-5]. Biological materials rarely behave as ideal elastic solids or ideal viscous liquids. Instead, constituent interactions in synovial (SF) and cerebrospinal fluids (CSF) lead to viscoelasticity[6]. Viscoelasticity can be investigated using oscillatory rheometry, which quantifies the elastic component (storage modulus, G′) and the viscous component (loss modulus, G″)[7]. Rheology may provide a positive contribution to characterizing the flow

behavior of biological fluids and further on to evaluating whether rheological parameters may provide an addition to the treatment decisions in the clinical routine.

This study focused on equine SF, CSF from human hydrocephalus patients, and artificial alanogues to determine how individual components influence the specific flow behavior. SF acts as a lubricant, supplies the avascular articular cartilage with nutrients and removes metabolic waste[8]. CSF serves to protect the brain and spinal cord and therefore must exhibit properties that enable effective mechanical cushioning and regulatory properties[9]. Some studies have already been focused on the investigation of artificial fluids. Bortel et al.[10] formulated artificial SF to make joint prosthesis wear testing more physiologically realistic. Artificial CSF has also been investigated by Zheng et al.[11] to replicate the ionic composition of native CSF, thereby providing a controlled, physiologically relevant medium for reproducible experiments. Therefore all samples the biological, as well as the bio-artificial samples were rheologically investigated with a rotational rheometer, equipped with a measuring geometry especially for low viscosity fluids[12].

MATERIAL AND METHODS

SF samples were drawn postmortem from horses of the vet clinic Tillysburg. The CSF samples were drawn from human hydrocephalus patients via an external ventricular drainage places for routine treatment after intracranial hemorrhage at the Department of Neurosurgery, Kepler University Hospital and Johannes Kepler University Linz.

To enable a more detailed investigation, artificial analogues were prepared from its principal composition and most relevant constituents. CSF consist of proteins, glucose, lactate and electrolytes[3, 4]. Given that albumin is reported to account for more than 50% but less than 75% of total protein, albumin was assumed to represent the protein fraction[3]. For the synovial fluid analogue, a hyaluronan solution was applied[10]. Human Albumin (20%), D(+)Glucose, Sodium L-Lactate and a ringer solution were used for preparation.

Table 1 presents the sample composition of the artificial CSF which was prepared in 100 mL ringer solution [3, 4]. Additionally an albumin solution (19 g/L) and a hyaluronic acid (HA) solution (3 g/L) were prepared in ringer solution.

TABLE 1: Compostion of artificial samples[3, 4].

Sample	Albumin	Glucose	Lactate
aCSF	180 µL	68.7 mg	18.6 mg

For the rheological measurements a rotational rheometer Physica MCR702 (Anton Paar Ltd., Graz, Austria) with a double gap geometry (DG26.7/T200/SS). Rotational and oscillatory rheological tests were conducted to characterize the steady-shear and viscoelastic behavior. The measurement parameters were applied as shown in **Table 2.**[12].

TABLE 2: Measurment parameters for rheology[12].

measurement	shear rate / s^{-1}	Angular fregency / rad s^{-1}	deformation / %
Rotational test	1-700	-	-
Amplitude test	-	10	0.01-100
Frequency test	-	0.1-628	10

To simulate relevant conditions in human and veterinary contexts, measurements were conducted at defined temperatures. For human CSF, the setpoints were: 5°C (storage), 35°C (hypothermic), 37°C (physiological), and 40°C (elevated body temperature). For equine synovial fluid, measurements were performed at 5°C (storage), 20°C (room temperature), 36°C (hypothermic), 37°C (physiological), and 39°C (elevated body temperature).

RESULTS AND DISCUSSION

The roatational test showed a non-Newtonial behavior in the low shear rate range for both the human CSF and the artificial CSF, meaning the viscosity is changing with varying shear rate (**Fig. 1.**). The higher the shear rate the more unaffected the viscosity is and resulting in an Newtonial behavior.

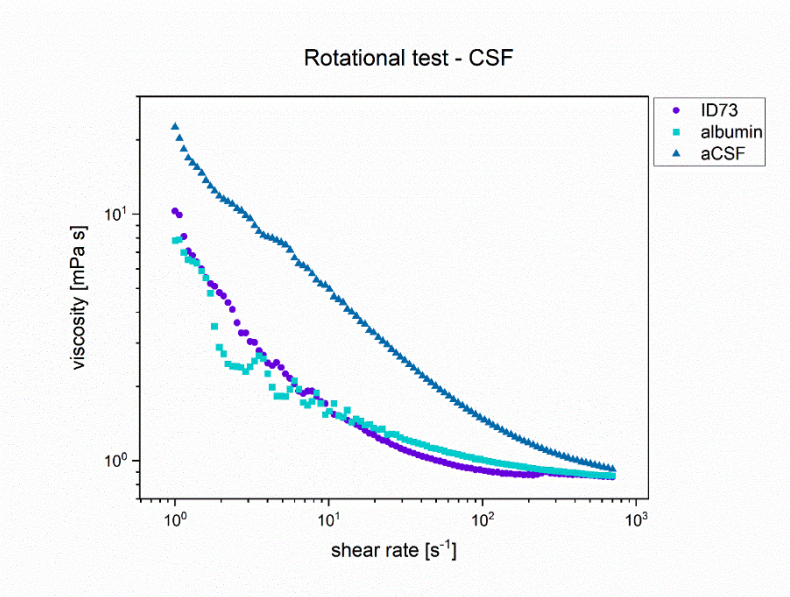

FIGURE 1: Rotational test comparision of albumin solution, artificial CSF and human CSF ID73. Non-Newtonian behavior in the low shear rate range, but with increasing shear rate viscosity is getting constant.

In **Fig. 2**. The rotational test of equine SF shows decreasing viscosity with increasing shear rate over the whole measurement range. In contrast to the hyaluron solution which exhibits a long Newtonian plateau.

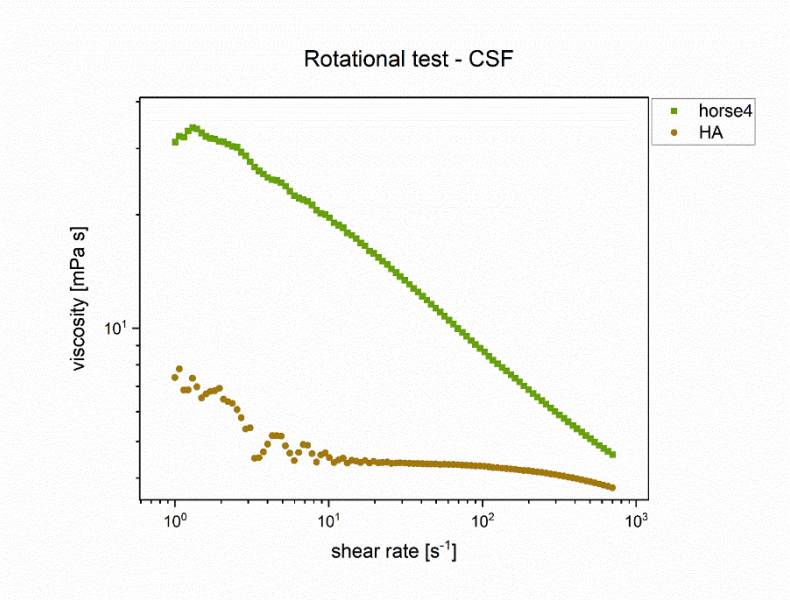

FIGURE 2: Rotational test comparison of HA and equine SF.

Prior to the frequency test amplitude tests were performed to define the linear viscoelastic region of the samples to ensure reversible deformation. In **Fig. 3.** and **Fig. 4.** the amplitude tests are shown. For all samples 10% deformation were preset for the frequency test.

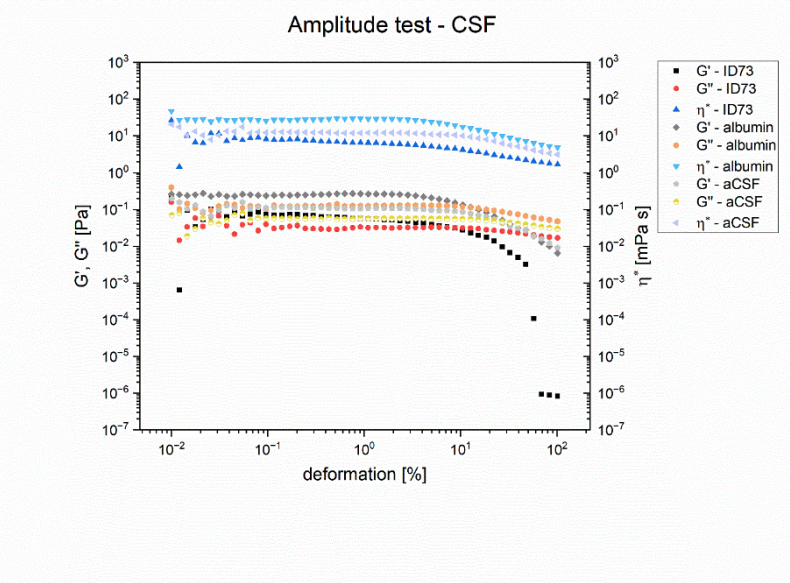

FIGURE 3: Amplitude test comparision of albumin solution, artificial CSF and human CSF ID73.

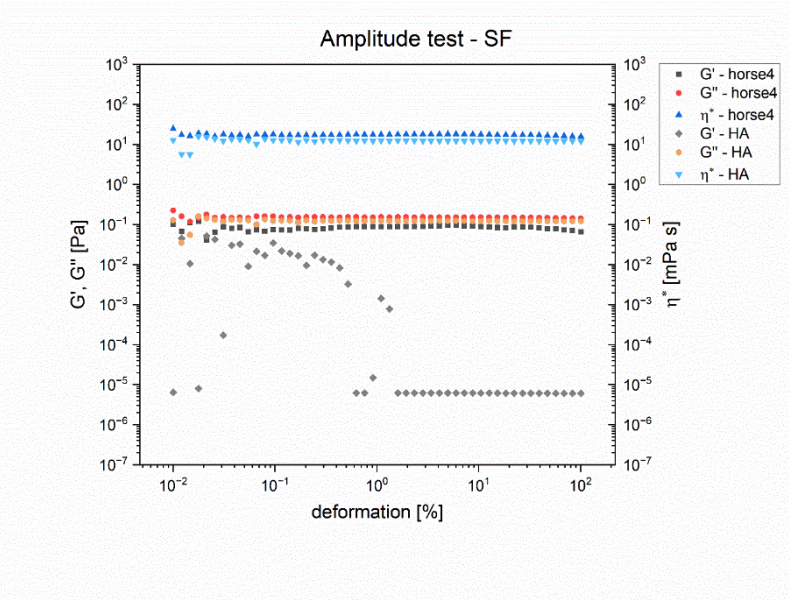

FIGURE 4: Amplitude test comparision of hyaluronic acid and equine SF.

In the case of CSF, an albumin solution, the artificial CSF and human CSF (ID73) were compared in the frequency test, shown in **Fig. 5.** Albumin is showing the lowest curves and storage modulus (G') curve is even lower than the loss modulus (G'') curve different from the artificial CSF and the human CSF. This suggests that the albumin solution is more viscose dominated compared to the other two. The complex viscosity shows shear thinning behavior as the viscosity decreases with increasing angular frequency. Human CSF shows the highest viscosity compared to the artificial CSF and the albumin solution.

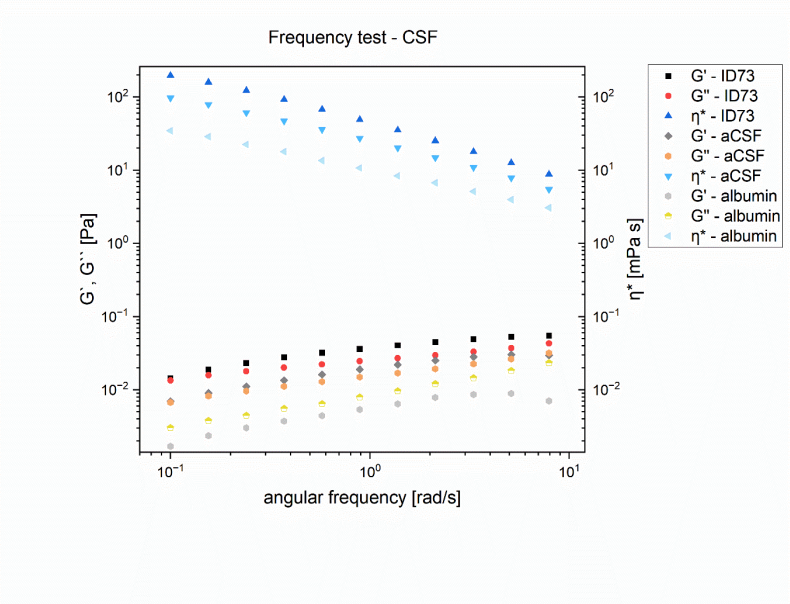

FIGURE 5: Frequency test comparison albumin solution, artifical CSF and human CSF ID73.

The horse SF and the hyaluronic acid solution are much more different compared to the CSF system, which can be seen in **Fig. 6.** For the horse SF and the albumin solution the loss modulus curve is higher than the storage modulus curve intending higher viscous amount in the flow behavior. The G' and G'' curves of the horse SF are much more steep, resulting in an increased frequency dependancy. That contrasts with the complex viscosity showing a flatter, near-Newtonian plateau.

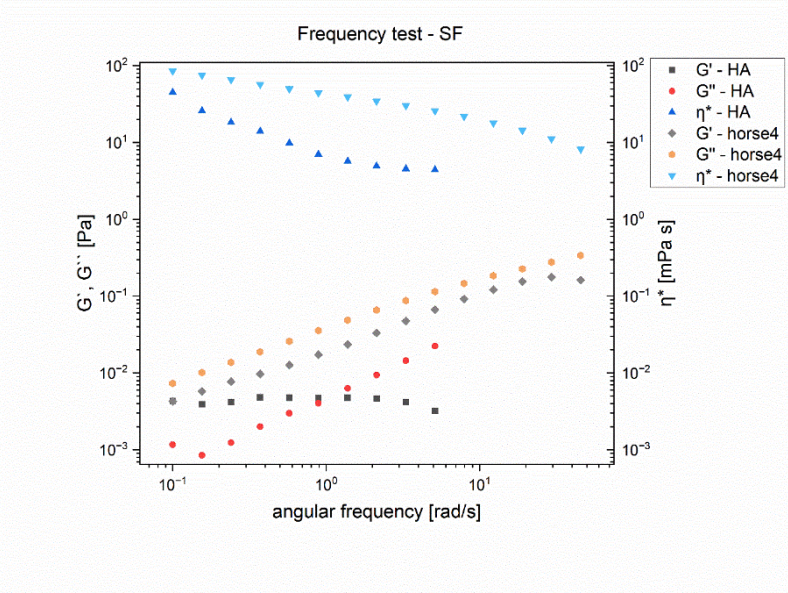

FIGURE 6: Frequency test comparision HA solution and equine SF.

Comparing the different temperature conditions applied for the frequency test is shown in **Fig. 7.** and **Fig. 8.** Both figures show the same tendency with inceasing temperature the values for storage, loss modulus and complex viscosity are increasing. This is acting against the natural trend that would be expacted to be decreasing viscosity with increasing temperature. For proteins it is known that at higher temperature thermical induced structural changes can appear[13]. This could be one reason for the unexpected trend. **Fig. 8.** shows the frequency test of the hyaluron soluction with defined measurement temperatures. The complex viscosity curve changes the shape between the low temperature measurements (5°C, 20°C) and the higher temperature measurements (35°C, 37°C, 40°C). At low temperatures the complex viscosity curve has a Newtonian shape, but with increasing temperature a shear thinning behavior appears.

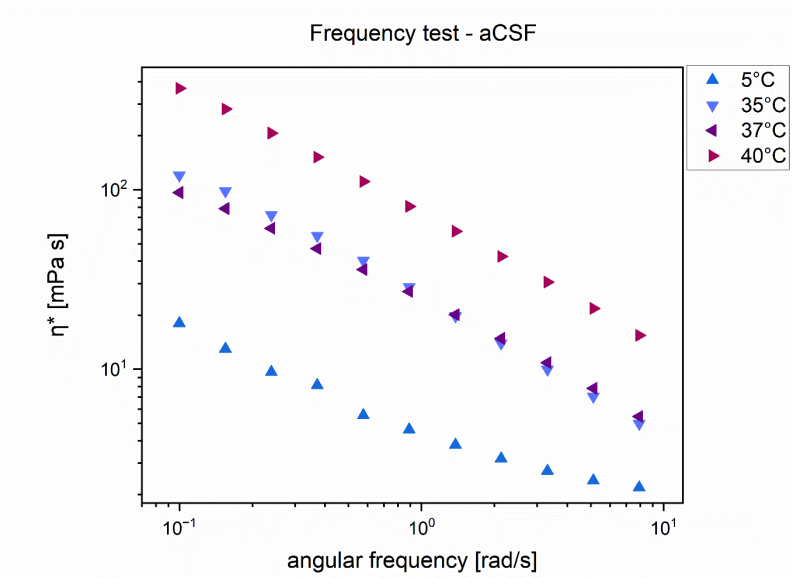

FIGURE 7: Frequency test of artificial CSF over defined measurment temperatures.

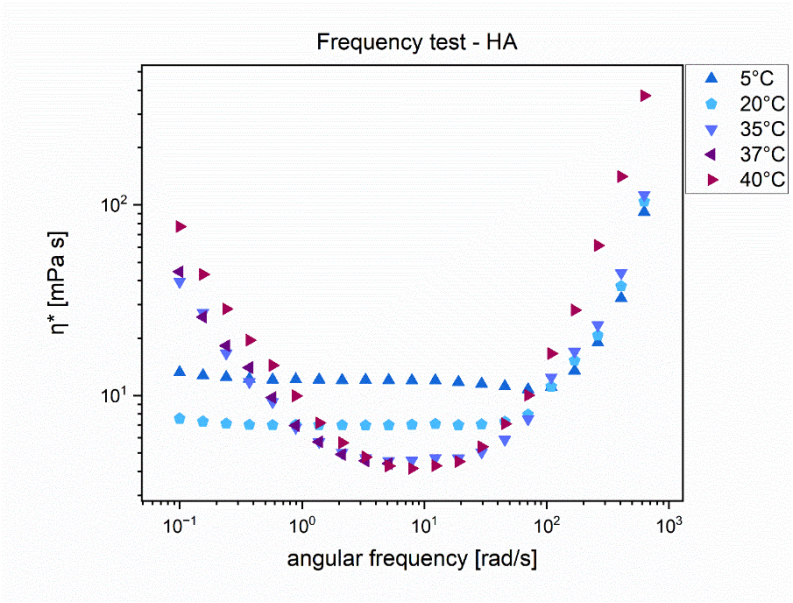

FIGURE 8: Frequency test of hyaluron solution over defined measurement temperatures.

CONCLUSION

The rheological measurements show that albumin and hyaluronic acid have a big influence on the flow behavior of the CSF and SF and potentially provide an effort for a better understanding of the rheological behavior of these biological fluids and their response to applied mechanical force. Further investigations will focus on the temperature trend and the influence of different components of the flow properties to reach the overall goal to evaluate if rheological parameters can positively contribute to clinical practice for CSF and SF disorders.

Ethical Statement: This study involving human samples was approved by the Ethics Committee, Faculty of Medicine, Johannes Kepler University Linz, MED Campus I, ADMBuilding 7th Floor, Krankenhausstaße 5, 4020 Linz (approval No. 1025/2022) on 1 July 2022. This study was conducted in accordance with local legislation and institutional requirements. The participants provided written informed consent to participate in this study.

Funding: The authors acknowledge the financial support of the Faculty of Medicine of the Johannes Kepler University Linz through its internal funding program Impetus Nr. I-10-22 and the LIT Institute of Technology of the Johannes Kepler University Linz, project number LIT-2022-11-SEE-123.

Conflicts of Interest: The authors have no conflicts to disclose.

REFERENCES

1. Bloomfield, I. G.; Johnston, I. H.; Bilston, L. E. Effects of proteins, blood cells and glucose on the viscosity of cerebrospinal fluid. *Pediatric neurosurgery* **1998**, *28*, 246–251. https://doi.org/10.1159/000028659.
2. Hollister, J. C. P.; Wang, A. C.; Kim, W.; Giza, C. C.; Prins, M. L.; Kavehpour, H. P. Shear thinning behavior of cerebrospinal fluid with elevated protein or cellular concentration. *Frontiers in Physics* **2023**, *11.* https://doi.org/10.3389/fphy.2023.1308136.
3. Wilhelmy, F.; Krause, M.; Schob, S.; Merkenschlager, A.; Wachowiak, R.; Härtig, W.; Meixensberger, J.; Gburek-Augustat, J.; Wende, T. Cerebrospinal Fluid Protein Concentrations in Hydrocephalus. *Children* **2023***, 10*(4), 644. https://doi.org/10.3390/children10040644.
4. Czarniak, N.; Kamińska, J.; Matowicka-Karna, J.; Koper-Lenkiewicz, O.M. Cerebrospinal Fluid–Basic Concepts Review. *Biomedicines* **2023**, 11, 1461. https://doi.org/10.3390/biomedicines11051461.
5. Bauer, T.-C.; Bradt, E.; Hild, S.; Gruber, A.; Rossmann, T.; Ruiz-Navarro, F.; Oberndorfer, J.; Stefanits, H.; Kracalik, M. Rheology of Cerebrospianl Fluid under Different Temperature Conditions. *Annu. Trans. Nord. Rheol. Soc.* **2023**, *31*, 87–92.
6. Michieletto, D.; Marenda, M. Rheology and Viscoelasticity of Proteins and Nucleic Acids Condensates. *JACS Au* **2022**, 2, 1506–1521. DOI: 10.1021/jacsau.2c00055.
7. Kracalik, M. Recycled clay/PET nanocomposites evaluated by novel rheological analysis approach. *Appl. Clay Sci*. **2018**, 166, 181–184. https://doi.org/10.1016/j.clay.2018.09.007.
8. Edwards, N.L. Cellular Components of Synovial Fluid in Health and Disease. In: Mandell, B.F. (eds) Synovial Fluid Analysis and The Evaluation of Patients With Arthritis. *Springer, Cham.* **2022**. https://doi.org/10.1007/978-3-030-99612-3_5..
9. Hladky, S.B.; Barrand, M.A. Mechanisms of fluid movement into, through and out of the brain: evaluation of the evidence. *Fluids Barriers* **2014**,CNS 11, 26. https://doi.org/10.1186/2045-8118-11-26.
10. Bortel, E.L.; Charbonnier, B.; Heuberger, R. Development of a Synthetic Synovial Fluid for Tribological Testing. *Lubricants* **2015**, 3, 664-686. https://doi.org/10.3390/lubricants3040664.
11. Zheng, W. H.; Yan, C.; Chen, T.; Kang, D. Z. New scheme for the preparation and use of artificial cerebrospinal fluid. *Journal of physiology and pharmacology* **2020**, 71(6), https://doi.org/10.26402/jpp.2020.6.15.
12. Bauer, T.-C.; Bradt, E.; Hild, S.; Gruber, A.; Rossmann, T.; Ruiz-Navarro, F.; Oberndorfer, J.; Stefanits, H.; Kracalik, M. Rheological Characterization of Cerebrospinal Fluid Under Different Temperature Conditions. *Fluids* **2026**, 11, 38. https://doi.org/10.3390/fluids11020038.
13. Anomalous change of viscosity and conductivity in blood plasma lipoproteins in the physiological temperature range. *Int. J. Quantum Chem.* **2001**, 81, 348–369. DOI: 10.1002/1097-461X(2001)81:5<348:AID-QUA1004>3.0.CO;2-H.

Cellulosic Systems

RHEOLOGY OF MECHANO-ENZYMATICALLY FIBRILLATED CELLULOSE IN FIBER SUSPENSIONS AND FOAMS

Juliane Kade[1], Janika Viitala[1], Titta Kiiskinen[1], Panu Lahtinen[2], Olli Ville Laukkanen[1]

[1]VTT Technical Research Centre of Finland, FI-40101 Jyväskylä, Finland
[2]VTT Technical Research Centre of Finland, FI-02150 Espoo, Finland

DOI: 10.31265/s094x503

ABSTRACT

Cellulosic materials are increasingly explored as renewable building blocks for applications such as packaging, insulation, and construction. Conventional production of microfibrillated cellulose (MFC) is energy intensive and results in suspensions with strong gel-like behavior even at low solids contents.[1-3] High-consistency mechano-enzymatic fibrillation of cellulose (HC MFC, previously referred as HefCel) has emerged as a lower-energy alternative, enabling the production of MFC directly at high solid contents.[2, 4]

In this work, the rheological behavior of HC MFC is investigated over a range of concentrations in both fiber suspensions and fiber foams. Two grades of HC MFC, coarse and fine, are studied to elucidate the effects of fiber content and fibrillation degree on viscoelastic and flow properties. Commercial MFC is used as a reference material to benchmark the behavior of HC MFC against established systems.

The results show that HC MFC suspensions and foams exhibit a predominantly elastic response at small deformations over the entire range of fiber consistencies studied (2.5-15 wt% for suspensions, 2.5-7.5 wt% for foams). Rheological properties depend systematically on fiber content and fibrillation degree, reflecting differences in fiber network strength. Compared with commercial MFC, HC MFC shows much lower stiffness and therefore improved processability at high fiber consistencies. These findings support the potential of HC MFC in the production of sustainable, low-density fiber-based materials.

INTRODUCTION

Cellulosic materials have attracted significant attention as renewable and sustainable building blocks for a wide range of applications, including packaging, insulation, and construction. Among these, microfibrillated cellulose (MFC) has emerged as a versatile material due to its high surface area, tunable network structure, and ability to form strong, lightweight, and porous assemblies.[5-7] However, conventional routes for producing MFC rely primarily on intensive mechanical fibrillation processes, often preceded by limited chemical or enzymatic pretreatments. These methods are typically energy demanding and yield dilute suspensions that exhibit pronounced gel-like behavior even at low solids contents, which complicates handling, transport, and downstream processing.[3]

To address these limitations, alternative production strategies have been developed that improve both process efficiency and material functionality. In particular, high-consistency (HC) processing has gained interest to enhance fibrillation efficiency while reducing water usage.[8] In this context, consistency refers to the mass fraction of dry fibers in the system, typically expressed as a percentage relative to the total mass of the suspension or foam. At elevated solid contents, increased fiber–fiber friction during mechanical treatment promotes structural disruption of the fiber walls. When combined with enzymatic treatment, this effect is further amplified: the reduced water content enables enzymes to more effectively locate, recognize, and adsorb onto cellulose surfaces, thereby enhancing their catalytic activity.[8] As a result, high-consistency mechano-enzymatic pretreatment can facilitate more efficient fiber breakdown compared to purely mechanical or enzymatic approaches alone, enabling extensive fibrillation that has not been observed in conventional processes.

A key advantage of HC mechano-enzymatic fibrillation is the ability to produce MFC directly at high solids contents, typically in the range of 20–25%.[4, 8] This represents a significant departure from conventional dilute systems and introduces practical benefits such as reduced water handling, improved process economics, and enhanced feasibility for off-site production and long-distance transportation. Moreover, the resulting material exhibits a paste-like, non-gel character, making it easier to handle, store, and process in industrial applications. The process is also adaptable, allowing the production of different grades of HC MFC—such as coarse and fine fibrillated fiber materials—by tuning processing conditions and the degree of fibrillation. Additionally, the approach is compatible with a wide range of lignocellulosic feedstocks, including wood and non-wood pulps, recycled fibers, textile waste, and agricultural residues, further supporting its relevance within circular material systems.[2, 4, 8]

Beyond production, understanding the rheological behavior of fibrillated cellulose systems is essential for their practical utilization, as rheology governs processability, structural stability, and end-use performance in applications ranging from coating and forming to foam structuring and additive manufacturing.[9-11]

While the rheological properties of conventional MFC suspensions have been studied extensively, comparatively little is known about the behavior of HC MFC systems, particularly at high solids contents and in structured forms such as fiber foams. Fiber foams are of particular interest due to their potential to reduce drying energy requirements, as their lower water content and high porosity facilitate more energy-efficient processing compared to conventional suspension processing.[12, 13]

In this context, the present study investigates the rheological behavior of HC MFC across a range of concentrations in both fiber suspensions and fiber foams. Two grades of HC MFC — coarse and fine — are examined to elucidate the influence of fibrillation degree and fiber content on viscoelastic and flow properties. To provide a meaningful benchmark, a commercial MFC product is included as a reference material, enabling direct comparison between HC MFC and established systems at equivalent solid and air contents. Through this approach, the work aims to advance the fundamental understanding of HC MFC rheology and to support its further development as a sustainable platform for low-density, fiber-based material applications.

MATERIALS AND METHODS

High-consistency mechano-enzymatically fibrillated cellulose (HC MFC, previously referred to as HefCel) was produced from bleached softwood kraft pulp (BSKP) using a 7 L Winkworth sigma mixer (MZ7).[4]

For the production of the standard (coarse) HC MFC grade, the pulp was subjected to simultaneous mechanical mixing and enzymatic treatment at a solids content of 25%. An enzyme dosage of 4.5 mg per gram of dry pulp was applied. The treatment was carried out at pH 5 and temperatures of 50°C and 70°C under gentle mixing for a total duration of 5.5 h.

To obtain the fine HC MFC grade, the coarse material was further processed by high-pressure homogenization using a microfluidizer. This treatment was performed at a solids content of 10%, and the suspension was passed once through the microfluidizer at a pressure of 1800 bar.

The resulting HC MFC materials were used as produced for subsequent suspension preparation, foam fabrication, and rheological characterization.

The as-received consistencies of the materials were 17.5% for the coarse grade and approximately 10% for the fine grade. A commercial MFC material was used as a reference.

Fibre morphology was characterized using a Valmet FS5 fibre image analyzer to quantify key parameters such as fibre length, width, and fines content, as shown in **Table 1**. The measurements were conducted according to the standard operating procedure of the instrument to ensure reproducibility and comparability between samples.

TABLE 1: Fiber properties of the two high-consistency (HC) MFC types, coarse and fine grade.

	Coarse grade	Fine grade
Fiber length, mm (Tappi)*	0.205	0.200
Fiber width, µm	29.58	22.98
F1(I) 0.00-0.20 mm, %**	94.0	99.4
Fines, %	99.08	99.95

*Length-weighted average fiber length, Tappi T271 0.1-7 mm.
**represents the percentage of fibres, determined by image analysis, with lengths between 0.00 and 0.20 mm, corresponding to the fines fraction of the sample.

In addition, optical microscopy was employed to qualitatively assess fibre structure and degree of fibrillation (**Fig. 1**). To enhance image contrast and improve the visibility of fibrillar features, Congo red dye was applied as a staining agent prior to imaging.[4]

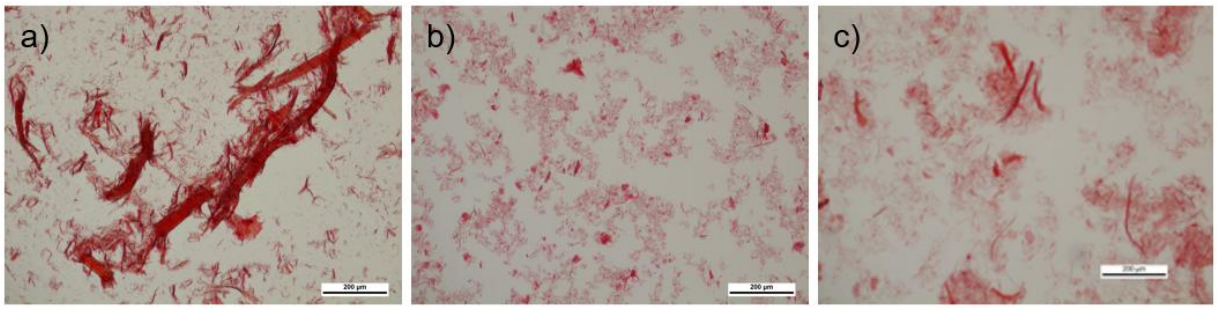

FIGURE 1: Microscope images of the two HC MFC grades, a) standard (coarse) HC MFC and b) microfluidized (fine) HC MFC, as well as c) commercial MFC reference at 10x magnifications.

Before the rheological measurements, the MFC suspensions were diluted to the given fiber consistency with deionized water and homogenized with different mixing procedures depending on the fiber consistency. The suspensions prepared from the two grades of HC MFC, namely a coarse standard grade and a fine fluidized grade, were homogenized using either syringe-to-syringe method or a Silverson mixer and commercially available MFC were homogenized with a Netzsch Shearmaster. The mixing vessel had a volume of approximately 600 mL and an inner diameter of 67 mm. Mixing was carried out at 800–1000 rpm for 15–20 minutes.

Fiber foams were prepared from both grades of HC MFC and from the commercial grade MFC. Prior to foaming, the materials were diluted to the desired working consistencies with deionised water. The coarse HC MFC suspensions were prepared at three different consistencies: 2.5, 5.0 and 7.5%, whereas the fine HC MFC and commercially available MFC reference suspensions were adjusted to 2.5%. Carboxymethyl cellulose (CMC; FinnFix 4000G) was incorporated at 3.5 m.% (based on dry fiber content). The diluted samples containing the CMC were activated using Silverson mixer at 4000 rpm for 5 minutes.

Sodium dodecyl sulfate (SDS) was added to all samples at a concentration of 0.4 g L^{-1}. For the commercially available MFC reference a higher SDS dosage of 0.8 g L^{-1} was required to reach the air content of around 70 ± 5%. Foaming was performed by mechanical mixing (Netzsch Shearmaster) using a high shear sawtooth impeller. Duration of mixing was 10-15 minutes at 2850-4000 rpm with a starting sample volume of 100 ml. The process parameters (mixing speed and time) were adjusted depending on the sample grade to obtain a target air content of 70 ± 5%. The resulting fiber foams were used directly for subsequent characterization.

It is worth noting that the mixing/homogenization procedure is likely to affect the structure and dispersion state of fiber suspensions, as well as the bubble size distribution in fiber foams. Therefore, the rheological properties of the investigated samples may vary depending on the mixing/homogenization method.

Rheological measurements were performed using a stress-controlled Discovery HR-2 rheometer (TA Instruments) with a wide-gap vane-in-cup geometry at 22°C, controlled by a Peltier system connected to a Julabo AWC 100 bath. A 3D-printed serrated cup was used to minimize wall slip at the wall of the cup.[14] The vane had a diameter of 15 mm and the cup diameter was 30 mm. This configuration minimizes wall slip and confinement effects[15], allowing samples with macroscopic fibers to be measured reliably. In the case of fiber foams, the vane geometry can be inserted into the sample without compressing it and therefore without altering its air content or bubble size distribution. An open-ended syringe was used to carefully transfer foam samples from the foaming container to the rheometer cup, ensuring that the foam samples were neither compressed nor there were air pockets created inside the sample.

Frequency sweep measurements for fiber suspension samples were performed at angular frequencies ranging from 0.1 to 100 rad/s at a strain amplitude of 0.1 %. In the amplitude sweep measurements, the strain amplitude was varied from 0.01 to 1000 % in the case of fiber suspension samples and from 0.01 to 100 % in the case of fiber foam samples, while the angular frequency was 3 or 10 rad/s. Shear rate sweep measurements were performed for fiber suspension samples first at increasing shear rate (from 0.001 to 100 s^{-1}), and then at decreasing shear rate (from 100 to 0.001 s^{-1}). Only data measured at decreasing shear rate are reported herein. All rheological data were obtained from the TRIOS software (TA Instruments) that employs the so-called “Couette analogy” in the calculation of rheological properties when a wide-gap vane-in-cup geometry is used, as described in Vadillo et al.[16]

RESULTS

MFC fiber suspensions

Figures 2a and **2b** present the results of frequency sweep and amplitude sweep measurements for the coarse HC MFC grade. The rheological behavior of HC MFC suspensions exhibit pronounced viscoelastic, gel-like characteristics that are strongly dependent on fiber consistency. Frequency sweep measurements show that HC MFC suspensions are highly elastic ($G' > G''$), while both storage and loss modulus showed little dependence on frequency within

the studied range as shown in **Fig. 2a**. In the amplitude sweep measurements, all suspensions show a well-defined linear viscoelastic region (LVER), within which both the storage modulus (G') and loss modulus (G'') remain relatively constant, indicating an intact fibrillar network. The limit for the LVER is observed to be around 0.1-0.5 % depending on the fiber consistency, and the crossover between G' and G'' (commonly known as the flow point) is observed at strain amplitudes of ~35-50 %. Above this point, the material behavior becomes predominantly liquid-like. Both G' and G'' decrease monotonously with increasing strain amplitude, demonstrating Type I LAOS behavior as classified by Hyun *et al.*[17]

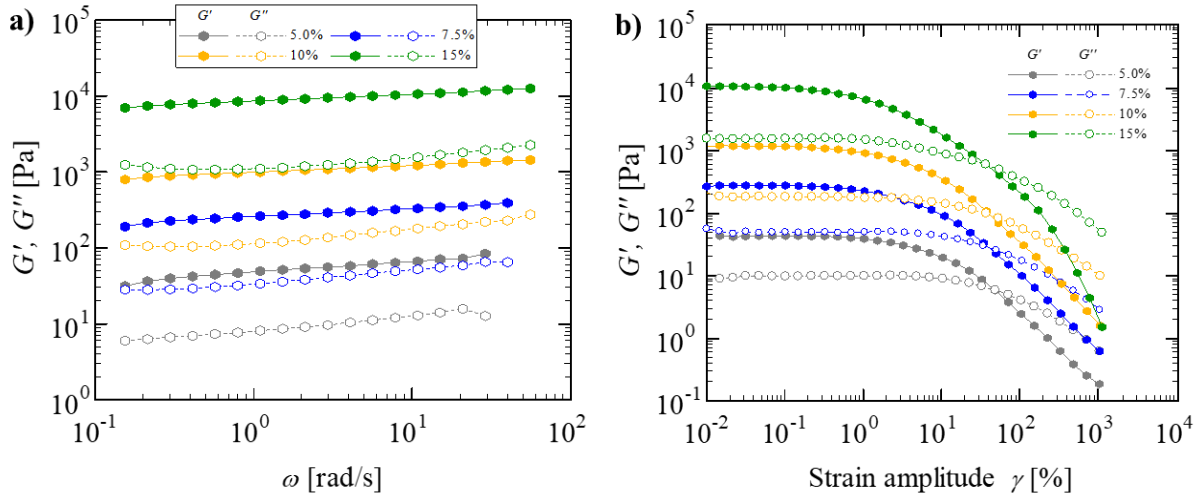

FIGURE 2: Storage modulus and loss modulus for coarse HC MFC grade a) as a function of angular frequency and b) as a function of strain amplitude. The amplitude sweep measurements were performed at an angular frequency of 10 rad/s.

Fig. 3a and **Fig. 3b** present the results of amplitude sweep and shear rate sweep measurements for the coarse and fine HC MFC grades, together with the commercial MFC reference at 2.5% fiber consistency. At the same fiber consistency, clear differences are observed between the samples. The commercial MFC exhibits the highest storage and loss moduli, indicating the formation of a comparatively stronger and more rigid fibrillar network at the same fiber consistency. In contrast, both HC MFC grades show lower moduli, reflecting a less densely connected structure. The fine HC MFC grade consistently shows higher G' and G'' compared to the coarse grade.

The shear viscosity results in **Fig. 3b** show that all suspensions exhibit strong shear-thinning behavior, with viscosity decreasing continuously with increasing shear rate. At the same fiber consistency (2.5%), both HC MFC grades exhibit significantly lower viscosity than the commercial MFC over the studied shear rate range. For example, at a shear rate of 10 s^{-1}, the viscosity of the commercial MFC is about one order of magnitude higher than that of the fine HC MFC grade and about two orders of magnitude higher than that of the coarse HC MFC grade. Overall, the results demonstrate that HC MFC produced by mechano-enzymatic fibrillation provides reduced flow resistance over the commercial MFC produced entirely by mechanical fibrillation, enabling easier handling and more efficient processing.

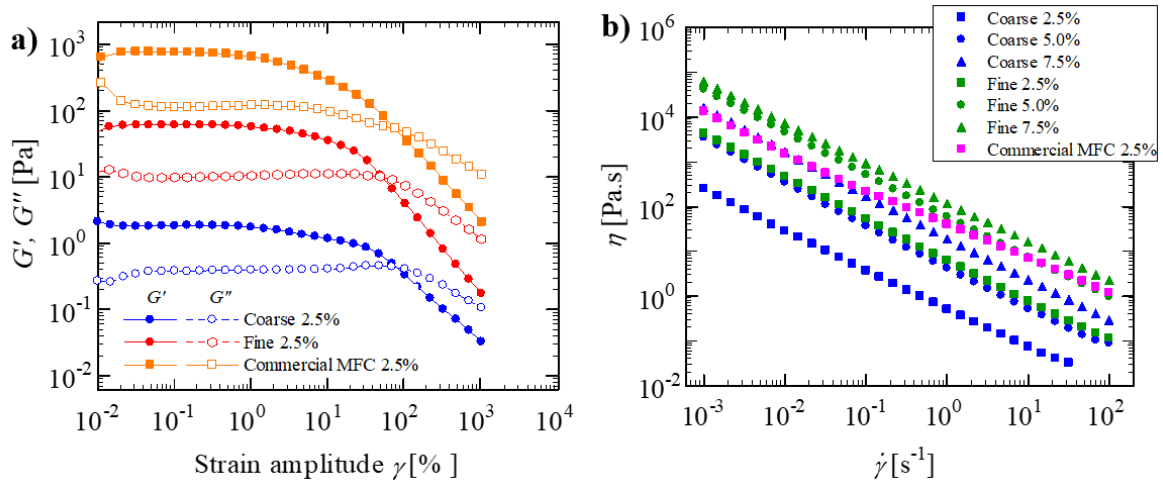

FIGURE 3: a) Storage and loss modulus as a function of strain amplitude for the coarse HC MFC, fine HC MFC, and commercial MFC suspensions. The amplitude sweep measurements were performed at an angular frequency of 3 rad/s. b) Viscosity as a function of shear rate for the three different MFC suspensions.

MFC fiber foams

Following the rheological characterization of HC MFC fiber suspensions, the analysis was extended to fiber foams prepared from the same HC MFC materials. For the fiber foams, CMC was added to improve dispersion and foam stability while reducing granule formation during mixing.

It is important to note that the rheological behavior of fiber foams can differ significantly from that of suspensions. Compared to suspensions, fiber foams contain less free water, which restricts fiber mobility and promotes inter-fiber contacts within the network. Furthermore, the presence of air bubbles alters the network structure and connectivity, effectively increasing the solid volume fraction and influencing the rheological response of the system.[13, 18, 19] These structural differences are expected to influence the viscoelastic and flow behavior of the materials.

Fiber foams represent a multiparameter system, in which not only the fiber properties but also the air content plays a critical role. It is well established that even small variations in air content can significantly influence rheological properties, and therefore careful control and reporting of air content is essential when comparing different samples.[20]

To the best of the authors' knowledge, this study presents the first investigation of high-consistency mechano-enzymatically fibrillated cellulose HC MFC fiber foams and their rheological behavior.

The corresponding air contents of the coarse HC MFC foams were 72.9% at 2.5% consistency, 73.1% at 5.0% consistency, and 64.1% at 7.5% consistency.

In **Fig. 4**, the amplitude sweep measurements revealed that the studied systems exhibit a predominantly elastic response at small deformations, as indicated by the storage modulus (G') values exceeding the loss modulus (G'') for all consistencies. With increasing strain amplitude, a transition from solid-like to liquid-like behavior was observed, marked by G'' surpassing G' at larger deformations. Similarly to the HC MFC suspensions, Type I LAOS behavior is observed at the lowest fiber consistency of 2.5%. However, at higher fiber consistencies of 5.0% and 7.5% Type III LAOS behavior is observed, as the G'' curve shows strain overshoot. At increasing fiber consistency, the fiber network within the foam becomes increasingly dense and hence the number of fiber-fiber contacts increases. These frictional contacts cause an increase

in *G''* values when the fibers start to slide against each other at increasing strain amplitude.[21] Both *G'* and *G"* increased systematically with increasing consistency, reflecting the formation of stronger and more interconnected fiber networks at higher solids contents. In addition, the flow point, defined by the crossover of *G'* and *G"*, shifted to higher strain amplitudes with increasing consistency. This indicates that larger deformations are required to induce flow – i.e. predominantly liquid-like behavior – in more concentrated systems.

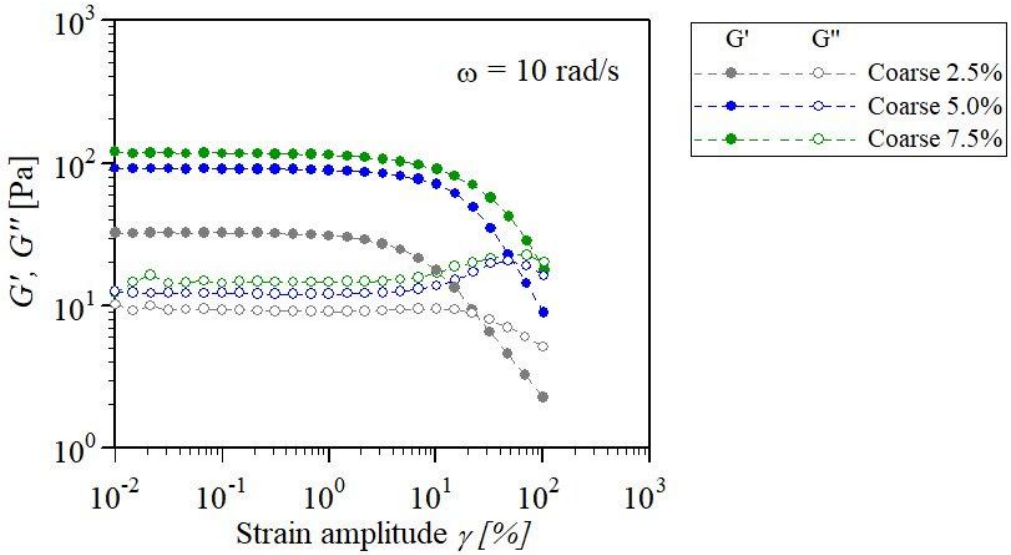

FIGURE 4: Storage and loss modulus as a function of strain amplitude of the coarse grade HC MFC fiber foams at consistencies ranging from 2.5%, 5.0% to 7.5% and air contents of 72.9%, 73.1% and 64.1%, respectively.

Having established the influence of consistency on the rheological behavior of coarse HC MFC fiber foams (**Fig. 4**), the effect of fibrillation degree was further investigated by comparing coarse and fine HC MFC grades, as shown in **Fig. 5**. In addition, the rheological properties were benchmarked against a commercially available MFC reference. The measured air contents were 72.9% for the coarse HC MFC foam, 71.3% for the fine HC MFC foam, and 70.5% for the commercialMFC foam at 2.5% consistency.

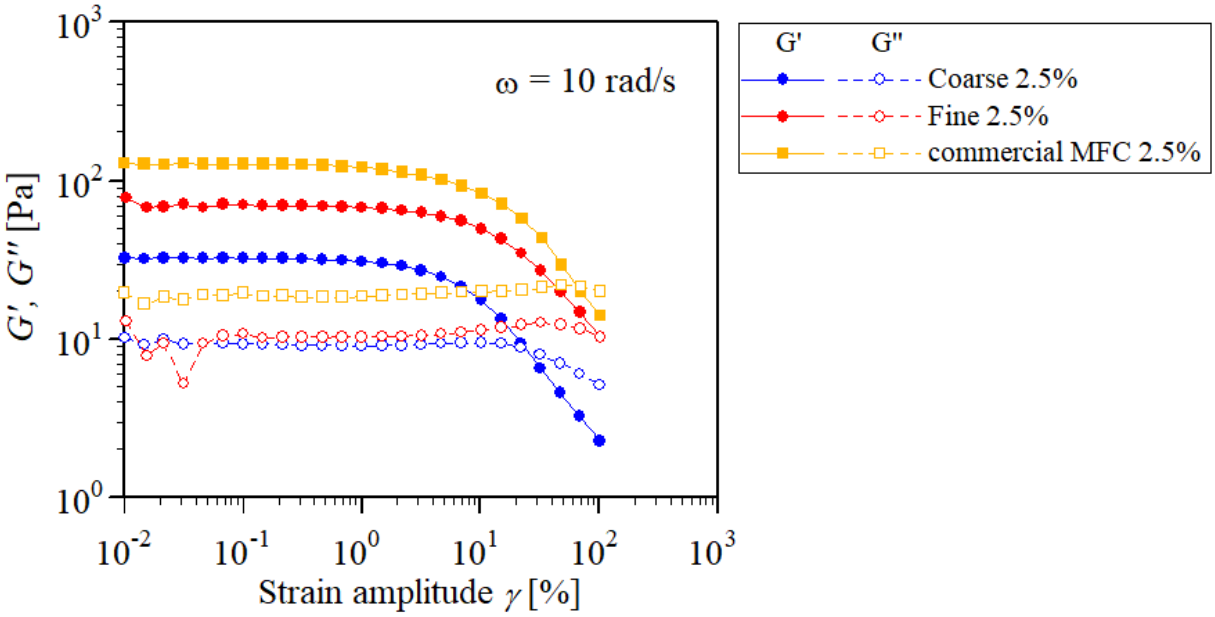

FIGURE 5: Storage and loss modulus as a function of strain amplitude of the coarse and fine grade HC MFC fiber foams, as well as the commercially available MFC reference at consistencies of 2.5% with resulting air contents of 72.9%, 71.3% and 70.5%, respectively.

As shown in **Fig. 5**, the fine HC MFC grade exhibited higher storage (G') and loss (G'') moduli compared to the coarse HC MFC grade, indicating a stronger and more interconnected network structure. Furthermore, the flow point ($G' = G''$) occurred at higher strain amplitudes for the fine grade, demonstrating that larger deformations are required to disrupt the internal structure and induce flow.

In comparison to the commercial MFC reference, HC MFC fiber foams showed lower G' and G'' values at comparable consistencies, indicating a less stiff network. This demonstrates that mechano-enzymatically fibrillated MFC can be used to produce fiber foams with improved handleability and processability. All fiber foams displayed pronounced shear-thinning behavior.

CONCLUSIONS

This study provides the first systematic investigation of the rheological behavior of high-consistency mechano-enzymatically fibrillated cellulose HC MFC fiber foams (previously referred to as HefCel). The results demonstrate that both HC MFC suspensions and foams exhibit characteristic viscoelastic behavior, with a predominantly elastic response at small deformations and a transition to liquid-like behavior at large strain amplitudes.

The rheological properties of HC MFC suspensions and foams were strongly influenced by fiber consistency, with increasing fiber consistency leading to higher storage (G') and loss (G'') moduli. In HC MFC foams, the flow point was shifted to higher strain amplitudes as the fiber concistency increased. This indicates that with increasing fiber consistency a stronger and more interconnected fiber networks forms in HC MFC foams, requiring larger deformations to induce flow. In addition, variations in air content were found to influence the foam structure and therefore the fiber network and should be carefully considered when interpreting rheological data.

The degree of fibrillation further affected the rheological response. The fine HC MFC grade exhibited higher moduli and greater resistance to structural breakdown compared to the coarse grade, reflecting a more developed fibrillar network. When compared to a commercial MFC reference, HC MFC suspensions and foams showed lower stiffness at comparable consistency, although similar qualitative rheological behavior was observed.

Overall, the results highlight that both fiber properties and foam characteristics, such as air content, govern the rheological behavior of HC MFC foams. These findings contribute to the understanding of structure–property relationships in fiber-based foams and indicate improved processability of HC MFC suspensions and foams at high consistencies. Furthermore, the results of this study support the potential of HC MFC as a promising material platform for applications requiring lightweight and porous structures.

ACKNOWLEDGMENTS

This study was conducted in the Business Finland Co-Innovation project RheoMaTe (Rheology for Sustainable Manufacturing Technologies), co-funded by Business Finland, VTT Technical Research Centre of Finland and 14 project partners: ACA Systems Oy, Ambertec Oy, AMT-Systems Oy, Bellmer Finland Oy, EDR & Medeso Oy, Fiberwood Oy, Mirka Oy, Pixact Oy, Spinnova Oyj, Stressfield Oy, Sulzer Pumps Finland Oy, Valmet Technologies Oy, Wetend Technologies Oy, Xpyro Oy. The authors would like to thank Heikki Talja for performing some of the rheological measurements in this study.

REFERENCES

(1) Lähdeniemi, A.; Knuts, A.; Dahl, O. Manufacturing of Microfibrillated Cellulose from Never-Dried Microcrystalline Cellulose Using Masuko Grinder. *BioResources* **2024**, *19*, 9375-9395. DOI: 10.15376/biores.19.4.9375-9395.

(2) Pere, J.; Tammelin, T.; Niemi, P.; Lille, M.; Virtanen, T.; Penttilä, P. A.; Ahvenainen, P.; Grönqvist, S. Production of High Solid Nanocellulose by Enzyme-Aided Fibrillation Coupled with Mild Mechanical Treatment. *ACS Sustainable Chemistry & Engineering* **2020**, *8* (51), 18853-18863. DOI: 10.1021/acssuschemeng.0c05202.

(3) Schenker, M.; Schoelkopf, J.; Gane, P.; Mangin, P. Rheology of microfibrillated cellulose (MFC) suspensions: influence of the degree of fibrillation and residual fibre content on flow and viscoelastic properties. *Cellulose* **2019**, *26* (2), 845-860. DOI: 10.1007/s10570-018-2117-4.

(4) Jaiswal, A. K.; Kumar, V.; Khakalo, A.; Lahtinen, P.; Solin, K.; Pere, J.; Toivakka, M. Rheological behavior of high consistency enzymatically fibrillated cellulose suspensions. *Cellulose* **2021**, *28* (4), 2087-2104. DOI: 10.1007/s10570-021-03688-y.

(5) Tofanica, B.-M.; Mikhailidi, A.; Fortună, M. E.; Rotaru, R.; Ungureanu, O. C.; Ungureanu, E. Cellulose Nanomaterials: Characterization Methods, Isolation Techniques, and Strategies. *Crystals* **2025**, *15* (4), 352.

(6) Missoum, K.; Belgacem, M. N.; Bras, J. Nanofibrillated Cellulose Surface Modification: A Review. *Materials (Basel)* **2013**, *6* (5), 1745-1766. DOI: 10.3390/ma6051745 From NLM.

(7) Sun, Y.; Chu, Y.; Wu, W.; Xiao, H. Nanocellulose-based lightweight porous materials: A review. *Carbohydrate Polymers* **2021**, *255*, 117489. DOI: https://doi.org/10.1016/j.carbpol.2020.117489.

(8) Rahikainen, J.; Mattila, O.; Maloney, T.; Lovikka, V.; Kruus, K.; Suurnäkki, A.; Grönqvist, S. High consistency mechano-enzymatic pretreatment for kraft fibres: effect of treatment consistency on fibre properties. *Cellulose* **2020**, *27* (9), 5311-5322. DOI: 10.1007/s10570-020-03123-8.

(9) Hubbe, M.; Tayeb, P.; Joyce, M.; Tyagi, P.; Kehoe, M.; Dimic-Misic, K.; Pal, L. Rheology of nanocellulose-rich aqueous suspensions: A Review. *BioResources* **2017**, *12*, 9556-9661. DOI: 10.15376/biores.12.4.Hubbe.

(10) Kalyon, D.; Aktas, S. Factors Affecting the Rheology and Processability of Highly Filled Suspensions. *Annual Review of Chemical and Biomolecular Engineering* **2014**, *5*, 229-254. DOI: 10.1146/annurev-chembioeng-060713-040211.
(11) Shin, S. Rheological Design and Applications of Cellulose Nanofiber in Additive Manufacturing. *Journal of Korea TAPPI* **2025**, *57* (4), 19-31. DOI: 10.7584/JKTAPPI.2025.8.57.4.19.
(12) Liukko, S.; Dimic-Misic, K.; Janackovic, A.; Gasik, M. Improving Mechanical and Thermal Properties of Cellulose Foam with Alumina Nanofibers. *Polymers* **2025**, *17* (8), 1043.
(13) Hjelt T, Ketoja JA, Kiiskinen H, Koponen AI, Pääkkönen E. Foam forming of fiber products: a review. *Journal of Dispersion Science and Technology* **2022**, *43* (10), 1462-1497. DOI: 10.1080/01932691.2020.1869035.
(14) Carraretto, I. M.; Owens, C. E.; McKinley, G. H. Time-resolved rheometry of coarsening foams using three-dimensionally printed fractal vanes. *Physics of Fluids* **2022**, *34* (11). DOI: 10.1063/5.0119944.
(15) Mohtaschemi, M.; Dimic-Misic, K.; Puisto, A.; Korhonen, M.; Maloney, T.; Paltakari, J.; Alava, M. J. Rheological characterization of fibrillated cellulose suspensions via bucket vane viscometer. *Cellulose* **2014**, *21* (3), 1305-1312. DOI: 10.1007/s10570-014-0235-1.
(16) Vadillo, D. C.; Owens, C. E.; Perego, A.; McKinley, G. H. Vane rheometry of viscoelastic liquids and yield stress fluids. *Rheologica Acta* **2025**, *64* (6–7), 315–335. https://doi.org/10.1007/s00397-025-01498-8.
(17) Hyun, K.; Kim, S. H.; Ahn, K. H.; Lee, S. J. Large amplitude oscillatory shear as a way to classify the complex fluids. *Journal of Non-Newtonian Fluid Mechanics* **2002**, *107* (1), 51-65. DOI: https://doi.org/10.1016/S0377-0257(02)00141-6.
(18) A. Jäsberg, P. Selenius, A. Koponen, Flow rheology of fibre-laden aqueous foams. *Proceedings of PaperCon 2015*, 872-889.
(19) Jäsberg, A.; Selenius, P.; Koponen, A. Experimental results on the flow rheology of fiber-laden aqueous foams. *Colloids and Surfaces A: Physicochemical and Engineering Aspects* **2015**, *473*, 147-155. DOI: https://doi.org/10.1016/j.colsurfa.2014.11.041.
(20) Prakash, B.; Jäsberg, A.; Koponen, A. Experimental investigation on the effect of fibre consistency on rheology of aqueous foams in pipe flow. *Annual Transactions of the Nordic Society of Rheology* **2021**, *29*, 27-34.
(21) Song, H. Y.; Park, S. Y.; Kim, S.; Youn, H. J.; Hyun, K. Linear and nonlinear oscillatory rheology of chemically pretreated and non-pretreated cellulose nanofiber suspensions. *Carbohydrate Polymers* **2022**, *275*, 118765. DOI: https://doi.org/10.1016/j.carbpol.2021.118765.

Advances in Rheometry

RHEODIALYSIS: A PLATFORM FOR PROBING RHEOLOGY IN EVOLVING CHEMICAL ENVIRONMENTS

Lai Zhang[1], Christopher Graham[1], Shona Marsh[2], Daniel Eriksson[2], Nikil Kapur[3], John Girkin[1] and Anders Aufderhorst-Roberts[4]

[1]Durham University, Durham DH1 3LE, United Kingdom
[2]Netzsch Gerätebau GmbH, Selb, Germany;
[3]University of Leeds, Leeds LS2 9JT, United Kingdom;
[4]University of Liverpool, Liverpool, United Kingdom

DOI: 10.31.265/75124q06

ABSTRACT

Many soft and complex materials exhibit rheological behaviour that evolve spatially in response to changes in their chemical environment, particularly at interfaces. Examples include biopolymer coatings, food products during digestion and personal care products. However, conventional rheological techniques typically operate under static conditions, limiting their ability to capture these coupled time and spatial effects. This presents a significant challenge for understanding processes such as gelation, transport-driven structuring, and interfacial material evolution. Here, we present rheodialysis as an experimental platform that enables in situ rheological measurements under dynamically controlled chemical conditions. The approach integrates a modified rheometer geometry with a membrane-separated flow system, allowing reagents to be introduced non-invasively via diffusion while continuously monitoring rheological properties. This configuration provides precise control over the local chemical environment without disrupting the sample structure. Using alginate hydrogels as a model systems undergoing chemically induced transformations, we demonstrate how rheodialysis can resolve both time-dependent rheological evolution. This work highlights the potential of rheodialysis as a versatile tool for studying soft matter in non-equilibrium conditions. The approach is broadly applicable to systems where external stimuli drive changes in structure and mechanics, offering new opportunities to investigate and optimise processes relevant to formulations, biological systems, and advanced materials.

Introduction

Hydrogels are three dimensional water-swollen networks that are corslsinked through either physical or chemical interactions. The physical properties of hydrogels have long been studied by rheologists and their industrial applications are myriad and growing, from simple applications such as structurants for food and personal applications, to advanced materials applications in tissue engineering, drug delivery, regenerative medicine and biosensing.[1] When manufacturing and using these materials, rheological changes commonly take place at boundaries and interfaces. For example, edible coatings such as meat casings are formed at air-water interfaces during co-extrusion, hydrogel bandages undergo changes in viscoelasticity when exposed to the surface of a wound, and anti-perspirant products undergo gelation-like behaviour when exposed to sweat from the human skin. Clearly, when gelation occurs in these conditions, the rheology of the interface and the rheology of the bulk material are interrelated. Both are sensitive to local changes in chemistry and these changes take place over different timescales that are defined by diffusion and chemical exchange at the surface of the material. This is a physically complex process and its industrial importance, there is a notable lack of

rheological techniques that can probe changes in viscoelasticity under changing chemical stimuli.

Recent rheological research has benefited from a number of novel custom-made platforms which have attempted to bridge this gap in instrumentation. In one study, chemical exchange was induced through a dialysis membrane soaked in an ionic solution that adhered to the lower plate of a parallel plate rheometer, enabling the gelation of the sample to be rheologically probed due to its direct external contact with membrane.[2] While effective at inducing and probing gelation, this approach did not allow for control of chemical release. In another study, this simple membrane was replaced by a hollow cell separated from the sample by a stainless steel mesh, with the chamber volume being continuously replenished using peristaltic pump.[3] This enabled the authors to carry out real time measurements of both gel formation and gel disassembly while the chemical environment was exchanged. More recently, a similar design was reported that involved injecting a crosslinking reagent into a chamber through a two holes on the lower plate using a manual syringe.[4] This enabled the process of gelation to be monitored from the onset of exposure to a crosslinking reagent. Further work by the same authors refined this design by adjusted number and arrangement of these holes to ensure more homogeneous chemical exposure to the sample. As expected, this also appeared to control the mass transfer of ions into the sample, with a larger number of holes leading to faster gelation.[5] In the same study it was reported that gelation process was sensitive to the oscillatory rheology protocol used, which was speculated to arise from induced mixing between the flow chamber and sample. While each of these published designs has it's own individual advantages, they also each have certain drawbacks. There is therefore a lack of a unified platform to enable in-situ chemical exchange for rheometers. In this work, we draw inspiration from these studies to present a new rheology accessory which we term Rheodialysis. Rheodialysis combines what we consider the best features of each of these previously reported approaches, while also incorporating a number of new design features.

Design and Implementation

The design of the Rheodialysis approach are defined by the following goals:

1. In-situ control of chemical environment though automated injection
2. Mechanical isolation of the sample from this chemical environment to minimise external pressure gradients
3. Control of injection rate and contact area to enable mass transfer into the sample to be adjusted.

The design of our device is shown in **Fig. 1(a), (b)**. We use a 20 mm parallel plate configuration with the flow cell taking the place of the lower plate, which is mounted on a Netzsch Kinexus Pro stress-controlled rheometer. The Rheodialysis device comprises a conical flow chamber with a flow inlet at it's base and a flow outlet at it's side. Two rigid plates with 0.16 mm holes are screwed in place on top of the chamber, with a 0.22 μm cellulose membrane between them. This combined assembly essentially replaces the lower plate of the rheometer. Therefore our three goals are addressed through (1) the use of the conical chamber ensures in-situ control, (2) the separation of the chamber using a semi-permeable membrane, and (3) the use of a syringe pump with controllable rate to enable control of the injection rate.

Our method is important that the device does not induce undesirable pressure to the sample between the during chemical exchange. To investigate this, we carried out a simple computational fluid dynamic simulation. **Fig. 1 (c)** shows the modelling of the fluid velocity profiles at an injection speed of 0.1 ml/min with the colour . The result shows that the design enables the inlet to expose the sample to a new chemical environment from below and minimises

the pressure gradient on the sample since the flow is directed parallel to the plate and flow rate (colour bar in **Fig. 1 (c)**) and is lowest at the top of the chamber, directly below the membrane.

Results

We test our device using sodium alginate, a well-studied model gel-forming biopolymer. Alginate is a marine-derived polysaccharide that is widely used in the food,[6] packaging,[7] and biomedical industries.[8] Its crosslinking mechanism arises from its molecular heterogeneity, as it has a block copolymer structure comprising mannuronic acid groups, known as M-blocks, and guluronic acid groups, known as G-blocks as depicted in **Fig. 1 (d)**. When exposed to divalent cations such as calcium, these ions bind to backbone of the negatively charged G-blocks, leading to ionic crosslinking between chains and the formation of a water-swollen hydrogel network.

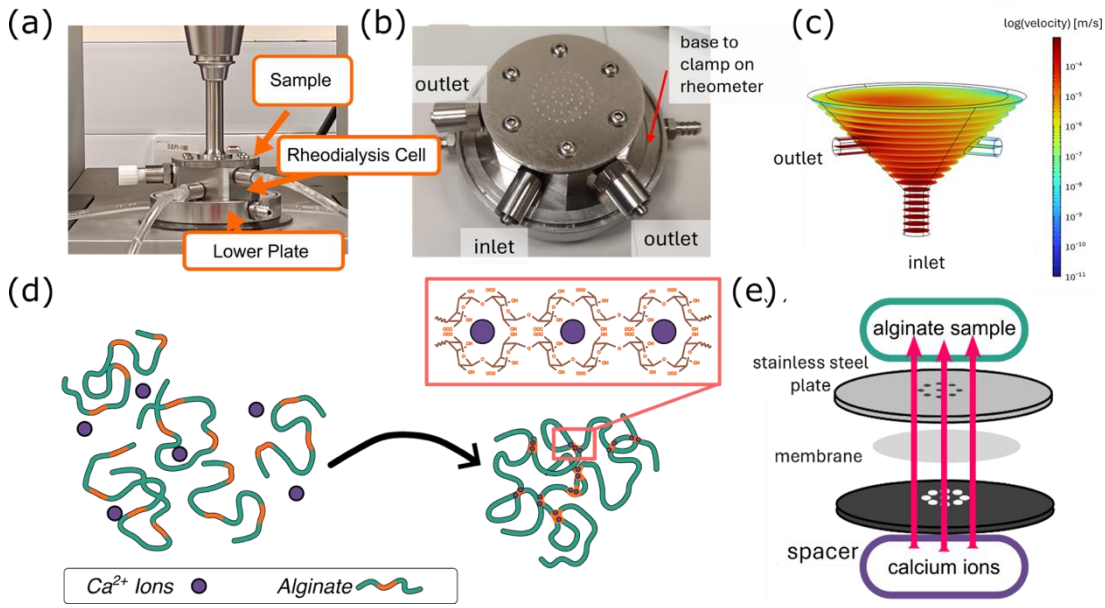

FIGURE 1: The rheodialysis approach comprises a custom-built flow cell that replaces the lower plate of a paralell plate rheometer (a). The flow cell's is separated from the sample through a semipermeable membrane. It's shape is conical with an inlet at the base, and two outlets a larger positions (b). A syringe pump exchanges the sample environment during rheological testing and the geometry ensures that maximum flow rates (c) are reached far from the membrane surface, ensuring minimal pressure gradients on the samples. As a proof-of-concept, we monitor the gelation of alginate, when exposed to calcium ions. The alginate biopolymer backbone consists of two groups: mannuronic acid and guluronic acid. Binding of calcium to the guluronic acid (inset) leads to the formation of a hydrogel network (d) We probe this dynamically by delivering calcium ions to an alginate soluton, through the flow cell.

As a proof-of-concept test, we probed an aqueous sodium alginate sample using the rheodialysis approach, exposing it calcum ions in-situ to induce gelation (**Fig. 1 (e)**). An alginate solution of concentration 5.4 % (w/v) was prepared with Sodium Alginate Protanal 8133 (Dupont, M/G ratio of 65/35, molecular weight 90-180 kDa) and Milli-Q water. The mixture was heated to 80°C and stirred for 30 minutes at 150 rpm to enable complete dissolution and was then cooled to room temperature. The sample was loaded on to the rheodialysis cell and a solution of 0.1 M Calcium Chloride ($CaCl_2$, Thermo Scientific) was injected into the chamber using a syringe pump constructed specially for this work. We explored three separate

injection rates: 0.05 ml/min, 0.1 ml/min, and 0.2 ml/min. The inlet piping was initially purged with the calcium solution carefully, ensuring that the chamber did not fully fill as this would induce gelation. Once complete, the rheometer inertia and torque was calibrated, using a 20 mm parallel plate and the alginate solution was loaded between the plates at a gap separation of 0.5 mm. A 5 rads.s^{-1} pre-shear protocol was then applied to ensure the sample was evenly spread between the plates and injection was initiated.

To monitor the gelation process we carried out a repeated oscillatory measurements across four frequencies 0.2 Hz, 0.4 Hz, 0.8 Hz and 1.6 Hz. This protocol allows observation of the phase angle (δ), elastic modulus (G') and viscous modulus (G") values during the gelation process. It is common to identify the gel point by the point at which G' exceeds G'', however this a crude measure since it invariably depends on the measurement frequency. The true gel point is generally defined through the Winter-Chambon criterion,[9] which posits that G' and G'' both scale with the same power-law relationship in frequency ω. This allows the gel formation time t_g to be accurately quantified through the frequency independence of δ, since, by definition, tanδ = G''/G'.

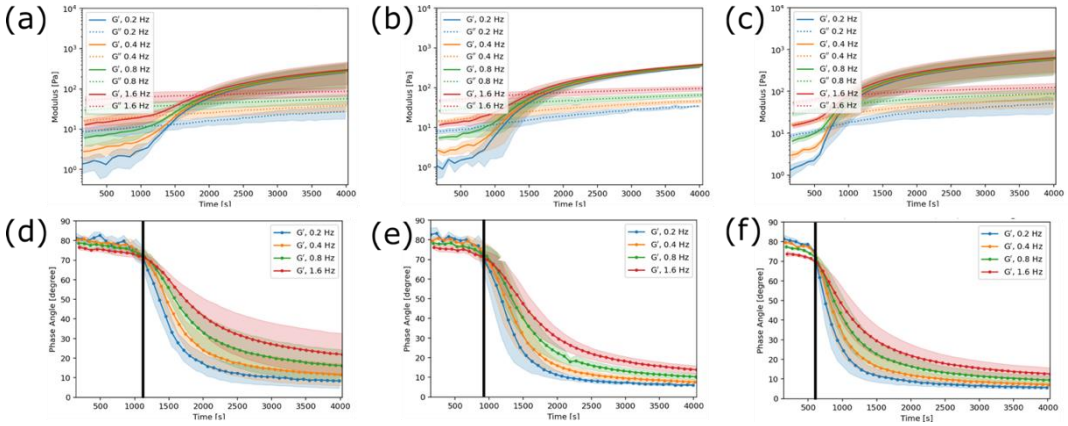

FIGURE 2: Oscillatory shear moduli of alginate samples, resolved over measurement time during in-situ exposure to calcium ions at three different injection speeds: 0.05 ml/min, (a) 0.1 ml/min, (b) and 0.2 ml/min (c). Crossover between storage modulus (solid lines) and loss modulus (dashed lines) is frequency dependent and indicates the approximate onset of gelation. Precise gel points are determined through use of the Winter-Chambon criterion, as the point at which the phase angle is frequency dependent, shown as vertical solid lines (d)-(f). Increasing the injection speed, results in gelation at earlier timescales.

The resulting time-resolved multi-frequency data is shown in **Fig 2 (a), (b)** and **(c)** for each of the three injection rates, respectively. As expected, gelation can clearly be seen to have occurred through the steady increase of G' and G'' over all frequencies. The final values of both metrics show dominance of G', indicating the presence of a soft viscoelastic solid. We interpolate the time-dependent values of δ and define the gel point as as the time of the minimum variance between values of δ collected at the four frequencies. The values of t_g with respect to time at different frequencies are shown in **Fig 2. (a), (b)** and **(c)** for each of the three injection rates, respectively in which the error bars denote the standard deviation from three independent experiments. The measured values of t_g are denoted as vertical bold lines in these plots and are also summarised in **Table 1**.

As shown in **Table 1**, the time taken to gelation is inversely proportional to the injection rate of calcium ions. We postulate that this time dependence arises from two key metrics: **(1)** t_m the rate of mass transfer of calcium ions across the membrane, which is defined by the concentration of calcium ions in the solution and the injection rate and **(2)** the binding rate of

calcium which arises from its association constant K_a and is defined by the alginate molecular structure and charge. Alginate biopolymers differ between sources but are generally known to have a particularly high value of K_a (of order 4×10^3 M^{-1} [10]) which results in fast association of alginate polymers to calcium as they are transported across the membrane during the experiment. The high value of K_a also means that calcium-alginate binding is long lived, which would necessitate the gradual depletion of calcium within the flow cell if there was no flow present. The presence of an injection rate directly determines t_m and acts to replenish these calcium ions in the reservoir. We therefore speculate that the observed sensitivity of the gelation time t_g on injection rate in **Table 1.** This sensitivity suggests that the mass transfer rate and the binding rate in our experiment must be of similar orders of magnitude.

TABLE 1: Calculated values of the gel point using the Winter-Chambon criteron, t_g at three different injection rates. Error bars are standard deviation results from three independent experiments.

Injection Rate (ml/min)	T_g (s)
0.05	1166 ± 80
0.10	972 ± 155
0.20	613 ± 9

Having established that the gelation kinetics can be tuned by injecton rate, we now consider how these kinetics influence hydrogel structure. **Fig. 3 (a)-(c)** show the frequency spectra, at a strain amplitude $\gamma = 0.004$, which are collected once G' and G'' reach a steady state value. To understand the nonlinear rheology of these hydrogels, we also carry out oscillatory amplitude sweeps by logarthimically increasing γ from 0.001 to 1 at a frequency of $\omega = 5$ s^{-1}, shown in **Fig. 3 (d)-(f)**.

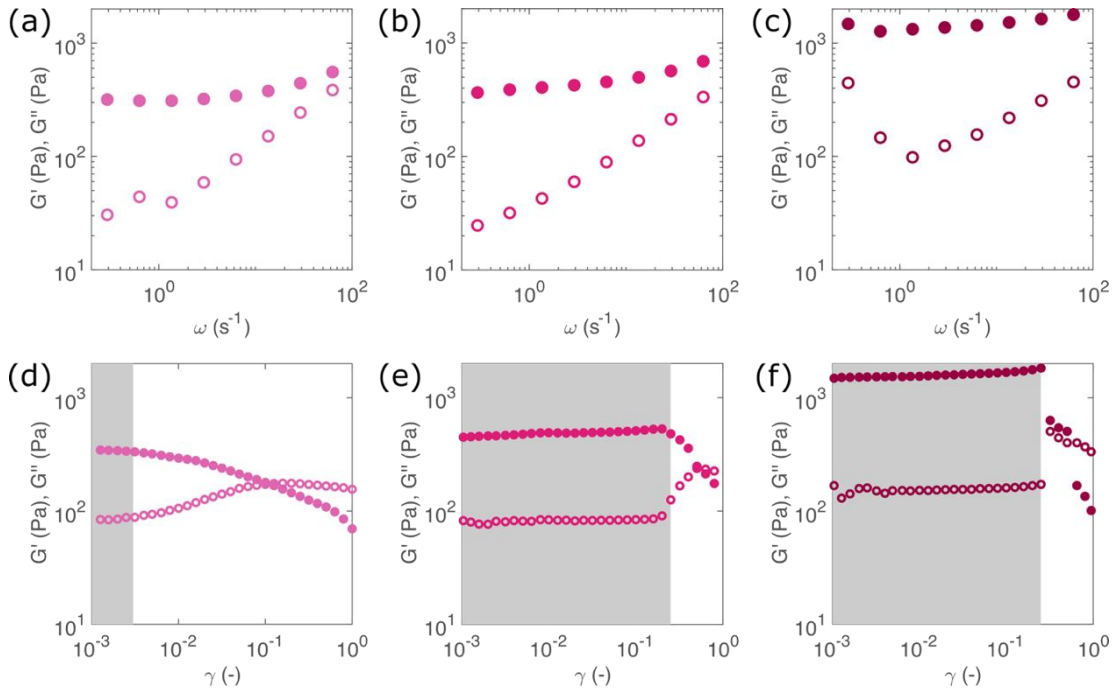

FIGURE 3: Final oscillatory frequency spectra (top) and amplitude sweep data (bottom) for alginate hydrogels formed using the rheodialysis approach. Data is shown for the three different injection speeds: 0.05 ml/min, ((a),(d)) 0.1 ml/min, ((b),(e)) and 0.2 ml/min ((c),(f)). Shaded regions in the lower panels indicate the linear viscoelastic regimes, where the apparent G' and G'' are strictly defined. Faster injection speeds are shown to result in higher values of G' and G'', with more extended linear viscoelastic regimes.

All three hydrogels show frequency spectra that are approximately level across the frequency range measured, which is a definitive characteristic of crosslinked hydrogels. Furthermore, the fastest injection rates appear to lead to hydrogels with significantly higher elastic moduli. The value of G'~ 300 Pa at 0.05 ml/min, while at 0.2 ml/min G'~ 1300 Pa. Similarly the amplitude sweep data show that, as the injection speed is increased, the hydrogels exhibit a more extended linear viscoelastic regime. Within the nonlinear viscoelastic regime, the yielding process of the hydrogels (intepreted as a decrease in the apparent values of G' and G'') has a distinctly different character. At the lowest injection speeds, (**Fig. 3 (d))** there is a gradual decrease in G' and gradual overshoot in G''. At the highest injection speeds, the opposite is observed: G' decreases sharply and G'' similarly overshoots abruptly at the onset of nonlinearity. While deeper analysis of this data is beyond the scope of this work, the observed trent in **Fig. 3 (d)-(f)** is characteristic of a transition between ductile yielding and brittle yielding, suggesting that the different gelation kinetics between the three samples result in hydrogels with distinctly different structures.

Conclusions

In summary, we have developed a simple experimental approach that enables the in-situ control of chemical environment during rheological testing for any viscoelastic material. Although our device stands on the shoulders of other devices reported previously, we have also introduced a number of novel innovations that we believe will broaden the applicability of this approach to other applications. Firstly, the use of a conical flow cell moves the point of injection into the flow cell from the sample surface and thereby minimises the possibility of any pressure graidents. Secondly, by separating the flow chamber from the sample through a semi-permeable membrane, we mechanically isolate the process of chemical exchange from the sample which also minimises the potential of pressure from injection from disrupting the sample. Finally, our Rheodialysis approach allows reaction kinetics to be controlled by adjusting the flow rate. Using alginate that is crosslinked in-situ by calcium chloride as model system, we have shown that the gelation time t_g, defined precisely through the Winter-Chambon criterion can be controlled through adjusting the injection rate. We rationalise this by considering the interplay between the injection rate and binding rate of calcium and postulate that the sensitivity of gelation kinetics to the former suggests that the two rates must be of similar order of magnitude. Intrigingly, the resulting hydrogels appear to have distinctly different rheological properties, both in the linear regime and in the nonlinear regime. This has clear implications for any industrial or biological application in which hydrogel crosslinking occurs at an interfaces, which includes wound healing, coatings, blood clotting and food products.

There are number of considerations regarding the Rheodialysis approach that remain inexplored in this work. More detailed complex fluid dynamics analysis of the binding of alginate and calcium with the hydrogel will allow us to better understand the structural changes that take place during gelation. Similarly, it is likely that the results presented in this work will be sensitive to the gap separation of the plates since our flow cell is incorporated into the lower plate. Finally, more detailed analysis of the nonlinear rheological response will enable us to better appreciate the structural changes

Our view is that there a wide diversity of potential applications for the Rheodialysis approach. Our approach could, for example be used to inform end-use industrial processes that involve rheological changes under shear, for example the topical application of creams and lotions, digestion of food products and rapidly dilution of detergents and cosmetics. Each of these applications have a co-dependence between shear and chemical exchange, which remain relatively unexplored and could be addressed using the approaches and principles set out here.

Bibliography

1. Van Vlierberghe, S.; Dubruel, P.; Schacht, E. Biopolymer-Based Hydrogels as Scaffolds for Tissue Engineering Applications: A Review. Biomacromolecules 2011, 12 (5), 1387–1408.
2. Mahdi, M.; Diryak, R.; Kontogiorgos, V.; Morris, G.; Smith, A. M. In Situ Rheological Measurements of the External Gelation of Alginate. *Food Hydrocolloids* **2016**, *55*, 77–80.
3. Besiri, I. N.; Goudoulas, T. B.; Germann, N. Custom-Made Rheological Setup for in Situ Real-Time Fast Alginate-Ca2+ Gelation. Carbohydrate Polymers, 2020, 246, 116615. https://doi.org/10.1016/j.carbpol.2020.116615.
4. Besiri, I. N.; Goudoulas, T. B.; Germann, N. Custom-Made Rheological Setup for in Situ Real-Time Fast Alginate-Ca2+ Gelation. Carbohydrate Polymers, 2020, 246, 116615. https://doi.org/10.1016/j.carbpol.2020.116615.
5. Besiri, I. N.; Goudoulas, T. B.; Fattahi, E.; Becker, T. In Situ Evaluation of alginate-Ca2+ Gelation Kinetics. J of Applied Polymer Sci, 2023, 140 (32). https://doi.org/10.1002/app.54252.
6. Qin, Y.; Jiang, J.; Zhao, L.; Zhang, J.; Wang, F. Applications of Alginate as a Functional Food Ingredient. Biopolymers for Food Design, 2018, 409–429. https://doi.org/10.1016/b978-0-12-811449-0.00013-x.
7. Metha, C.; Pawar, S.; Suvarna, V. Recent Advancements in Alginate-Based Films for Active Food Packaging Applications. Sustainable Food Technol., 2024, 2 (5), 1246–1265. https://doi.org/10.1039/d3fb00216k.
8. Gheorghita Puscaselu, R.; Lobiuc, A.; Dimian, M.; Covasa, M. Alginate: From Food Industry to Biomedical Applications and Management of Metabolic Disorders. Polymers, 2020, 12 (10), 2417. https://doi.org/10.3390/polym12102417.
9. Chambon, F.; Winter, H. H. Linear Viscoelasticity at the Gel Point of a Crosslinking PDMS with Imbalanced Stoichiometry. Journal of Rheology, 1987, 31 (8), 683–697. https://doi.org/10.1122/1.549955.
10. Wang, X.; Garth Spencer, H. Calcium Alginate Gels: Formation and Stability in the Presence of an Inert Electrolyte. Polymer, 1998, 39 (13), 2759–2764. https://doi.org/10.1016/s0032-3861(97)00597-1.

The Effect of Pre-Shear Protocol for a Thixotropic Fluid

Tale Egeberg Aasland[1], Hans-Joakim Skadsem[1]

[1]Department of Energy and Petroleum Technology, University of Stavanger, Norway

DOI: 10.31265/epsh6425

ABSTRACT

Recent studies have proposed pre-shear protocols that aim to negate directional bias and improve repeatability using a reset step: a short duration rotation in the opposite direction of the final step in the pre-shear. This should leave the sample in a directionally unbiased state, with little or no residual stress. Using a highly thixotropic fluid, we have tested four different pre-shear protocols: one-directional rotation, rotation with reset as suggested by Choi and Rogers (2020)[1], large-amplitude oscillations with reset proposed by Donley et al. (2026)[2] and a synthesis of the two latter. For the present material, a low-concentration aqueous solution of Laponite®-RD, our results do not indicate that either one of these protocols is better suited than the others, nor, in fact, that they perform better than using no pre-shear protocol at all.

INTRODUCTION

In rheology, a wide variety of pre-shear protocols are employed with the purpose of erasing the shear history of the sample and ensure repeatability of the measurements. Traditionally, one-directional rotational shear has been used, but several studies have raised concerns that this may leave the material in a directionally biased state due to residual stress[3–5]. Some studies have replaced rotation with large-amplitude oscillatory shear (LAOS) in an effort to reduce structural anisotropy[6–9], though, in their recent study[1], Choi and Rogers point out that even this approach does not guarantee the removal of recoverable strain. Instead, they suggested a new rotational pre-shear protocol with an additional step: a short duration rotation in the opposite direction of the final step in the pre-shear. The strain imposed by this step should be equal to the recoverable strain in order to erase the shear history imposed by the pre-shear itself. A very recent study has proposed a variation on this protocol using LAOS instead of rotational pre-shear[2].

In the present study we investigate the effect these new pre-shear protocols, called 'reset' protocols henceforth, have on rheological measurements of a thixotropic yield-stress material, and compare the results with conventional rotational pre-shear. Our aim is practical, and we focus on the effect of pre-shear on typical measurements, namely flow curves and steady state shear tests.

EXPERIMENTAL METHODS

Fluid preparation

The model fluid was an aqueous solution of Laponite®-RD (LAP-RD) of concentration 1.5 wt%, in tap water. LAP-RD is a synthetic magnesium silicate clay, made of disk-shaped particles with an approximate length of $\sim$ 30 nm, and a height of $\sim$ 1 nm. For ionic strengths above 10^{-3} M, and concentrations below $\sim$ 4 wt%, aqueous solutions of LAP-RD form a gel structure when left idle[10].

LAP-RD powder provided by BYK was used in this study. The solution was mixed for 20 minutes using a three-bladed ducted propeller. A 1 wt% solution of NaCl was added subsequently, to a concentration of 0.035M. A batch of 1000 g was made and stored in separate containers of size 50 ml. Samples used in the present study were left idle at room temperature for 5 - 8 weeks before measurements.

Measurement methodology

The tests were carried out using an Anton Paar MCR-702e rheometer, with a parallel plate configuration. The plate diameter was 50 mm, with a gap of 1 mm. The top plate was serrated, in order to avoid wall slip. All tests were carried out at a temperature of 20 °C.

The tested pre-shear protocols are outlined in the following:

i) Conventional: Rotational shear followed by structural recovery

ii) Rotation - reset: Rotational shear directly followed by a reset step, and structural recovery, as proposed by Choi and Rogers[1]

iii) LAOS - relax - reset: LAOS followed by a relaxation interval, a subsequent reset step, and a final relaxation interval, as proposed by Donely et. al.[2],

iv) LAOS-reset: LAOS directly followed by a reset step and structural recovery

The last protocol is suggested by the present authors, to bridge the gap between protocols ii) and iii). The relaxation interval between pre-shear and the reset step was an addition suggested by Donley et al.[2]. Choi and Rogers[1], however, stress the importance of running the reset step directly after pre-shear, in order to avoid structural recovery in a biased state. For this reason, we run tests for both cases: LAOS with direct reset and LAOS with a relaxation interval before the reset step. In the LAOS-relax-reset protocol, the final relaxation occurs under small-amplitude oscillations (SAOS), whereas for the remaining protocols structural recovery occurs at $\tau = 0$.

Prior to starting the measurement campaign, pretests were carried out in order to determine the linear viscoelastic range, and structural recovery time scales. Amplitude sweep and SAOS recovery results are shown in figure 1. From figure 1a, we see that $\gamma = 1$ % is within the linear viscoelastic range, whereas $\gamma = 10$ % is clearly in the non-linear region, though far away from the flow point (.i.e. the cross-over between the storage modulus G' and the loss modulus G''). Thus, these values are suitable for SAOS and LAOS, respectively.

The recovery test was carried out at s strain amplitude of $\gamma = 1$ % and a frequency of $\omega = 10$ rad/s. LAP-RD is highly shear-thinning at low concentrations, and exhibits long structural recovery times after shear, seen in figure 1b. Initially, recovery occurs over a

short time scale, then the growth rate of G' decreases. From practical considerations, the duration of the recovery interval was set to 30 minutes, i.e. 1800 s. This is long enough to be well outside the short recovery time scale, although a slow increase of G' continues beyond this point.

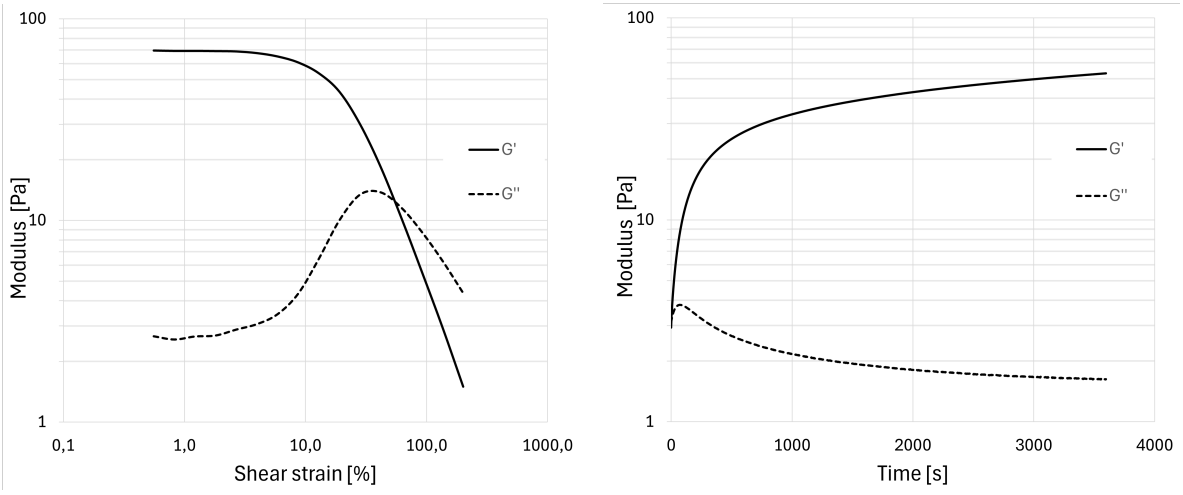

(a) Amplitude sweep.

(b) Structural recovery.

FIGURE 1: Pretests to determine linear viscoelastic range and structural recovery time scale.

The recoverable strain, γ_{rec}, for the rotation-reset protocol was determined by creep tests. This entails that a constant shear stress is applied for a given duration, then the stress is set to zero, while the subsequent development of the strain is monitored. The steady-state value of the strain is taken as γ_{rec}. The rotational part of the rotation-reset protocol applies a shear rate of $\dot{\gamma} = 200$ s^{-1} for 200 s, equal to the conventional protocol, which gives a steady-state stress of $\tau \approx 6.2$ Pa. This value was used as the applied stress in the creep test, and the duration of the applied stress interval was the same as the rotational part of the protocol.

Finding the right values for γ_{rec} was something of a challenge, because the creep tests themselves were not very repeatable, with significant spread for samples taken from the same container during the same day. A representative collection of creep tests is shown in figure 2. Ironically, perhaps, tests may have been more repeatable with a pre-shear protocol in place, but as the object of this study is to consider such protocols, it was not deemed suitable to use one. In lieu of pre-shear, samples were sheared by deploying them slowly (meaning for approximately 15 s) to the bottom plate with a syringe. This ensured an equal sample volume (3 ml) for every repetition, if not completely equal deployment shear rate. After being placed, the sample rested for 60 minutes before the creep test started.

The rheometer used in this study can be run as both stress-controlled and strain-controlled. In order to be consistent with the method of Donley et al.[2], whose rheometer was strain-controlled, an oscillating strain is used for the LAOS protocols. This entails that γ_{rec} must be estimated from the residual stress, or determined by trial and error, that is, finding a shear rate interval that gives zero, or near-zero, residual stress after pre-shear. We have attempted to estimate the γ_{rec} using

$$\gamma_{rec} = c_g \frac{\tau_{res}}{G'_l} \frac{(G'_l + G''_l)}{G'_l}, \tag{1}$$

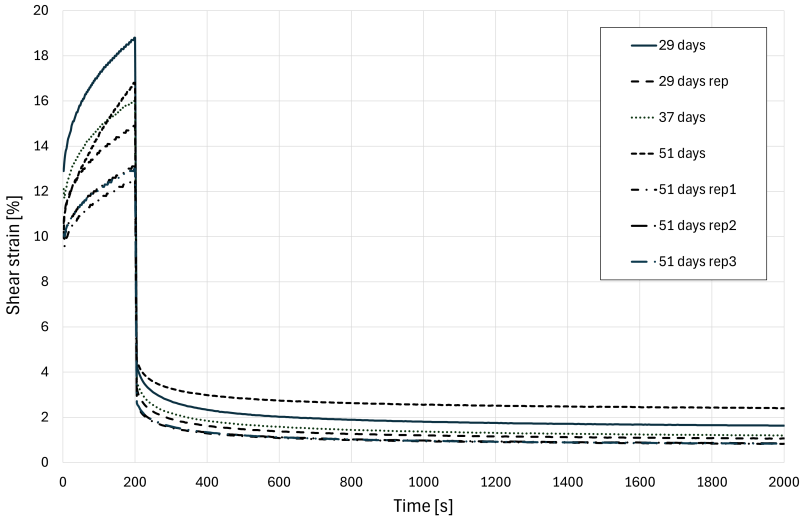

FIGURE 2: Creep tests at different sample idle times.

	$\dot{\gamma}_1$ 1/s	γ_1 %	ω_1 rad/s	t_1 s	t_2 s	$\dot{\gamma}_3$ 1/s	t_3 s	γ_4 %	ω_4 rad/s	t_4 s
Conventional	200			200					1800	
Rotation-reset	200			200		-12	0.1			1800
LAOS-relax-reset		10	1	64	60	-0.0075	0.01	-7.5×10^{-5}	10	60
LAOS-reset		10	1	64		-0.4	0.1			1800

Table 1: Pre-shear protocol variables

where τ_{res} is the residual stress, c_g is a geometry dependent correction factor, and G_l' and G_l'' are the storage and loss moduli within the linear viscoelastic range[2]. For parallel plates, $c_g = \pi/\sqrt{2} \approx 2.22$.

In practice, the residual stresses in the material are very low, and there is a slight variation for each realization. This makes it difficult to find an accurate value of γ_{rec} either by estimation or trial and error. If τ_{res} is taken as the value directly after the LAOS interval, this typically gives $\gamma_{rec} \approx 0.04$, whereas the value when a 60 s relaxation interval is allowed, is $\gamma_{rec} \approx 7.5 \times 10^{-5}$.

The pre-shear variables as summarized in Table 1. Here, subscript 1, 2 and 3 refer to the initial shear interval, the relaxation interval, and the reset step, respectively. 4 refers to the structural recover or final relaxation interval. t denotes interval duration.

Because LAP-RD undergoes physical aging due to dissociation of sodium ions[11], timing of the test schedule is important. For results to be comparable, the tests cannot be very far apart in time, otherwise the storage modulus of the material will have increased beyond repeatability. Therefore, all steady shear rate tests were carried out within 24 hours for each rotational protocol. Likewise, three repetitions of the flow curve were carried out within 24 hours, per pre-shear type. Despite our sincere efforts, tests cannot be carried out simultaneously. This means a certain degree of physical aging will have occurred between testing one pre-shear protocol and the next. Therefore, the results are not compared directly. Rather, the degree of directional bias and repeatability obtained with each protocol is evaluated. The rotational protocol measurements were carried out first, after an idle time of approximately 5 weeks, while the LAOS-reset and LAOS-relax-reset were

carried out after 7 and 8 weeks of idle time, respectively.

Each test series was carried out with material from the same container, in case small differences in structure arise during idle time. However, the pretests will in some instances have been carried out with material from a different container than the final measurements, which gives rise to some uncertainty.

Finally, each test was carried out with a new sample, in order to avoid drying effects, given the long duration of the structural recovery interval.

RESULTS AND DISCUSSION

Constant shear rate tests

A set of constant shear rate tests were carried out for the rotational pre-shear protocols, in order to check for signs of directional bias in the steady-state values. Three shear rates were tested for both directions, and the results are shown in Figure 3. Agreement between positive and negative directions is generally quite good. For the two lowest shear rates, agreement is best for the conventional protocol, whereas a larger discrepancy is seen for this protocol at a higher shear rate. As such, it is difficult to conclude whether or not these differences are caused by directional bias. In the study of Choir and Rogers[1], directional bias tended to be smoothed out for steady-state conditions, and was primarily visible in the initial transient phase of the measurement.

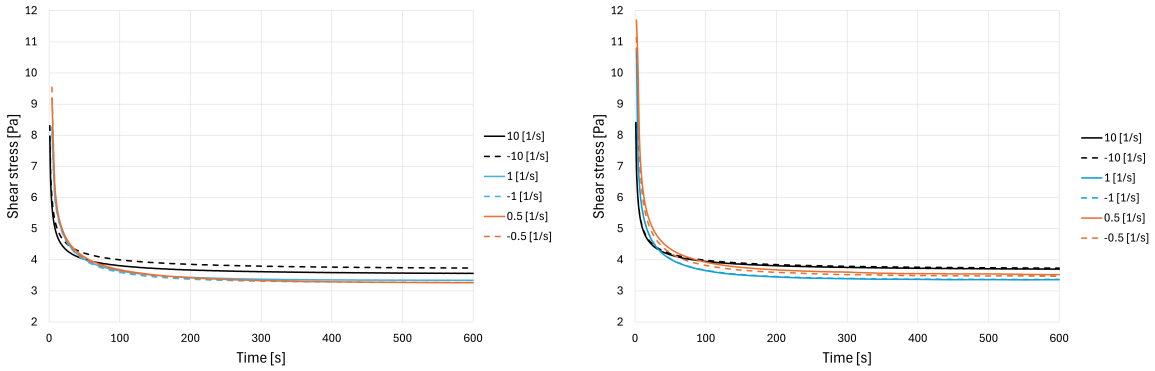

(a) Conventional (b) Rotation-reset

FIGURE 3: Constant shear rate tests for the rotational protocols. Dashed lines represent negative rotational direction during measurement.

Shear rate ramps

Figure 4 shows flow curves generated from logarithmic shear rate ramps. The shear rate was increased stepwise from 0.01 s^{-1} to 200 s^{-1}, and the time per step was decreased from 200 s to 2 s. The curves shown are averaged over three consecutive measurements, and the error bars represent the standard deviation (STD) at each point. In addition to the pre-shear tests, a series with no pre-shear was taken for comparison.

From Figure 4d, we see that for low to intermediate shear rates, LAOS-reset outperforms the other protocols, though the standard deviation increases significantly in the region beyond $\dot{\gamma} \approx 5$ s^{-1}.

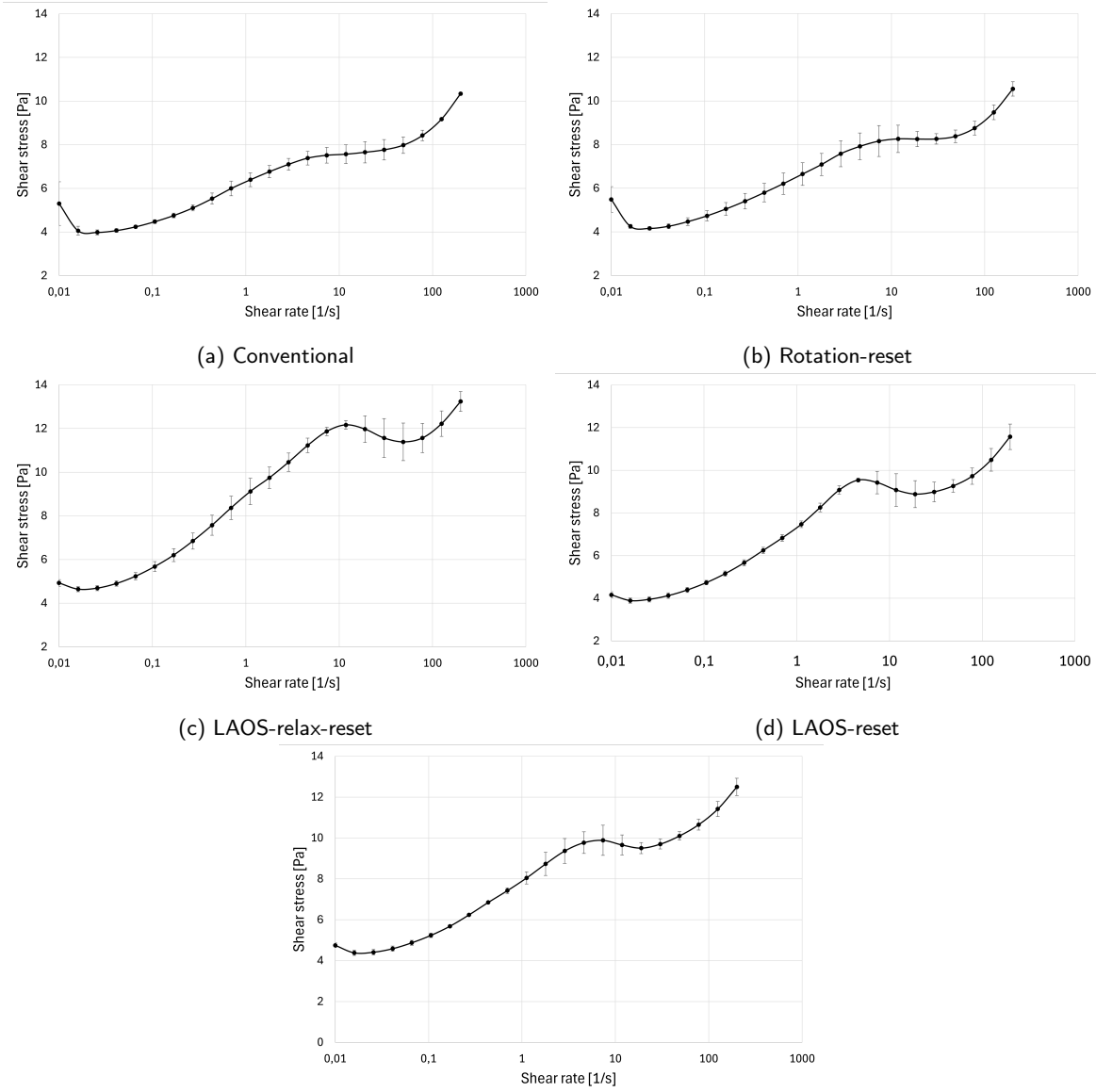

(a) Conventional

(b) Rotation-reset

(c) LAOS-relax-reset

(d) LAOS-reset

(e) No pre-shear

FIGURE 4: Shear rate ramps

The rotation-reset and LAOS-relax-reset protocols exhibit relatively high STD over a large portion of the measurement range, though not necessarily for the same values. Some of this error likely comes from the difficulty of obtaining consistent parameters for recoverable strain. It is quite conceivable that an erroneous value in the reset step may impart additional shear history instead of erasing it, which makes matters worse where repeatability is concerned. When considering the data from each run separately (not shown), we see that residual stress is normally not completely removed by the pre-shear, though the values are typically in the order of 10^{-3} Pa. This means that the material will recover with growing stresses that may influence the measurement. This observation is underlined by the fact that the tests without pre-shear have very good repeatability, in particular in the low shear rate range.

Notably, save the LAOS-relax-reset protocol, low shear rates have the best repeatability in most cases, whereas higher STD values are found for intermediate to high shear rates. This is likely related to the initial process of breaking the microstructure of the material before steady-state conditions are achieved. Several studies have reported shear banding across the measurement gap for various geometries[12–14]

Martin & Hu[14] found that increasing the shear rate may lead to a lower transient stress; the microstructure breaks down faster at higher shear rate, so that the stress overshoot decreases faster than for a low shear rate. It was also pointed out that the stress at $\dot{\gamma} = 10$ s^{-1} took "tens of seconds" to plateau. While the concentration of LAP-RD in that study was 3 wt %, double that of the present study, the results are still comparable. Increasing the solid content of the solution within the gel phase does not alter the overall material structure, though the elastic properties are strengthened.

In Figure 4, all curves display a bump in the vicinity of $\dot{\gamma} \sim 5 - 10$, though the maximum of this bump is not exactly in the same place. Considering the constant shear rate curves in Figure 3, we see that the two lowest shear rates need a longer time to reach steady state conditions. This means that if the measurement time per point is somewhat too low, the reported stress may be higher than the would-be steady state value.

The flow in the gap is a constant competition between structural breakdown and rebuilding[14], and the initial microstructure at the start of a measurement point on the flow curve is in reality a compilation of the shear history from all prior treatment of the material. Shear-banding is very sensitive to the initial microstructure, so variations in the same due to slight variations in the post pre-shear conditions may very well cause a rise in STD. There are noticeable differences between the pre-shear protocols in the shape of the flow curve as well as in the location of STD maxima and minima, which underscores this point.

It should be added here that Donely et al.[2] explicitly suggest their method may not be suitable for aging or very time-dependent materials. Their purpose was to develop a path-independent method, where a set of measurements may be taken on the same sample in any given order, always preceded by pre-shear. We are not able to test this notion, for the sheer time required to run a single measurement step with pre-shear and recovery (and the inevitable drying that would follow). That being said, it seems as though LAOS may be more suitable for this material than rotational pre-shear, albeit with a properly tailored reset step directly after the initial shear.

CONCLUDING REMARKS

In this study, we have evaluated the effect of pre-shear on rheological measurements of a distinctly thixotropic fluid, a low-concentration aqueous solution of Laponite-RD. Four pre-shear protocols were tested, where one was conventional rotational shear, while the others incorporated a so-called reset step, i.e. short-duration shear in the opposite direction, with the purpose of negating the history of the pre-shear itself. Two of the protocols hail from previous studies by Choi and Rogers[1] and Donley et al.[2], while protocol number four was our own synthesis of the two.

Our results indicate that there is little directional bias for the material we have used, and residual stresses after the initial pre-shear protocol are very low. From the flow curves, we cannot conclude with certainty that any of the pre-shear protocol is significantly better than the others, nor, in fact, that they are significantly better than simply refraining from pre-shear. However, a synthesis of the two protocols from the literature, shows promise.

Here, LAOS is used in lieu of rotation, and the reset step is added directly after pre-shear. Refining this method further may be interesting for future work.

Our efforts show that finding the correct shear rate and duration for the reset step can be challenging, and requires that the researcher devote considerable time before starting the main measurements. As such, extensive protocols like those tested herein are perhaps more suited for fundamental research rather than applications.

References

1 Choi, J. and Rogers, S.A. Optimal conditions for pre-shearing thixotropic or aging soft materials. *Rheologica Acta*, 59:921–934, 2020.

2 Donley, G., Martys, N., Del Gado, E., and Snyder, K. Path-independent flow characterization of model yielding pastes. *Rheologica Acta*, 65:341–352, 2026.

3 Rogers, S.A., Callghan, P.T., and Vlassopoulos, D. Time-dependent rheology of colloidal star glasses. *J. Rheology*, 54(1):133–158, 2010.

4 Cloitre, M., Borrega, L., and Leibler, L. Rheological aging and rejuvenation in microgel pastes. *Phys. Rev. Lett.*, 85(22):4819–4822, 2000.

5 Fernandez, R.R., Andrade, D.E.V., and Negrão, C.O.R. Influence of pre-shearing on rheometric measurements of an oil-based drilling fluid. *Rheologica Acta*, 56(9):743–752, 2017.

6 Lee, J.C.W., Weigandt, K.M., Kelley, E.G., and Rogers, S.A. Recovery rheology via rheo - sans: Application to step strains under out-of-equilibrium conditions. *AIChE J.*, September:1–15, 2019.

7 Lee, J.C.W., Porcar, L., and Rogers, S.A. Strucure-property relationships via recovery rheology in viscoelastic materials. *Phys. Rev. Lett.*, 122(24):248003, 2019.

8 Moghimi, E., Jacob, A.R., Koumakis, N., and Petekidis, G. Colloidal gels tuned by oscillatory shear. *Soft Matter*, 13(12):2371–2383, 2017.

9 Moghimi, E., Jacob, A.R., and Petekidis, G. Residual stress in colloidal gels. *Soft Matter*, 13(43): 7824–7833, 2017.

10 Tanaka, H., Meunier, J., and Bonn, D. Nonergodic states of charged colloidal suspensions: Repulsive and attractive glasses and gels. *Physical Rev. E.*, 69:031404, 2004.

11 Shahin, A. and Joshi, Y.M. Physiochemical effects in aging aqueous Laponite suspensions. *Langmuir*, 28:15674–15686, 2012.

12 Pignon, F., Magnin, A., and Piau, J.M. Thixotropic colloidal suspensions and lfow curves with minimum: Identification of flow regimes and rheomtric consequenes. *J. Rheology*, 40(4):573–587, 1996.

13 Pignon, F., Magnin, A., and Piau, J.M. Butterfly light scattering pattern and rheology of a sheared thixotropic clay gel. *Physical Rev. Lett.*, 79(23):4689–4692, 1997.

14 Martin, J.D. and Hu, Y.T. Transient and steady-state shear banding in aging soft glassy materials. *Soft Matter*, 8:6940–6949, 2012.

Poster Presentations

RHEOLOGY OF HIGH-PROTEIN SAUCES

Hanna Svensson[1], Ana Miljkovic[1], Célia Carlier[1] and Mats Stading[1,2]

[1]RISE Research Institutes of Sweden, Gothenburg, Sweden
[2]Chalmers University of Technology, Gothenburg, Sweden

ABSTRACT

As life expectancy continues to rise age-related health issues are becoming increasingly prevalent, placing greater demands on healthcare systems. Adequate intake of energy and protein is critical for maintaining health and preventing frailty in older seniors. Ready-to-eat meals are commonly consumed by this group, particularly those living alone, and offer a practical avenue for nutritional intervention. Enhancing the protein content of these meals, especially through components like sauces, may improve dietary intake without compromising palatability.

An ongoing project aims to develop high-protein, high-energy, ready-to-eat meals tailored to the needs of older seniors. This current study investigated the impact of adding different protein powders (pea, rice, gluten and whey) to a model sauce on its rheological properties. Using viscometry, the results show that protein addition generally increases sauce viscosity, with rice protein being an exception, and modify the initial structure formation on heating. These findings suggest that protein fortification of sauces is feasible, though formulation adjustments may be necessary to achieve desirable sensory and textural characteristics.

INTRODUCTION

With increasing life expectancy – now approximately 20 years longer than fifty years ago[1], age-related health challenges are becoming more prevalent and place growing demands on healthcare systems. Two key determinants of sustained health and quality of life in older adults are adequate nutritional intake and regular physical activity. Inadequate consumption of energy and protein is strongly associated with undernutrition, sarcopenia, frailty, increased hospitalization rates, and elevated mortality risk.

It is a challenge to design and develop good tasting and attractive foods, dense in energy and nutrients, since impact on the food experience itself is crucial. Tastes, flavours and texture change according to addition of nutrients and energy[2]. Ready-to-eat meals are popular among seniors, especially for community-dwelling seniors in single households. Such a meal typically contains 400-700 kcal and 20-30g protein and contains meat, carbohydrates (potato, rice, pasta), vegetables and sauce. For the senior consumers it would be beneficial to increase the protein content which can be done in several ways. More meat could be added but it is by some considered tough to eat, and another way is through the sauce. Sauce has been found beneficial overall for increasing intake of energy and protein for seniors[3]. Addition of protein affects both rheological behaviour and sensory properties.

The aim of the on-going project FRESH is to develop high-protein, high-energy, nutritious ready-to-eat meals to prevent onset of frailty. The objective of the present study was to study addition of protein to a model sauce[4] and how it influences its rheology.

MATERIALS AND METHODS

Materials

Three different protein powders of pea, rice and whey protein were kindly supplied by the food manufacturer Dafgårds (Källby, Sweden). Gluten was supplied by Lantmännen (Lidköping, Sweden). Wheat flour, rapeseed oil and salt were obtained from the local supermarket.

Sample preparation

A basic model recipe of sauce was used where 6g wheat flour, 9g protein powder, 0.2g salt and 6g oil was first mixed. Water (100g) was then added and stirred to a smooth sauce consistency at 60°C. In the reference sauce no extra protein powder was added. The prepared amount corresponded to a typical serving of sauce.

Rheometry

An ARES G2 rheometer (TA Instruments, New Castle, DE, USA) was used for viscometry, equipped with a helical impeller in a 34 mm diameter cup at 37°C, see **Fig. 1a**. Viscometry was monitored using systemic rheology[5]. Viscosity was monitored at a shear rate of 100 s^{-1} during a temperature profile simulating processing, cooling and reheating for consumption as shown in **Fig. 1b**. Heating and cooling rates were set to 2°C/min. A flow curve was obtained after the reheating for shear rates 1-100 s^{-1}. The Power law model, $\sigma=K\dot{\gamma}^n$, was fitted to the flow curves, and the consistency index K and flow behaviour index n was extracted. All measurements were performed in triplicate.

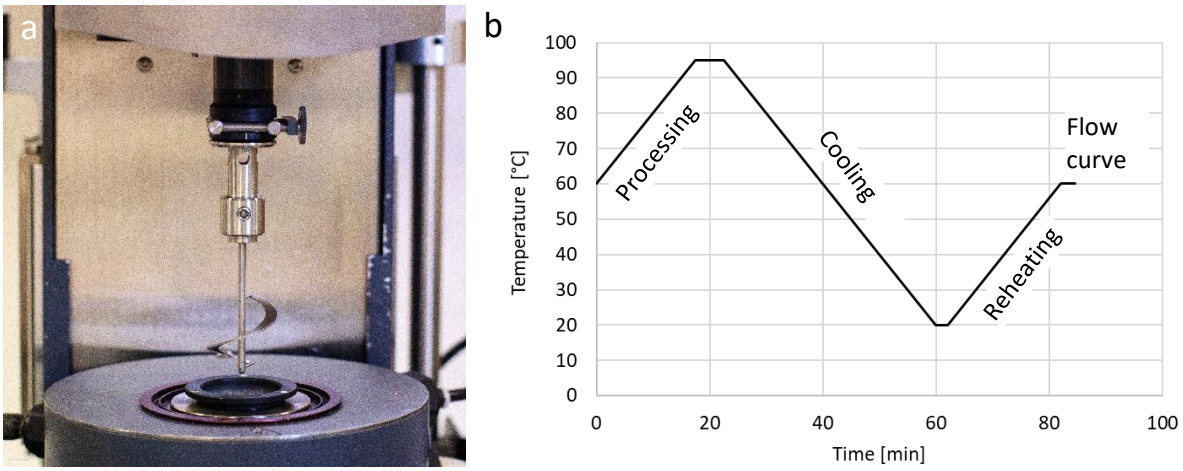

FIGURE 1: Experimental setup. a) Helical impeller system, b) temperature profile

RESULTS AND DISCUSSION

During heating of the ingredients from 60-95°C the starch will gelatinise and protein aggregate. This caused an increase in viscosity as depicted in **Fig. 2**. The reference sauce without added protein had a moderate increase in viscosity at about 85°C mainly caused by gelatinisation of the wheat starch, whereas whey protein caused a strong increase in viscosity starting at 75°C. All sauces showed an initial increase in viscosity going through a peak and then decrease at

higher temperatures. The sauces were continuously sheared at 100 s^{-1} throughout the heating causing the initial aggregates and gelatinised starch granule structure to eventually break, and the viscosity to level out.

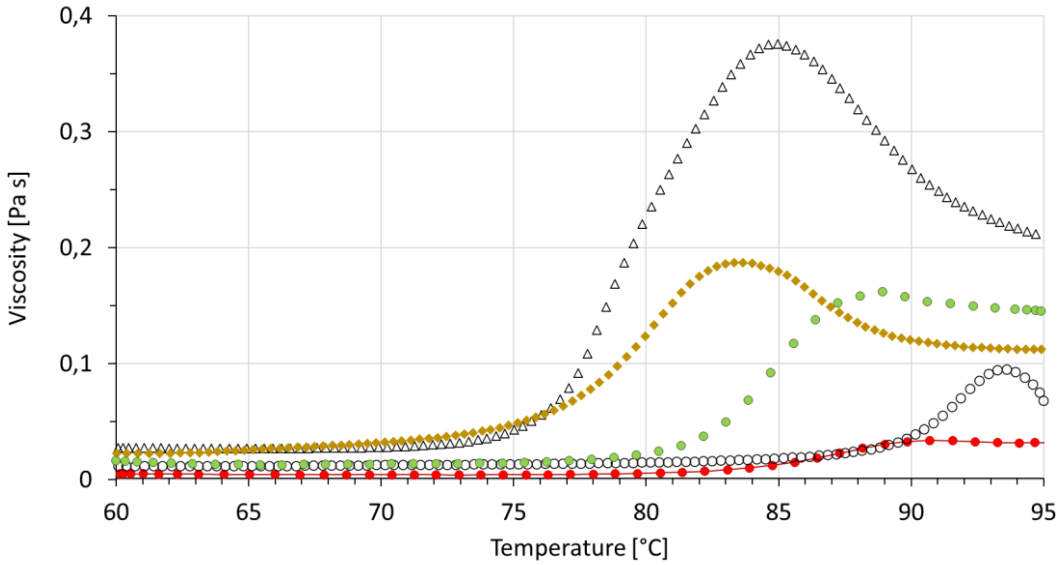

FIGURE 2: Viscosity during processing of sauces (heating and shearing).
● Reference (flour only), ● pea protein, ○ rice protein, ◆ gluten and △ whey protein

After the initial heating, resembling processing (**Fig. 2**), the sauces were cooled and reheated to eating temperature (60°C) where a flow curve was obtained. The Power Law model was fitted to the recorded data, and K and n are presented in **Fig. 3.**

The flow behaviour index n shows the degree of shear thinning where a value close to one indicates Newtonian behaviour (**Fig. 3a**). The n value ranged from 0.4 to 0.7 except for the sauce containing rice protein (0.97). This sample also had a low K value (0.020 Pa s^n) meaning that it had a "thin" texture. After the initial peak for the rice protein sauce in viscosity during processing the structure was broken by the shear flow which resulted in much lower viscosity than for the other sauces.

The consistency K can be considered as the sauce "thickness" as the recorded flow behaviour index n was fairly constant (except for the sauce with added rice protein). **Fig. 3a** shows the consistency index for all sauces. Except for rice protein, all addition of protein resulted in thicker sauces than the reference. It can also be noted that whey protein caused high variability in the measured viscosity between replicates.

CONCLUSIONS

The rather high amount of 9 g added protein to a serving did not significantly alter sauce rheology. The viscosity of the final product at eating temperature increased, but not beyond limits. Processing of the sauce may have to be adjusted as the protein-fortified sauces had significantly higher initial viscosity and onset of the viscosity increasing at lower temperature than the reference sauce.

Rice protein was the exception resulting in a reduced viscosity and a too thin texture. For a commercial product this could be exploited by using a mixture of rice and other proteins to modulate the viscosity towards the desired texture.

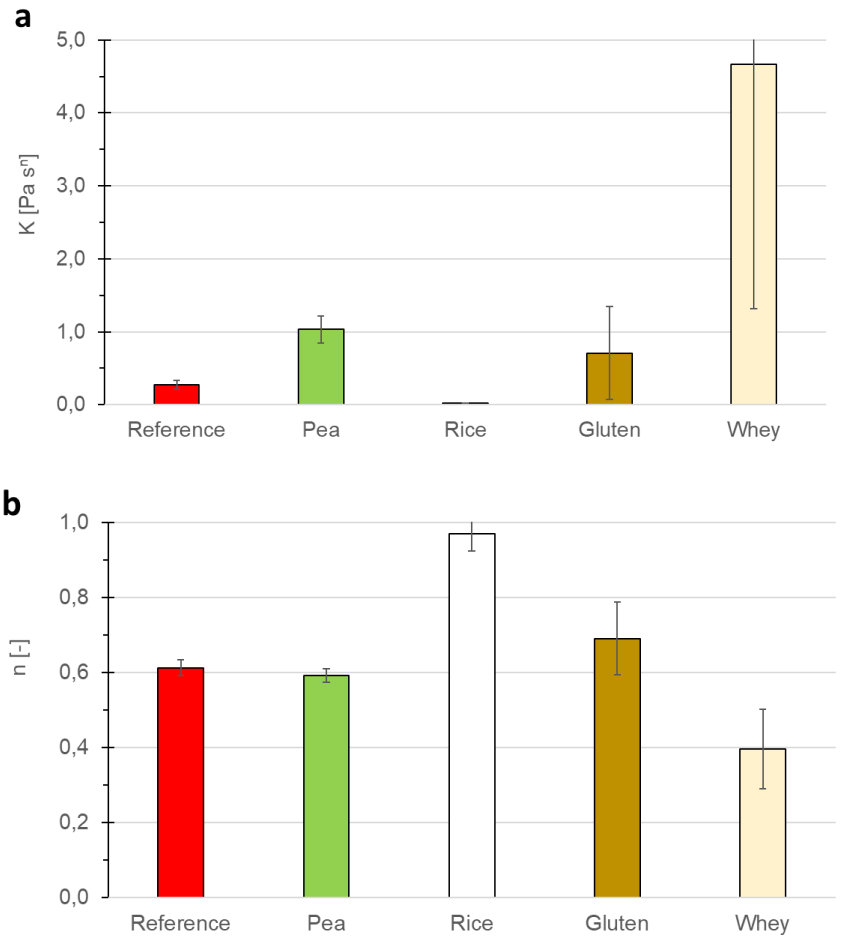

FIGURE 3: Power law constants for the sauces, a) consistency index K, and b) flow behaviour index n.

ACKNOWLEDGEMENTS

The Swedish Scientific Board FORMAS is gratefully acknowledged for funding the present work. Participants in the project FRESH are thanked for fruitful discussions.

REFERENCES

1. WHO WHO. *World report on Ageing and Health*. 2015. https://www.who.int/ageing/events/world-report-2015-launch/en/
2. Broge EHdL, Wendin K, Rasmussen MA, Bredie WLP. Familiarity and identification of everyday food odors in older adults and their influence on hedonic liking. *Food Quality and Preference*. 2023/01/01/ 2023;103:104715. doi:https://doi.org/10.1016/j.foodqual.2022.104715
3. Appleton KM. Increases in energy, protein and fat intake following the addition of sauce to an older person's meal. *Appetite*. 2009/02/01/ 2009;52(1):161-165. doi:https://doi.org/10.1016/j.appet.2008.09.009
4. Román L, Reguilón MP, Gómez M. Physicochemical characteristics of sauce model systems: Influence of particle size and extruded flour source. *J Food Eng*. 2018/02/01/ 2018;219:93-100. doi:https://doi.org/10.1016/j.jfoodeng.2017.09.024

5. Aït-Kadi A, Marchal P, Choplin L, Chrissemant A-S, Bousmina M. Quantitative Analysis of Mixer-Type Rheometers using the Couette Analogy. *The Canadian Journal of Chemical Engineering*. 12/01 2002;80:1166-1174. doi:10.1002/cjce.5450800618

BIOPOLYMERIC RHEOLOGY MODIFIERS IN LIME-BASED ENVIRONMENT

Tomáš Žižlavský[1] and Martin Vyšvařil[1]

[1]Brno University of Technology, Faculty of Civil Engineering, Veveří 331/95, 602 00 Brno, Czechia

ABSTRACT

Grout injection is also used to repair masonry and plasterwork on heritage structures. Since cementitious materials are generally deemed unsuitable, lime-based grouts are commonly used. The rheology of injection grouts is often modified to improve injectability and prevent bleeding and segregation. The use of rheology-modifying agents is mostly based on their behaviour in cementitious materials. While their properties are comparable, the dissimilarities may have crucial implications for the behaviour of rheology modifiers.

This study examines how biopolymeric rheology modifiers (e.g. cellulose ethers, diutan gum, and guar gum derivatives) affect the properties of air lime-based grouts prepared with the same flow value. Flow and amplitude sweep tests were conducted on pastes containing 0.5% of rheology modifier to study their behaviour. Grouts containing the modifier required a higher water-to-solid ratio to achieve the specified flow value, since the additives act by swelling and increasing the viscosity of the solvent. Bingham model was used to characterise the flow curves. Yield stress and plastic viscosity generally decreased at a rate corresponding to the increase in w/b in most cases. Elevated water content also led to lower loss and storage moduli observed during the amplitude sweep test while the simultaneous presence of additives promoted stability of the paste (LVR length), less brittle transition from viscoelastic solid to liquid behaviour and shift of the flow point to significantly higher strain values. The suitability of the studied additives for use in lime-based grouts is discussed with a view to further developing injection grouts.

INTRODUCTION

Injection grouting is a widely employed technique in the restoration and conservation of historical structures, offering an effective means of stabilizing and reinforcing deteriorated masonry and stone materials[1,2]. It involves the injection of fluid or semi-fluid grout materials into cracks, voids, or porous substrates to improve mechanical strength, reduce permeability, and restore structural integrity. Among the various types of grouts used, aerial lime-based injection grouts are preferred in restoration practice for their compatibility with historic materials, as they provide solution that respects the original materials of heritage constructions[3–5]. Achieving optimal performance in grouts requires careful control of their rheological properties, which directly influence the grout's injectability, penetration depth, stability, and setting behaviour[6].

Rheological parameters may be used to describe how the grout behaves under the shear stresses encountered during injection and how it behaves after placement. Yield stress (τ_0) represents the minimal force necessary to initiate flow[6–8]. Grout with an appropriately low τ_0 can overcome resistance in narrow capillaries and cracks within masonry, ensuring deep penetration without excessive pressure that might cause damage to historic substrates however, too low τ_0 leads to the grout flowing too freely, risking segregation and rapid loss from the

injection site [7,9]. Plastic viscosity (η) reflects the internal resistance to flow once τ_0 is exceeded, influencing the grout's penetration depth and distribution. Similarly to τ_0, high η leads to greater pumping pressures and reduced flow rates, limiting how far the grout can travel from the injection point while too low η leads to separation between solid and liquid phase [6,8,10]. Thixotropy, a time-dependent shear thinning property, governs the recovery of viscosity after shear is removed, crucial for maintaining homogeneity and preventing grout segregation or settling after injection [9,11].

To control and optimize these parameters, rheology modifying admixtures are often incorporated into grout formulations. Various cellulose ethers are commonly used based on their applications in cementitious materials however, mostly without dedicated studies on lime-based systems [12–15]. Lately apart from cellulose ether other biopolymeric admixtures such as guar gum or chitosan ethers, diutan gum and various algae extracts have been studied as cellulose ethers alternatives [16–21]. These admixtures not only modify rheology but also improve water retention, reduce shrinkage cracking, and increase adhesion to the substrate [13,16,22]. They mainly work by forming gels in aqueous media thus rising τ_0 and thixotropy, so in order to counter this also requiring higher water/binder (w/b) ratio. Cellulose ethers are recognized for their ability to increase τ_0 and improve thixotropy [12,13,23], while diutan gum contributes by viscosifying and stabilising effects [19,24,25]. Sodium alginate offers gel-forming properties through ionic cross-linking with Ca^{2+} ions present in solution helping to stabilise the suspension [26], chitosan and guar gum derivatives act in similar way to cellulose ethers with the effects largely dependent on the functional group added, e.g. use hydroxypropyl leads also to increased amount of air entrapped in the grout during the mixing process [13,22,27,28].

While the impact these admixtures on cementitious grouts has been partially studied, literature focusing on their use in lime-based grouts is sparse. Therefore, this study aims to explore the influence of selected biopolymeric rheology modifying admixtures on the rheological properties of aerial lime-based injection grouts studying flow and viscoelastic response of the grouts the research tries to understand how these additives alter grout's behaviour and performance that'll lead to improved formulation strategies for lime-based injection grouts, enhancing their applicability and reliability in the preservation of historic masonry and stone structures.

MATERIALS AND METHODS

CL 90 S aerial lime in accordance with EN 459 (vápenka Čerotvy schody, s.r.o, Czechia) was used to prepare the grouts with 0.5% weight addition of selected biopolymeric admixture (**Table 1**). The grout was prepared by dry mixing lime with admixture and then adding specified amount of water (water/binder ratio; w/b; **Table 1**), necessary to achieve 250 mm spread using EN 1015-3 flow cone – a value denoted as common by practitioners – after 60 s of mixing. After the same 60 s mixing procedure, the grout was introduced into the DIN concentric cylinder geometry with vaned tool installed on TA Discovery HR 1 hybrid rheometer, and 120 s from water introduction inti the mixture one of the following procedures was started at 20 °C Peltier system controlled temperature.

Flow and viscoelastic properties' procedure consisted of 60 s of preshear at 50 s^{-1}, followed by 60 s resting period and 0 s^{-1} to 100 s^{-1} to 0 s^{-1} flow sweep test; then, after 105 s of resting period, the amplitude sweep test at 10 rad s^{-1} angular frequency and strain from 0,001% to 1000% was conducted. The three interval thixotropy test (3iTT) intervals were 120 s at 0.1 s^{-1} shear rate followed by 60 s at 100 s^{-1} to breakdown the structure and another 300 s at 0.1 s^{-1} to

observe structural rebuild (see **Fig 3**). This test was conducted on fresh grout, starting 120 s after introduction of water into the mixture, placing the start of observation period 5 min mark.

TABLE 1: Used admixtures, their properties and w/b of prepared grouts.

abbreviation	chemical composition	manufacturer	η @ 20°C 2% aq sol. (mPa s)	w/b (–)
LG-ref	lime grout – no admixture	–	–	1.36
HPG	hydroxypropyl guar gum	Lamberti S.p.a.	68	2.31
HPCH	hydroxypropyl chitosan	Kraeber & Co, GmBh	6	1.42
HPMC	hydroxypropyl methyl cellulose	Lotte fine chemical	188	2.31
DG	diutan gum	CP Kelco	85	2.46
ALGNA	sodium alginate	Sigma Aldrich, Co	6	1.42
CMCH	carboxymethyl chitosan	Kraeber & Co, GmBh	5	1.48
CMC	carboxymethyl cellulose	Carl Roth GmbH	50	1.82
HEC	hydroxyethyl cellulose	SE Tylose GmbH & Co. KG	209	1.86
HEMC	hydroxyethyl methyl cellulose	Sigma Aldrich, Co	158	2.08

The linear part of down curves was fitted using Bingham model to determine the yield stress (τ_0) and plastic viscosity (η) of the grout. From the results of amplitude sweep test the critical strain (γ_c); end of linear viscoelastic region LVR) and flow strain (γ_F; modulus crossover, where the behaviour changes from viscoelastic solid to liquid) with corresponding values of storage modulus (G') were obtained. The γ_c was defined as the last point at which the G' lowers by less than 5% from the highest value at the plateau region. For 3iTT, the η at specific timepoints (5, 10, 20, 30, 60, and 300 s) at the recovery period was compared to the η measured at the end of first interval and express in relative terms as percentage of this η regained at the given timepoint.

RESULTS AND DISCUSSION

Flow properties

Fig. 1 (a) shows downward flow curves of several modified grouts along with example of Bingham fit on one curve. From the vertical positioning of the curves the decrease in τ_0 is evident of shown admixtures as well as growth of η represented by the slope of the linear part of the downcurve. The η growth is most evident for DG with significantly steeper curve as the η is about 8 times higher than that of unmodified grout as based on values of all the parameters shown in **Fig 1 (b)**. τ_0 in general diminishes with incorporation of admixture as the water content is increased decreasing the amount of solids in the mixture[29]. The effect is however not governed only by increased water content as seen by comparing HPG and HPMC, where the latter showed about double the τ_0 of the former even though the w/b is the same. The most notable is behaviour of HEC that increases both τ_0 and η despite the increased w/b. This is caused by HEC being the admixture with the highest viscosity in its aqueous solution (**Table 1**) as well as the later found slower gelling of HEC (see 3iTT, **Fig 3**) in lime suspension, that leads to the grout at the time of testing notably deviating from its properties at 60 s after mixing, when the w/b was determined.

The η of lime grout is generally increased as the water is replaced by more viscous admixture solution [15], however the efficiency of the admixtures does not completely mirror their solution η as the process is more complex, influenced by large amount of free Ca^{2+} ions in lime suspension as well as variable w/b that causes the concentration of admixture in the dispersing

medium to vary approximately between 2% and 3.5%. The effects of different media are evident in the case of DG, that even though having about half the solution viscosity of hydroxy-cellulose derivatives, causes significant increase in η, most likely thanks to its high stability even at highly basic solution with high amount of bivalent ions [24,25]. Overall, the decrease in τ_0 of the grout caused by increase w/b thanks to the water-retentive function of admixture, is beneficial to the injection grouts as it decreases also the injection pressure and therefore chance to damage the surrounding structures [6,8,9]. The increase in η on the other hand would limit the injection depth, making admixtures with moderate η increase such as HPG and HPMC more suitable options.

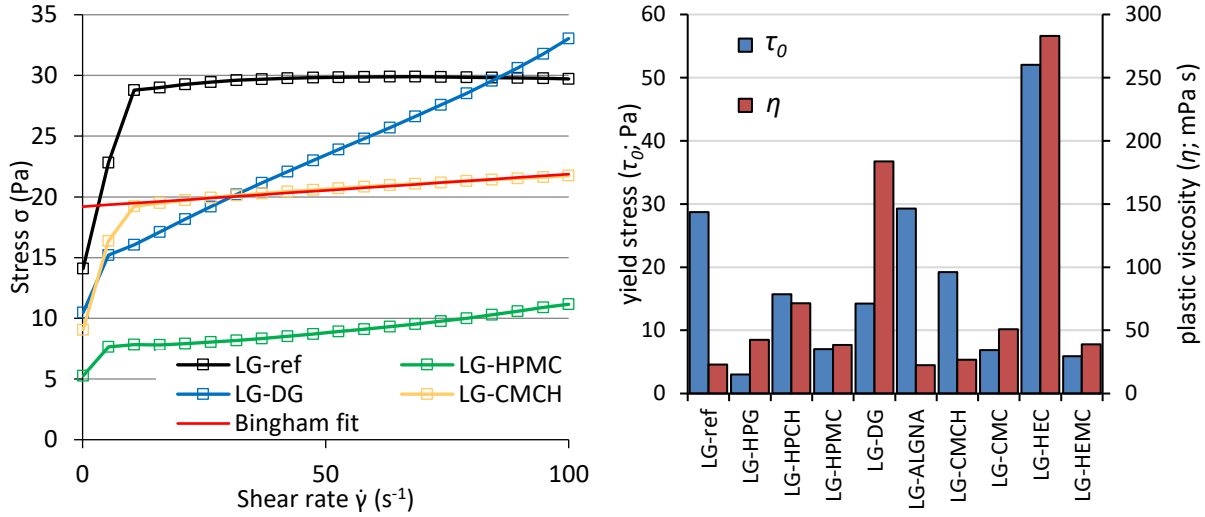

(a) (b)

FIGURE 1: (a) examples of downcurves of selected samples; (b) Bingham model parameters

Viscoelastic properties

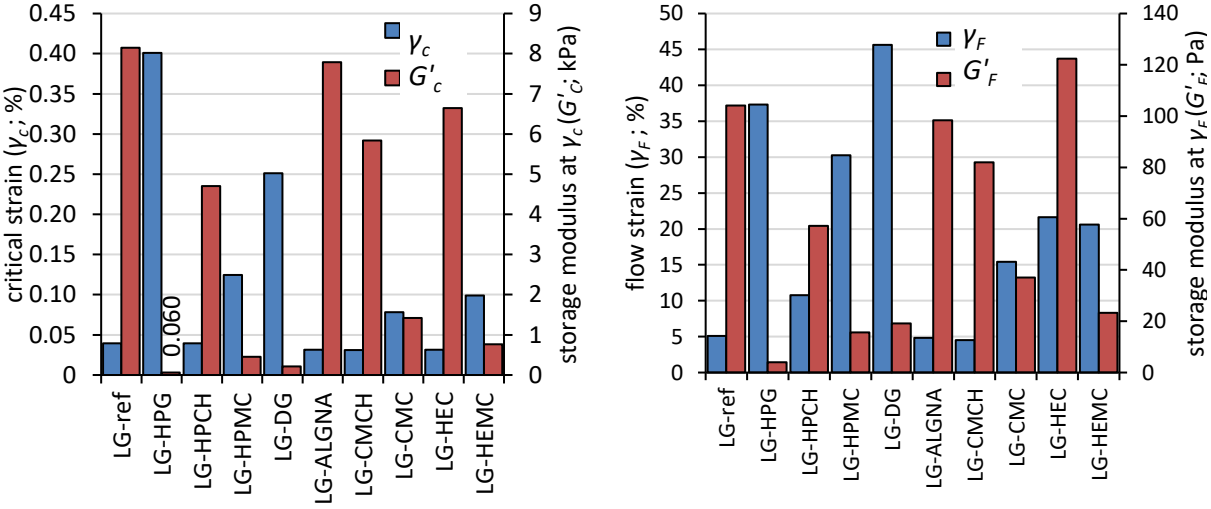

(a) (b)

FIGURE 2: (a) critical strain and corresponding storage modulus; (b) flow strain and corresponding storage modulus.

The results of the amplitude sweep test are shown in form of strain/storage modulus coordinates for two specific points in the grout behaviour: γ_c for the end of LVR where the stability of the

grout is compromised and its transition from viscoelastic solid to liquid behaviour through gel-like phase begins (**Fig 2 (a)**), and flow point (γ_F) where this transition end by the storage modulus intersecting the loss modulus curve and marking the start of liquid behaviour of the grout (**Fig 2 (b)**). During the test all the samples showed *G'* higher than *G''* behaving as viscoelastic solids as expected from the suspensions of larger particles with measurable τ_0 [17,21]. Two main effects can be observed here, the influence of increased w/b causing decrease in G'_C by up to three orders of magnitude due to increased amount of dispersing medium [21], and the stabilising effect of admixture gel formation resulting in LVR up to 10 × longer than that of the unmodified grout, the promotion of viscoelastic behaviour is expected as the sole aqueous solutions of the admixtures are viscoelastic [25,30]. Decrease in G'_C along with increase in stability shows of behaviour sough after e.g. in a case of self-compacting concrete that is also parallel to injection grout – ability to withstand much less force however with significantly higher amplitude, allowing the material to flow easily while preventing segregation [17,31]. By comparing the length of interval between γ_c and γ_F the more homogenous and gradual breakdown of the internal structure of most of the admixtures, apart from ALGNA and CMCH that show values comparable to unmodified grout, can be observed. This would mean, that more intensive mixing is required pre-application, which is however compensated decrease *G'* and therefore the strain needed to overcome the viscoelastic solid-like state.

Thixotropy

Thixotropy of the grouts using 3iTT was tested, and the results are presented in **Table 2** in a form of % of η regained at specified timepoints, and for selected admixtures as η evolution curves in **Fig 3.** The unmodified grout quickly regains all the original η, that further slightly grows as the lime grout ages. The introduction of the admixture along with increased w/b leads to only fraction of initial η being rebuilt just after end of second interval, as the gel restructuralisation in most cases takes significantly longer time. Majority of the grouts showed consecutive η growth with passing time while in case of HPCH it seems to plateau at around 90% relatively quick just around 30 s timepoint. For the grouts with high w/b, where the η is governed by the η of dispersing medium, all the mixtures shown 45-80% η rebuilt at studied time period, while grouts with w/b comparable to pure lime (CMCH, ALGNA) both reached the same comparable value although at slower pace.

TABLE 2: percentage of regained viscosity at specific timepoints after end of mixing period

	(%) of viscosity regained at time t(s) from end of second interval					
t (s)	5 s	10 s	20 s	30 s	60 s	300 s
LG-ref	102.4	106.8	108.2	108.1	109.2	115.7
LG-HPG	19.7	39.3	64.1	48.3	60.2	82.6
LG-HPCH	51.8	69.6	86.9	90.1	87.6	88.0
LG-HPMC	14.1	15.7	20.1	24.0	32.2	44.4
LG-DG	9.0	12.2	13.1	15.1	21.5	52.4
LG-ALGNA	73.8	71.9	71.7	73.0	80.7	120.2
LG-CMCH	76.2	73.5	74.7	76.5	82.4	127.6
LG-CMC	22.9	26.6	34.7	37.9	45.1	59.5
LG-HEC	151.6	202.7	282.1	312.7	333.5	309.7
LG-HEMC	24.6	26.4	37.0	43.2	50.9	66.4

The most distinct is the behaviour of HEC, that initially after end of second interval shows significant increase in η that further notably grows in first 60 s, showing either really high thixotropy and gelling properties of HEC [32], or possible delayed gel formation while compared to other admixtures as the η growth is significantly higher than in any other, even unmodified,

grout, meaning that during the first interval the gel was not yet fully formed therefore the test procedure of HEC may need to be modified to mirror its behaviour. The thixotropy decrease present in most cases may benefit injection grouts intended for injection of larger voids with fewer injection points, more complex crack network, and also pressure sensitive surrounding structure as the lower thixotropy ensures the grout will flow further into the structure even after the initial pressure is gone before it rebuilds enough structure to stay in place [8,9,33].

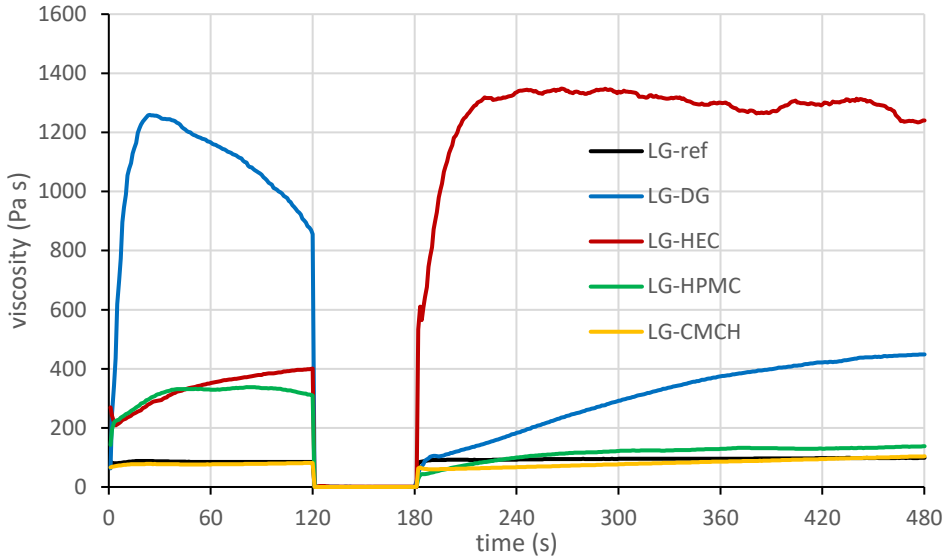

FIGURE 3: Results of 3iTT for selected grouts

CONCLUSIONS

The article studies the effects of various biopolymeric viscosity modifying admixtures on the properties of aerial lime-based grouts. The flow properties using Bingham model, internal structure using amplitude sweep test and thixotropy by a means of viscosity during 3iTT are studied.

The use of the selected viscosity modifying admixtures led to decrease in yield stress as the water/binder ration had to be increased to maintain specified workability, however plastic viscosity mostly grows as the water is replaced by more viscous polymer solution. The increase in amount of water, therefore decrease in solids fraction cases drop in storage modulus in the area of linear viscoelastic region, with admixtures stabilising the suspension in this area significantly prolonging the LVR. With changes to dispersing medium the manner of structural breakdown moves to more gradual and homogeneous as the flow point moves to almost order of magnitude higher strains. Most of the admixtures lower the thixotropy of the grout, showing slower more, gradual rebuilt of viscosity, promoting the grout's ability to flow after the initial stress is removed, improving the penetration depth. Only hydroxyethyl cellulose has opposite effect causing significant increase in viscosity as soon as the strain is removed.

The decrease in yield stress is essential for lowering the injection pressure, therefore protecting the delicate structures around the intervention site, for this alone, all the admixtures would be beneficial for use in lime-based injection grouts. However from the presented results mainly hydroxypropyl guar gum and hydroxypropyl methyl cellulose come as the most suitable as the significant drop in yield stress is accompanied by only minor increase in plastic viscosity. Further research should focus on the incorporation of other particles such as fillers and

pozzolanic additives into the mixture and the overall stability and behaviour of such to bring the experiments closer to applicable products.

Acknowledgement

The results were obtained with the financial support by the Czech Science Foundation, grant number 25-15748S “Lime-based injection grouts with biopolymeric and biotech admixtures to repair the surfaces of historic architecture”.

Bibliography

(1) Biçer-şimşir, B.; Griffin, I.; Palazzo-Bertholon, B.; Rainer, L. Lime-Based Injection Grouts for the Conservation of Architectural Surfaces. *Studies in Conservation* **2010**, *55* (Supplement-1), 3–17. https://doi.org/10.1179/sic.2010.55.supplement-1.3.

(2) Papayianni, I.; Bicer-Simsir, B.; Jornet, A.; Groot, C.; Valek, J.; Bokan-Bosiljkov, V.; Van Hees, R.; Padovnik, A.; Pachta, V. RILEM TC 243-SGM Report: Grouting for Historic Architectural Surfaces. *Materials and Structures/Materiaux et Constructions* **2023**, *56* (1), 1–17. https://doi.org/10.1617/S11527-022-02076-7/TABLES/3.

(3) Luso, E.; Lourenço, P. B. Experimental Characterization of Commercial Lime Based Grouts for Stone Masonry Consolidation. *Constr. Build. Mater.* **2016**, *102*, 216–225. https://doi.org/10.1016/J.CONBUILDMAT.2015.10.096.

(4) Padovnik, A.; Piqué, F.; Jornet, A.; Bokan-Bosiljkov, V. Injection Grouts for the Re-Attachment of Architectural Surfaces with Historic Value—Measures to Improve the Properties of Hydrated Lime Grouts in Slovenia. *International Journal of Architectural Heritage* **2016**, *10* (8), 993–1007. https://doi.org/10.1080/15583058.2016.1177747.

(5) Padovnik, A.; Bokan-Bosiljkov, V. Effect of Ultralight Filler on the Properties of Hydrated Lime Injection Grout for the Consolidation of Detached Historic Decorative Plasters. *Materials 2020, Vol. 13, Page 3360* **2020**, *13* (15), 3360. https://doi.org/10.3390/MA13153360.

(6) Jorne, F.; Henriques, F. M. A. Evaluation of the Grout Injectability and Types of Resistance to Grout Flow. *Constr. Build. Mater.* **2016**, *122*, 171–183. https://doi.org/10.1016/J.CONBUILDMAT.2016.06.032.

(7) Nonveiller, E. Grouting Suspensions, Solutions and Resins. In *Developments in Geotechnical Engineering*; 1989; Vol. 57, pp 35–68. https://doi.org/10.1016/B978-0-444-87400-9.50007-5.

(8) Cambefort, H. The Principles and Applications of Grouting. *Quarterly Journal of Engineering Geology* **1977**, *10* (2), 57–95. https://doi.org/10.1144/GSL.QJEG.1977.010.02.01.

(9) Van Rickstal, F. Grout Injection of Masonry, Scientific Approach and Modeling. Doctoral thesis, KU Leuven, 2000.

(10) Jorne, F.; Henriques, F. M. A.; Baltazar, L. G. Influence of Superplasticizer, Temperature, Resting Time and Injection Pressure on Hydraulic Lime Grout Injectability. Correlation Analysis between Fresh Grout Parameters and Grout Injectability. *Journal of Building Engineering* **2015**, *4*, 140–151. https://doi.org/10.1016/J.JOBE.2015.08.007.

(11) Khayat, K. H.; Saric-Coric, M.; Liotta, F. Influence of Thixotropy on Stability Characteristics of Cement Grout and Concrete. *Materials Journal* **2002**, *99* (3), 234–241. https://doi.org/10.14359/11968.

(12) Patural, L.; Marchal, P.; Govin, A.; Grosseau, P.; Ruot, B.; Devès, O. Cellulose Ethers Influence on Water Retention and Consistency in Cement-Based Mortars. *Cem. Concr. Res.* **2011**, *41* (1), 46–55. https://doi.org/10.1016/j.cemconres.2010.09.004.

(13) He, M.; Lin, Y.; Huang, Y.; Fang, Y.; Xiong, X. Research Progress of the Preparation of Cellulose Ethers and Their Applications: A Short Review. *Molecules 2025, Vol. 30, Page 1610* **2025**, *30* (7), 1610. https://doi.org/10.3390/MOLECULES30071610.

(14) Leemann, A.; Winnefeld, F. The Effect of Viscosity Modifying Agents on Mortar and Concrete. *Cem. Concr. Compos.* **2007**, *29* (5), 341–349. https://doi.org/10.1016/j.cemconcomp.2007.01.004.

(15) Silva, B. A.; Ferreira Pinto, A. P.; Gomes, A.; Candeias, A. Impact of a Viscosity-Modifying Admixture on the Properties of Lime Mortars. *Journal of Building Engineering* **2020**, *31* (December 2019), 101132. https://doi.org/10.1016/j.jobe.2019.101132.

(16) Boutouam, Y. ; Hayek, M. ; Bouarab, K. ; Yahia, A. A.; Rainieri, C.; Boutouam, Y.; Hayek, M.; Bouarab, K.; Yahia, A. A Comprehensive Review of Plant-Based Biopolymers as Viscosity-Modifying Admixtures in

Cement-Based Materials. *Applied Sciences 2024, Vol. 14, Page 4307* **2024**, *14* (10), 4307. https://doi.org/10.3390/APP14104307.

(17) Cano-Barrita, P. F. de J.; León-Martínez, F. M. Biopolymers with Viscosity-Enhancing Properties for Concrete. *Biopolymers and Biotech Admixtures for Eco-Efficient Construction Materials* **2016**, 221–252. https://doi.org/10.1016/B978-0-08-100214-8.00011-7.

(18) Zizlavsky, T.; Vysvaril, M.; Rovnanikova, P. Rheological Study on Influence of Hydroxypropyl Derivatives of Guar Gum, Cellulose, and Chitosan on the Properties of Natural Hydraulic Lime Pastes. *IOP Conf. Ser. Mater. Sci. Eng.* **2019**, *583* (1), 012009. https://doi.org/10.1088/1757-899X/583/1/012009.

(19) Žižlavský, T.; Vyšvařil, M.; Rovnaníková, P. Rheology of Natural Hydraulic Lime Pastes Modified by Non-Traditional Biopolymeric Admixtures. *Epitoanyag - Journal of Silicate Based and Composite Materials* **2019**, *71* (6), 204–209. https://doi.org/10.14382/epitoanyag-jsbcm.2019.36.

(20) Arizzi, A.; Banfill, P. F. G. Rheology of Lime Pastes with Biopolymer-Based Additives. *Mater. Struct.* **2019**, *52* (1), 8. https://doi.org/10.1617/s11527-019-1310-8.

(21) Cappellari, M.; Daubresse, A.; Chaouche, M. Influence of Organic Thickening Admixtures on the Rheological Properties of Mortars: Relationship with Water-Retention. *Constr. Build. Mater.* **2013**, *38*, 950–961. https://doi.org/10.1016/j.conbuildmat.2012.09.055.

(22) Žižlavský, T.; Bayer, P.; Vyšvařil, M. Bond Properties of Nhl-based Mortars with Viscosity-modifying Water-retentive Admixtures. *Minerals* **2021**, *11* (7), 685. https://doi.org/10.3390/min11070685.

(23) Feng, K.; Ma, K.; Yang, H.; Long, G.; Xie, Y.; Zeng, X.; Tang, Z.; Usman, I. U. Influence of Cellulose Ethers on Rheological Properties of Cementitious Materials: A Review. *Journal of Building Engineering* **2024**, *95*, 110347. https://doi.org/10.1016/J.JOBE.2024.110347.

(24) Espinal-Todd, S.; Sprayberry, S. S. Observation and Testing of Diutan Gum in Grout Mixes. **2012**, 1672–1680. https://doi.org/10.1061/9780784412350.0142.

(25) Xu, L.; Gong, H.; Dong, M.; Li, Y. Rheological Properties and Thickening Mechanism of Aqueous Diutan Gum Solution: Effects of Temperature and Salts. *Carbohydr. Polym.* **2015**, *132*, 620–629. https://doi.org/10.1016/j.carbpol.2015.06.083.

(26) Ručigaj, A.; Golobič, J.; Kopač, T. The Role of Multivalent Cations in Determining the Cross-Linking Affinity of Alginate Hydrogels: A Combined Experimental and Modeling Study. *Chemical Engineering Journal Advances* **2024**, *20*, 100678. https://doi.org/10.1016/J.CEJA.2024.100678.

(27) Khayat, K. H. *Viscosity-Enhancing Admixtures for Cement-Based Materials-An Overview*; 1998; Vol. 20.

(28) Gu, X.; Li, X.; Zhang, W.; Gao, Y.; Kong, Y.; Liu, J.; Zhang, X. Effects of HPMC on Workability and Mechanical Properties of Concrete Using Iron Tailings as Aggregates. *Materials 2021, Vol. 14, Page 6451* **2021**, *14* (21), 6451. https://doi.org/10.3390/MA14216451.

(29) Krieger, I. M.; Dougherty, T. J. A Mechanism for Non-Newtonian Flow in Suspensions of Rigid Spheres. *Transactions of The Society of Rheology* **1959**, *3* (1), 137–152. https://doi.org/10.1122/1.548848.

(30) Clasen, C.; Kulicke, W. M. Determination of Viscoelastic and Rheo-Optical Material Functions of Water-Soluble Cellulose Derivatives. *Prog. Polym. Sci.* **2001**, *26* (9), 1839–1919. https://doi.org/10.1016/S0079-6700(01)00024-7.

(31) Mezger, T. G. *The Rheological Handbook: For Users of Rotational and Oscillation Rheometers*; Vincentz, 2014.

(32) Maestro, A.; González, ; C; Gutiérrez, ; J M; Gonzá Lez,) C; Gutié Rrez, J. M. Shear Thinning and Thixotropy of HMHEC and HEC Water Solutions. *J. Rheol. (N. Y. N. Y).* **2002**, *46* (6), 1445–1457. https://doi.org/10.1122/1.1516789.

(33) Baltazar, L. G.; Henriques, F. M. A.; Cidade, M. T. Rheology of Natural Hydraulic Lime Grouts for Conservation of Stone Masonry—Influence of Compositional and Processing Parameters. *Fluids 2019, Vol. 4, Page 13* **2019**, *4* (1), 13. https://doi.org/10.3390/FLUIDS4010013.

AMYLASE SENSITIVITY TO pH IN STARCH-BASED THICKENED SOLUTIONS FOR DYSPHAGIA MANAGEMENT

José Manuel Aguilar García[1,2], Anna Miljkovic[2], Hanna Svensson[2] and Mats Stading[2,3]

[1]University of Seville, Spain
[2]RISE Research Institutes of Sweden, Gothenburg, Sweden
[3]Chalmers University of Technology, Gothenburg, Sweden

ABSTRACT

Dysphagia i.e. swallowing disorders negatively impacts on health and daily life, especially in older adults. It affects up to 30% of seniors above 65, which is particularly significant given that 20% of Sweden's population falls within that age group and is foreseen to rise due to longer life expectancy. Starch-based thickeners can provide tasty and good mouthfeel contributing to ensure a safe swallowing in seniors, except that starch is rapidly hydrolysed by salivary α-amylase.

This contribution focus on the role of pH in acidic, starch-based, thickened solutions to inhibit starch hydrolysis as a first step to the development of beverages adapted for dysphagia patients. The objective was to determine the range of pH values affecting α-amylase. For this goal, 5.4 %wt. starch-based solutions with pH between 2.1 and 2.9 were prepared, and viscosity was monitored using a systemic rheology approach for simulating oral processing conditions.

Results showed that the starch-based solution acidified at pH 2.1 inhibited α-amylase hydrolysis maintaining its viscosity during the test. On the contrary, a 72% drop in viscosity was observed after α-amylase was added to thickened solution prepared at pH 2.9, while a moderate decrease (41 and 59%) was showed for pH 2.3 and 2.5, respectively. In summary, the hydrolysis of starch-based solutions via α-amylase and, consequently, the viscosity can be modulated by adjusting pH. It highlights the potential application of these thickeners in the development of beverages to manage swallowing disorders.

INTRODUCTION

Swallowing disorders, or dysphagia, affects 10-30% of all aged 65 and above due to factors such as degenerative diseases, side effects of medication or simply age-related impairment of physiological oropharyngeal function[1]. The proportion of seniors over 65 is 20% in Sweden and is nearing 30% in Japan, compared to a global average of about 10%. Additionally, global life expectancy is projected to rise. Age-related dysphagia, which is seldom curable, necessitates the provision of texture-modified foods and beverages that can be safely swallowed [2].

Increasing the viscosity of beverages results in slower flow, allowing sufficient time for individuals with age-impaired physiology to swallow safely[3]. To prevent aspiration, it is also crucial to maintain the cohesiveness of the bolus, preventing it from breaking into droplets. This is achieved by thickening, which involves increasing shear viscosity and, also important, enhancing fluid elasticity[4,5]. Xanthan gum, the most commonly used dysphagia thickener,

contributes to elasticity but has the disadvantage of creating a somewhat slimy mouthfeel[6,7]. Dehydration is a common consequence of dysphagia, and the undesirable sliminess can exacerbate this issue. Starch-based thickeners offer the advantage of enhancing the taste and aroma intensity of beverages but suffer from a decrease in viscosity due to amylolytic process driven by α-amylase in oral saliva[8]. However, the pH value of the food media can inactivate this process as acidity is increased under pH values of 4 - 3[9].
The aim of the project FRESH was to develop starch-based, thickened beverages to provide a more pleasant mouthfeel for dysphagia patients. The objective of the present study was to highlight the role of pH in acidic starch-based thickened solutions to inhibit the enzymatic activity of α-amylose as a first step to the development of such beverages.

MATERIALS AND METHODS

Materials

Starch was kindly supplied by Lyckeby (Kristianstad, Sweden), as a modified potato starch thickener, pregelatinized and subjected to acetylation and phosphate crosslinking, labelled by EFSA as E1414. This starch was cold swelling and able to provide an appropriated viscosity and consistency. α-Amylase (cat. No. A6380) was obtained from Sigma Aldrich and citric acid (cat. No. 0244) from Merk. All reagents for INFOGEST protocol were obtained as follows: KCl (Merk, cat. No. 4936); KH_2PO_4 (Fisher Scientific cat. No. 4800); $NaHCO_3$ (Sigma-Aldrich, cat. No. 108378); $MgCl_2(H_2O)_6$ (Merk, cat. No. 5833); $(NH_4)_2CO_3$ (Sigma Aldrich, cat. No. 108375); HCl (Sigma-Aldrich 258-148J. T. Baker, cat. No 6081); $CaCl_2(H_2O)_2$ (Merk, cat. No 2382); and HCl (Sharlau, cat. No. AC0741). Ultrapure type I water, generated by a Milli-Q system was uses as solvent for all prepared solutions and dispersions.

Sample preparation

Aliquots of the starch were dispersed overnight at room temperature in Milli-Q by means of a magnetic stirrer to have 5.4 %wt. dispersions at desired pH values (2.1; 2.3; 2.5 and 2.9) by adding citric acid 2N. All dispersions showed an IDDSI-level 3 according to the International Dysphagia Diet Standardization Initiative (IDDSI) framework when tested by an IDDSI syringe.

Following the INFOGEST protocol[10], the starch dispersions were first mixed with simulated salivary fluid (SSF) in a 50:50 ratio. The mixture (40 mL) was inserted in the measuring cup of the rheometer and set at 37 °C to simulate the oral processing. For this purpose, α-Amylase (1 mL) was added later during rheological monitorization.

Rheometry

An ARES G2 strain control rheometer (TA Instruments, New Castle, DE, USA) equipped with a helical impeller in a 34 mm diameter cup was used for rotational tests, see **Fig. 1**. Viscosity was monitored at 37°C using systemic rheology[11]. For this purpose, samples and α-amylase were mixed in situ and stress growth tests were carried out at 50 s^{-1} for 600 s, being α-amylose added after the first 60 s. All measurements were performed in triplicate.

RESULTS AND DISCUSSION

To mimic a typical bolus the samples were mixed with simulated salivary fluid (SSF) without α-amylase at 37 °C and 50 s^{-1}, which is often referred to as a typical shear rate during oral processing. **Fig. 2**. shows the evolution of apparent viscosity as a function of time for 600 s. Reproducibility was good. Error bars were left out of Fig. 2. as the standard deviation was in the same order as the symbols.

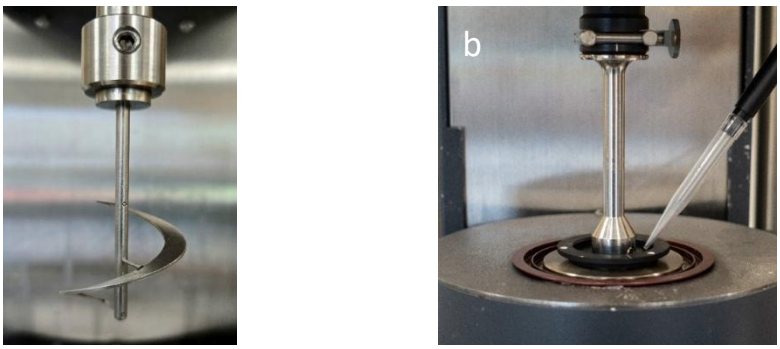

FIGURE 1: Experimental setup. a) Helical impeller system, b) addition of amylase

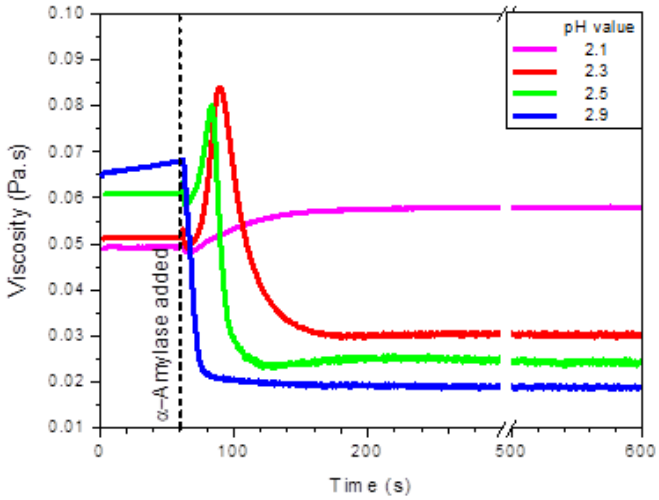

FIGURE 2: Evolution of apparent viscosity of Swely gel dispersions (5.4 %wt.) at different pH values before and after α-amylase was added to simulate oral processing ($\dot{\gamma} = 50\ s^{-1}$).

All systems showed an initially increasing trend after adding α-amylase. However, each of them followed a different evolution depending on the set pH value within the first 180 s, although all of them increased to a plateau after 120 s of adding α-amylase. Thus, 5.4 %wt. starch dispersions at pH starting with 2.3 displayed a decrease in viscosity, which got more pronounced as pH increased. The system at pH 2.3 exhibited a moderate decrease in viscosity (ca. 41%), whereas a sharp and immediate drop was observed for systems at pH 2.5 and 2.9 with a percentage decrease of 59 and 72%, respectively. On the contrary the system at pH 2.1 showed an increase in viscosity of ca. 29% in viscosity, maintaining its value to the end of the test (600 s). In any case, the final viscosity value after the α-amylase had acted on the samples for 9 minutes were in the order of 20-55 mPa s which imply values from 25 to 80 times higher compared to the viscosity of water (0.7 mPa·s) at the same temperature (37 °C).

On the other hand, the amylase sensitivity of starch-based dispersions at pH between 2.3-2.9 could be seen as a disadvantage for use in beverage. However, the decrease in viscosity appeared 20-40 s after adding α-amylase for pH 2.3 and 2.5, which is a relative long time compared to the few seconds that people usually keep beverages in their mouths. Furthermore, although those suffering from dysphagia may keep food and beverages in the mouth for a longer time, the whole effect of the exposure of these systems to amylase would not be taking place before 60 or 120 s from its addition for system at pH 2.5 and 2.3, respectively. This, beside the fact that the starch hydrolysis was not observed in the system at pH 2.1, open a possibility for

the use of starch-based thickeners in acidic beverages below pH 2.9 to get a better mouthfeel and safer swallowing.

CONCLUSIONS

The effect of adding α-amylase on the viscosity of starch-based thickened dispersions varied as a function of the set pH value in tests simulating oral processing conditions by systemic rheology. Whereas a pronounced effect was observed for system at pH 2.9, that one at the more acidic conditions inhibited the activity of the above-named enzyme. Samples within the studied range (e.g. 2.3 and 2.5) displayed a moderate fall in viscosity (ca. 40-60%). But, in either case, the completed effect of α-amylase was not observed until 10-120 s of adding α-amylase for systems at pH value 2.9-2.3. This may or may not be serious for those suffering from dysphagia as the timeframe of oral processing of beverages could be even shorter. Hence, starch-based thickeners can be an alternative to other gums used with a potential enhancement of the taste and aroma in acidic beverage. Consequently, beverages with low pH would be worth studying further for the design of tailored beverages for seniors and others suffering from dysphagia.

ACKNOWLEDGEMENTS

The Swedish Research Agency FORMAS are gratefully acknowledged for funding the FRESH project (2024-010319), and Ministerio de Ciencia, Innovación y Universidades for funding José Manuel Aguilar García.

REFERENCES

1. Barczi SR, Sullivan PA, Robbins JA. How Should Dysphagia Care of Older Adults Differ? Establishing Optimal Practice Patterns. *Semin Speech Lang*. 2000;21(04):0347-0364. doi:10.1055/s-2000-8387
2. Ekberg O. *Dysphagia - Diagnosis and Treatment*. 2 ed. Diagnostic Imaging. Springer International Publishing; 2019:924.
3. Newman R, Vilardell N, Clavé P, Speyer R. Effect of Bolus Viscosity on the Safety and Efficacy of Swallowing and the Kinematics of the Swallow Response in Patients with Oropharyngeal Dysphagia: White Paper by the European Society for Swallowing Disorders (ESSD). journal article. *Dysphagia*. 2016;31(2):232-249. doi:10.1007/s00455-016-9696-8
4. Chen J, Lolivret L. The determining role of bolus rheology in triggering a swallowing. *Food Hydrocoll*. 2011;25(3):325-332. doi:http://dx.doi.org/10.1016/j.foodhyd.2010.06.010
5. Nyström M, Qazi WM, Bülow M, Ekberg O, Stading M. Effects of rheological factors on perceived ease of swallowing. 2015;
6. Gössinger M, Buchmayer S, Greil A, et al. Effect of xanthan gum on typicity and flavour intensity of cloudy apple juice. *J Food Process Preserv*. 2018;42(10):e13737. doi:https://doi.org/10.1111/jfpp.13737
7. Richardson RK, Morris ER. Characterization of the perceived texture of thickened systems by dynamic viscosity measurements. *Food Hydrocolloids*. 1989;3(3):175-191.
8. Baert F, Vlaemynck G, Beeckman A-S, Van Weyenberg S, Matthys C. Dysphagia management in Parkinson's disease: Comparison of the effect of thickening agents on taste, aroma, and texture. *J Food Sci*. 2021;86(3):1039-1047. doi:https://doi.org/10.1111/1750-3841.15595
9. Freitas D, Le Feunteun S. Inhibitory effect of black tea, lemon juice, and other beverages on salivary and pancreatic amylases: What impact on bread starch digestion? A dynamic in vitro study. Food Chemistry. 2019;297:124885. doi:https://doi.org/10.1016/j.foodchem.2019.05.159.
10. Brodkorb A, Egger L, Alminger M, et al. INFOGEST static in vitro simulation of gastrointestinal food digestion. *Nature Protocols*. 2019/04/01 2019;14(4):991-1014. doi:10.1038/s41596-018-0119-1
11. Aït-Kadi A, Marchal P, Choplin L, Chrissemant A-S, Bousmina M. Quantitative Analysis of Mixer-Type Rheometers using the Couette Analogy. *The Canadian Journal of Chemical Engineering*. 12/01 2002;80:1166-1174. doi:10.1002/cjce.5450800618

Index of contributors